MODELLING AND TESTING MICROWAVE MAGNETRONS

by

Erwin Wilhelm Schumann

Submitted in partial fulfilment of the
requirements for the degree of
Doctor of Philosophy
in the
Department of Electronic Engineering,
University of Natal
Durban
1988

ABSTRACT

Though declining in popularity over the last decade, the magnetron still has applications where portable high power is needed. This study examines the predicted performance of cylindrical microwave magnetrons using analytic lumped-spoke models based on the energy conservation principle. The analytic approach is still favoured when small computer systems are used and the overall performance of the tube is to be predicted. The magnetron elements are examined and the role they play in the overall device performance analysed. Simplified representations of these elements are used to construct a complete magnetron model.

The Hartree threshold condition is reexamined and a new, more accurate analytic formulation proposed. This formulation is based on electric field strengths at the base of the magnetron spoke. The effect of the space charge on the threshold condition is included. Spoke current has been evaluated at the edge of the Brillouin hub. The resulting anode-cathode voltage performance predictions are consistent with measured results. A computer program has been written to analyse the performance predicted by this model. Models proposed by other authors are examined, and compared to this model. The resulting model has been tested by comparing predicted results to the measured performance of four slot-and-hole magnetrons.

To facilitate accurate magnetron testing, a new automated triple-stub high power microwave load has been developed. The load operates at a peak power of 1MW from 2,7-3,0GHz, and allows the change of the VSWR to any value along any path within the VSWR=1,5:1 circle. The development of the triple tuner and termination is discussed in detail. A new waterload configuration which has the advantage of simple construction yet good matching characteristics is presented. Automated measurement of pulling figure and construction of Rieke diagrams is discussed. The accuracy of the complete load is compared to conventional loads currently in service in the tube industry.

CONTENTS

APPENDICES

PREFACE

Background

The work described here was carried out on a part-time basis in the Department of Electronic Engineering, University of Natal, Durban, from April 1985 to December 1986, under the supervision of Professor H. L. Nattrass.

These studies represent a part of a larger study made by the author since October 1982 on High Power Microwave Devices. This broader study included the design and construction of solid state amplifiers, slot-and-hole magnetrons, voltage tunable magnetrons and travelling wave tubes. The author is at present responsible for the Travelling Wave Tube development Program at the University of Natal, a program designed as an instruction and research vehicle for under- and postgraduate students in the Materials Science Research Laboratory.

This work originally arose from an informal Support Program devised to assist the Council for Scientific and Industrial Research's (CSIR) magnetron program. The Support Program was divided into two areas; viz. tube design support and tube testing support. The objectives of the tube design support program was to write a computer program which could be used to assist in the design of new tubes and allow improvements of existing designs. The tube testing support program was to assist in the design and manufacture of a 'hot' test station.

As part of the tube design support program, the author conducted an investigation into the current state of magnetron modelling. As a result of the survey, it was decided to concentrate on so-called 'lumped-spoke' magnetron models, since these are a more cost effective design solution for a relatively young design team. Given the construction details these models allow the prediction of magnetron performance by ignoring details of electron movement and considering only the gross movement of the charge clouds. Though not as accurate as numeric particle simulation programs, they are analytic in nature and are thus more easily implemented in a program on a small computer system. The author wrote a magnetron design program CAMPA which has since been used to predict the performance of numerous magnetrons.

As part of the tube testing support program, the author designed a high power microwave test load. This unique design makes use of a philosophy different from other high power designs making use of state-of-the-art measurement and control equipment. The load, designated as the UNMS01, uses three computer controlled stubs, inserted into waveguide, to control the mismatch and phase of the load to a degree of accuracy that is not achievable using conventional design techniques. The author is not aware of an equivalent system in operation elsewhere. In 1985 RCA developed a Programmable Microwave Tuner (the PMT System) which, being a two slug system in slotted guide does not have the high power capabilities or versatility of the UNMS01. The UNMS01, which has been successfully tested to powers in excess of 900kW, is extremely flexible and allows reflection coefficient variation along any path within the VSWR=1,5:1 circle. This leads to numerous additional applications, including the dynamic matching of rotating antenna. At least one international tube manufacturer has expressed considerable interest in this design.

Work of this nature is for obvious reasons often restricted, and for political reasons laboratory research reports are at times unavailable; the literature survey was restricted to what was available in English and German papers through the British Library Lending Division and Dialog Information Services, Inc. literature surveys.

These studies represent original work by the author and have not been submitted in any form to another University for any degree. Where use was made of work carried out by others, it has been duly acknowledged in the text.

Claims

The author has made original contributions to the fields of magnetron modelling and the design of high power microwave test equipment.

The author has examined the modelling of magnetrons using lumped-spoke, energy conservation techniques, and has made a number of

improvements to existing models. This has resulted in improved magnetron performance prediction. These improvements are as follows :

1) Development of an Analytic Field Threshold Criteria

The threshold condition at the surface of the Brillouin hub has been evaluated in terms of the RF and dc fields at the hub rather than the voltages at the cathode and anode. This results in the correct prediction of the magnetron dynamic impedance. This is dealt with in section 3.3 of Chapter 3.

2) Inclusion of Space Charge Effects in the Threshold Criteria

Spoke space charge has been included in the calculation of the Field Threshold Criteria. This criteria gives the width of the electron spoke at the surface of the Brillouin Hub and leads to an improved prediction of the magnetron current-voltage characteristics. This is covered in section 3.4 of Chapter 3.

3) Spoke Current Calculation at the Base of the Spoke

The spoke current has been evaluated at the base of the spoke. This leads to an improved representation of the interaction mechanism within the tube that does not depend on an assumed shape of the electron spoke. This is dealt with in section 3.5 of Chapter 5. As illustrated in section 5.2 of Chapter 5, this gives improved magnetron performance prediction that is consistent with observed data.

To the author's knowledge, these formulations have not appeared in the literature before. Dr. J.R.M. Vaughan in his paper published in 1973 made reference to the question of field threshold conditions but has to the author's knowledge not persued this in any detail.

Predicted I-V characteristics are compared to previously published work and deviations highlighted. Reasons for these deviations are given in section 5.4 of Chapter 5.

The author has made use of modern day computer based test and control equipment to simplify the design of what would normally be a complex piece of test equipment. Here the author has made a number of contributions :

4)Development of a High Power Microwave Test Load *

A computer controlled power microwave load has been designed that is capable of providing a match of better than VSWR = 1,02:1. The author has designed and written a controlling program so that the load is capable of providing a mismatch of up to VSWR = 1,5:1 at any phase from 0 to 360^{o}, and can move along any path within the VSWR = 1,5:1 circle. The development of this load is dealt with in sections 4.2 to 4.7 of Chapter 4.

5) High Power High Performance Water Load

The author has designed an alternative power water load that is simple to construct yet provides a match of better than VSWR = 1,04:1. This load may be inserted into waveguide without the need to modify the guide. This is dealt with in section 4.6 of Chapter 4.

---

* E.W. Schumann, H.L. Nattrass, R.E. Ham, "The Design of a High Power Triple Stub Mismatch Unit", presented by the author at the First Joint Symposium on Antennas & Propagation and Microwave Theory and Techniques held in August 1986. Paper subsequently published in The Transactions of the South African Institute of Electrical Engineers, Volume 78 no. 2 December 1987.

6) High Power Mismatch Stub

The author has designed and constructed a novel high power microwave stub consisting of a metal loaded dielectric. This has the advantage of being simple to construct from readily available materials yet provides a lossless mismatch giving performance similar to a more expensive high dielectric material. This has been dealt with in Section 4.4. of Chapter 4.

To the author's knowledge, no load of comparable performance has been designed for magnetron testing.

Acknowledgements

The author wishes to thank the many people who have rendered assistance during these studies. In particular the author wishes to thank the following :

Professor H.L. Nattrass for his supervision, support and helpful suggestions,

Professor K.F. Poole for the encouragement needed to complete this thesis,

Mr. W. van den Berg, Mr. W. Drijfhout and others at the CSIR for assistance in developing the magnetron load and supplying useful magnetron data,

My wife Carolyn for proof reading and encouragement,

and

The workshop staff of the Department of Electronic Engineering for assistance in the construction of the UNMS01 and its prototypes.

Thanks is also extended to the Academic Staff of the Department of

Electronic Engineering for reducing the author's workload during the writing of this thesis and to the Council for Scientific and Industrial Research for financial assistance rendered.

Signed _____

Date 14/3/89

List of Principal Symbols

$\bar{B}$ - static magnetic field

B - magnitude of the static magnetic field

C_r - resonator capacitance

C_s - strap capacitance

D_1 - diameter of mismatch stub

D_2 - diameter of mismatch stub

d - anode cathode spacing

E - magnitude of the electric field

E_o - permitivity of free space

E_x - x directed electric field

E_x^{rf} - x component of the RF electric field

E_y - y directed electric field

E_p^{rf} - peak RF field

E_y^{sc} - y directed space charge fields due to spoke only

E_y^{static} static dc electric field

E_y^{th} - threshold field

E_y^{rf} - y component of the RF electric field

e - electronic charge $+1,6 \times 10^{-19}$

F_o - magnetron resonant frequency (H_z)

G_e - equivalent external conductance

G_l - equivalent loaded conductance

G_u - equivalent unloaded conductance

h - height of the Brillouin stream for the linear magnetron

h' - slot width

I_a - anode current

I^{spoke} spoke current

I - current

L - anode length

L_r - resonator inductance

l_s - resonator slot length

l_1 - transmission line length 1

l_2 - transmission line length 2

l_3 - transmission line length 3

k - width of spoke and a function of position y

m - electron mass

n - equivalent coupling transformer winding ratio

N - number of resonators

Q_e - external quality factor

Q_l - loaded circuit quality factor

Q^{spoke} total spoke charge

Q_u - unloaded anode block quality factor

q - spoke charge

P - circuit period

P_a - anode bombardment power loss

P_c - cathode back heating power loss

P_e - potential function within the interaction space

P_s - time average power transmitted across a closed surface S

P_u - anode block resistive heating losses

P_x - output power

R_r - equivalent resistance representing resonator losses

R_{eq} - resistance component of the load transferred to the resonant circuit

R_1 - reflected wave 1

R_2 - reflected wave 2

R_3 - reflected wave 3

R_n - reflected wave from n-th hairpin bend

r_b - Brillouin radius

r_s - synchronous radius

u_o - initial velocity of an electron

V_a - anode dc voltage

V_{rf} - peak anode RF voltage

V_{as} - synchronous voltage (Hartree voltage)

v_p - RF wave phase velocity

v_x - x-directed electron velocity

v_y - y-directed electron velocity

w_s - strapped resonator frequency

w_c - cyclotron frequency (=eB/m)

w_u - unstrapped resonator frequency

w - frequency of RF wave (rad/s)

X - normalised stub reactance

X_1 - normalised reactance of mismatch stub 1

X_2 - normalised reactance of mismatch stub 2

X_3 - normalised reactance of mismatch stub 3

Y_o - output admittance of anode block

Y_r - resonator admittance

Z - characteristic impedance of a single resonator

Z_{term} - load terminating impedance

ε_o - permitivity of free space

β - circuit propagation constant

β_n - phase angle at base of the electron spoke

λ_c - circuit wavelength

ρ - Brillioun charge density

ρ_l - equivalent line charge of spoke

θ - angle at the centre of the spoke

λ_π - pi-mode resonant wavelength

$\lambda(N/2-1)$ resonant wavelength closest to the pi-mode wavelength

CHAPTER 1

INTRODUCTION

The magnetron was developed during the Second World War as a lightweight, high power microwave source for airborne applications. Though declining in popularity in this sphere since the development of power microwave semiconductor technologies capable of operation in the GHz region, the magnetron today still finds a number of applications in the communications and radar fields. The major advantage of this tube when compared to semiconductor devices is its compactness, high efficiency and high pulsed power output.

Theoretical magnetron studies saw an intense period of activity during and immediately after the war. This period saw the publication of a comprehensive document, edited by Collins[1], representing the state of the research at that time. Theoretical and practical research continued up until the early sixties, when a further collection of works, edited by Okress[2] was published. Although much effort went into understanding the tube operation, it continued to defy complete analysis. In addition, with the advantages of coherent radar becoming apparent, research efforts were diverted to linear beam tubes and semiconductor devices. After the tremendous effort, magnetron research all but died away and an enormous amount of research material was never published. Though tube performance has improved since that time, the improvements have been more of a technological nature than theoretical.

All microwave tubes rely on the interaction between an electron beam and an electromagnetic wave. The electromagnetic wave is usually supported by a microwave circuit so designed that the electric field component of the wave may suitably couple with the electron beam. The electron beam is generated by a heated cathode and a static electric field in the conventional manner and usually focused by a static magnetic field. The magnetron belongs to the family of so-called crossed-field tubes, since the static magnetic field is orientated at right angles to the electric field. Although the microwave circuit may take on a variety of configurations, favourable interaction occurs

when the electric field component of the RF electromagnetic wave is parallel to the electron motion.

Modern magnetrons are usually of the cylindrical type and have a RF circuit that is circular in format resulting in a rotating RF wave. The electron source is a cathode located at the centre of the circuit, and the dc magnetic field is at right angles to this plane of the circuit. The resulting electron pattern must rotate about the cathode if favourable interaction is to occur. This is shown in Fig. 1.1 .

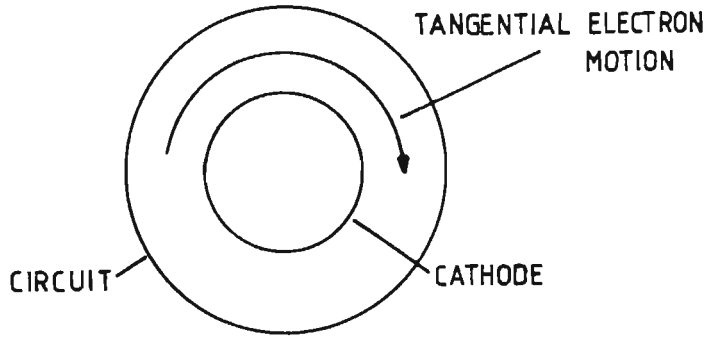

Figure 1.1 Circuit and beam configuration

A dc voltage is applied between the cathode and the microwave circuit. The microwave circuit is of a resonant type, capable of supporting a travelling wave rotating in both directions. The electric field component of this travelling wave parallel to the transverse electron motion interacts with the electron stream in such a way that the electron stream may give up energy to the rotating wave; the movement of the charge is in the form of spokes, the RF wave grows and the interaction process is self sustaining.

The most complicating aspect of the tube's analysis is that it is a three dimensional problem with an unknown charge and field pattern. Computer simulation of two dimensional, planar magnetrons show a turbulent electron stream flowing in spokes from cathode to anode. End space emission, non-axial magnetic fields, and circuit asymmetry are just a few of the additional complications in store for the enthusiastic theorist. The end result is that the tube industry has had little time for theoretical models, and still today tends to design new tubes as variants of existing designs. Unlike the semiconductor industry, where a new circuit can commit an entire

production facility, it has always been a relatively simple task to try a few variants of a design in parallel with an existing production facility. There is thus at present little motivation to develop a comprehensive magnetron Computer Aided Design facility.

1.1 An Overview of Work Published since 1961

Works published on magnetrons in the English literature since that of Okress in 1961 encompass a wide range of study areas. What follows is by no means a complete list of published works, but a sample of what may be considered to be significant contributions to the study of magnetrons. For the sake of some order these works have been divided into three categories as follows :

1) Magnetron theory and performance prediction
2) Relativistic magnetron studies
3) Technological innovations

1.1.1 Magnetron Theory and Performance Prediction

In 1965 Yu et.al.[3] wrote the first comprehensive numerical simulation program to predict the operation of the planar magnetron in detail. Using an equivalent set of charge rods the electron spoke shape during transient and steady-state could be predicted. In 1966 and 1967 Bayburin et.al. published three papers describing analytic models; the first[4] examining the formation of the magnetron spokes in the interaction region, the second[5] predicting the distortion of the spokes as a result of space charge and the third[6] presenting a unified model predicting overall device performance. The spoke shapes predicted agreed well with the numerical studies of Yu; however the detail of charge motion and start-up conditions could not be predicted. In 1973 Vaughan[7] used an ingenious approach by utilising the spoke formation criteria of Welch[8] together with empirical formulae to predict the overall device performance. The model had the advantage of being compact enough to be installed on a small computer;

this was achieved by again neglecting the detail of charge motion and instead considering a good approximation of gross charge movement in the steady-state.

In 1976 Shein et.al.[9] used averaging techniques to predict the shape of the spokes in the presence of multiple RF frequencies. In 1977 Shaw[10] used analytic techniques to predict the start-up in a distributed emission crossed-field-amplifier. He concluded his work by comparison with more accurate numerical computer predictions and found good agreement between the two methods.

In 1980 Thomas[11] used the soliton approach to understanding the non-linear interaction in a crossed field amplifier. The soliton concept was developed in the plasma physics field to describe the Langmuir waves and turbulent phenomena. It has been found to be a useful approach[12] which may be extended to other electronic devices where an electromagnetic wave propagates through an electron cloud. The agreement between predictions using the soliton approach and numeric techniques has been good[13,14].

Use of the structural method[15] has allowed the calculation of the electrostatic field in a 3-dimensional model of the magnetron. It has shown that the static field is distorted considerably due to the anode vanes and end cap effects. This would effect the electron paths around the circuit and distort the cloud shape.

Attention has been given to analysing the 'cold' resonant characteristics of magnetrons. Analysis of resonator systems as a concatenation of radial waveguides[16] has helped mode identification in coaxial tubes. Finite Element Methods[17] have been used to determine the cold resonant characteristics of a resonator block with some success. In 1988 Allen et.al.[18] demonstrated the use of the Transmission Line Matrix Method applied to a magnetron resonator structure to compute the 'cold' mode spectrum.

In 1983 Bayburin[19] constructed a complete analytic model based essentially on the concepts of Vaughan's paper in 1973[7], though it contained some improvements by reducing the reliance on empirical formulae. Again this method could be implemented on a small computer

system and could provide information on the overall performance of the magnetrons.

In 1983 Krasnenko[20] used an averaging method to determine the motion of out of phase electrons in a magnetron. Results were compared to numeric equations obtained from integral equations.

Bayburin's paper[21] published in 1984 deals in fair detail with the problem of using 'large-particle' methods to analyse the behavior of crossed field amplifiers. Here he uses a numerical approach and provides some plots showing the shape of 'spokes' formed in the interaction space. This was followed up in 1985 by another paper by Bayburin[22] attempting to determine the limits to the operation of a magnetron by analytic means.

What is particularly striking is the diversity of mathematical techniques employed to attempt to obtain improved performance prediction or to gain a better insight of the device's operation. The advantages of the analytic approach is that it allowed easy prediction of overall device performance but at the expense of losing the detail of the charge movement and spoke shape. The advantage of the numeric particle simulation approach is that it provides more detail and gives a realistic account of interaction procedures. These two streams of research (that is the numeric and analytic approach) have tended to remain largely separate up to the present day. Numerical particle simulation techniques though expensive to implement have proven to be accurate for a large range of configurations. These simulations take into account electron motion to varying degrees of accuracy but require long simulation times on large mainframes (in the order of hours of time on a CRAY computer[23]). The numeric approach has generally been expensive and used to obtain a better understanding of a specific aspect of device performance rather than as a design tool. Unless the user can afford multiple runs, the effect and significance of the various design parameters on device operation is easily obscured. In this respect the analytic approach has had more success and workers have shown that more economical analytic models have the potential of accurately predicting tube output characteristics. These are thus often the preferred design tools.

1.1.2 Relativistic Magnetron Studies

Most recent effort however has been directed towards research into relativistic magnetrons, since they provide powers far in excess of those operating at 'conventional' voltages. In the quest to obtain higher powers anode voltages were increased to the hundreds of kilo-Volts to Mega-Volt region. Work initially undertaken by Bekefi, Orzechowski and Palevsky in 1975 resulted in devices achieving powers of 900MW[24]. Some of the first high voltage magnetron experiments documented were those of Palevsky et.al.[25]. Fully relativistic particle-in-cell (PIC) codes were used to simulate these tubes. Two types of tubes are presented here viz. a small gap magnetron using 6 vanes with an anode cathode aspect ratio of 0.15-.25 and a large gap magnetron 54 vane S- band tube. The former operates at 360kV-600kV in the 2-pi mode delivering 850MW with a 50nS pulse. The latter generated 500-800 MW at 600kV. These tubes all used field emission (cold) cathodes. In 1981 Chekanova et. al.[26] reported powers in excess of 4GW using similar techniques and increasing anode lengths. In 1982 Ballard et.al.[27] used conventional design techniques with a thermionic oxide cathode at 500kV to achieve powers in the order of 20MW. With appropriate adjustments, it was found that at relativistic voltages both numerical simulation and conventional design techniques had areas of validity[28,29,30], though at least one alternate theory[31] was presented at the time.

1.1.3 Technological Innovations

Technological improvements have resulted in smaller, more reliable and more cost effective tubes which have helped keep the tube on the market. Extensive use of ceramics instead of glass means devices are more rugged, while improved processing techniques give longer life. By and large conventional design techniques are employed and measurements are used to refine the performance of prototype designs. In recent years a few innovations have emerged; the main area addressed is that of magnetron tuning. In 1984 Morton[32] used the double-output method to tune a tube by connecting one output to a microstrip tuner switched by PIN diodes, Gunnarsson[33] described a spin-tuned stepper driven

magnetron and a tuning fork system has been used to provide a frequency agile tube[34]. In 1985 English Electric Valve[35] produced a compact unit by incorporating a magnetron, duplexer and solid-state receiver in one packet. A number of improvements have also been made by incorporating integral switched-mode power supplies with the tube, thus removing one of the tube user's headaches.

1.1.4 The Choice of Model for Design Purposes

Though research has continued since the 1960's no unified magnetron theory exists. Numerical particle simulation has provided an increased understanding but even these complex programs do not completely take into account the three dimensional nature of the problem. This complex electromagnetic wave-charge interaction problem will probably never be solved unless research efforts are increased.

To be effective, a program used as a design tool must be sufficiently versatile. It must be accurate in predicting the device performance, fast enough to allow iterative design optimisation and inexpensive to run. If these conditions are satisfied the program will serve an additional purpose; that of allowing the user to obtain an increased understanding of device performance. For this reason it was decided to use an analytic approach when developing the magnetron model; details of electron movement are ignored and only the overall movement of the charge cloud is taken into account.

1.2 The Magnetron Model

Initially the magnetron is divided into four distinct sub-components. The first is the cathode which is presumed to be operating in space charge limited conditions, acting as a supply plane of electrons. The second is the electron cloud, which is a synchronous hub rotating about the cathode with a series of 'spokes' reaching from the hub to the cathode. The third, the anode circuit, is modelled as a lumped equivalent circuit resonator made up of of capacitors and inductors.

This circuit is presumed to be operating only in the pi-mode, since this mode has considerable operating advantages over the other modes. The last sub-component is the output circuit modelled as a coupling element, transformer, transmission line and load. These components are discussed in more detail in Chapter 2.

In Chapter 3 the details of the electromagnetic wave and the charge cloud interaction are introduced. The motion of the cloud is related to the RF electric field, which is related to the output characteristics. Using energy concepts the tube operating characteristics are calculated. This model differs from previous work on three points:

The first concerns the fundamental concept of the Hartree (or threshold) condition. The threshold voltage is the minimum anode voltage necessary to allow the electron cloud to drift from the cathode to the anode in the spoke and thus give up its energy to the RF wave. As proposed by Welch[8], the anode voltage need not exceed the threshold at all points, only there where the spokes are to form. However in the presence of RF voltages it is necessary to consider the electric field conditions rather than the voltage at the anode circuit. Chapter 3 formulates Welch's condition based on fields and results in a more accurate prediction of the tube dynamic impedance.

The second addition to the model is the incorporation of space-charge effects to determine the threshold field. This space charge field modifies the threshold conditions further and results in an increase in the predicted operating voltage. This agrees closely with measured results.

The third model improvement is obtained through the careful selection of the spoke current formula. In this model the spoke current is calculated at the base of the spoke. This results in a formula that is not dependent on empirical formula or on any presumed spoke shape.

These improvements result in improved magnetron performance prediction. Chapter 5 compares the predicted and measured performance of a number of tubes. The shape of the predicted current-voltage curves are examined in some detail, and compared to predictions of

other workers.

1.3 Magnetron Load Development

In order to age and accurately test magnetrons a high power load is required. The load must not only be able to absorb the full load power with minimal reflection, it must also present the tube with a VSWR of 1,5:1 at any phase to allow the determination of the tube pulling figure[1]. On examination of currently available loads it became apparent that most loads did not adequately satisfy these requirements. A high power load was thus developed that has a number of features not found in conventional loads. The development of this 3-stub computer controlled load is discussed in Chapter 4. This load allows a match of better than 1,02:1 to be obtained. It also allows the adjustment of the VSWR to any value up to 1,5:1 and the continuous variation of the the phase of the mismatch from 0 to 360^{o}. This load may be directly used to automatically plot Rieke diagrams[1] and to age magnetrons, both normally time consuming processes. This load has many more applications in industry, including the dynamic matching of a rotating radar antenna or any load with a predictably changing mismatch. Though not implemented in the final design, Chapter 4 presents an alternative power water load consisting of offset hairpin tubes that lower the mismatch to 1,04:1.

Chapter 5 deals with tests using this load conducted on a magnetron constructed at the CSIR, Pretoria, comparing the measured performance of the tube to its predicted performance using the magnetron model.

CHAPTER 2
FUNDAMENTAL ANALYSIS

2.1 Introduction

Fundamental magnetron theory tends to ignore the detail of charge motion and electric field patterns while concentrating on the overall gross device behavior. Charge entities are isolated, their trajectory plotted in the absence of other charges and that trajectory taken to be the direction of all charge movement in the vicinity. Charge movement is presumed ordered and laminar, with RF and dc electric fields unaffected by the space charge.

Many excellent texts[1,2,36,37,38] are available that serve to introduce these fundamental concepts of magnetron analysis. This chapter takes a brief look at concepts important to the development of the model in Chapter 3. Section 2.2 examines the magnetron cathode, noting the conditions under which it must be operated so that the model developed may be valid. Section 2.3 is a general discussion of electron motion in crossed fields and examines the form of the space charge cloud at the cathode during pre-oscillation conditions. Section 2.4 examines electron motion between the cathode surface and the synchronous charge hub, where the RF fields become important. Sections 2.5 to 2.7 examine the anode circuit, the electron stream and the output circuit. Finally interaction between the electrons and the RF wave are examined in section 2.7 giving some qualitative insight into the formation of the magnetron 'spokes'.

2.2 The Magnetron Cathode

The cylindrical magnetron cathode, usually located in the centre of the RF circuit, is often a source of tube performance problems. J.R. Pierce[39] described an ideal cathode as one which, without heating or bombardment emits electrons freely in unlimited quantities. However this is far from practical and most microwave tube

cathodes (apart from relativistic magnetrons which rely on field emission) are heated to temperatures in the order of 1000^{o}C and are able to supply only a limited current density. In addition to electrons, cathodes liberate chemicals from their surfaces often contributing to short tube life and sporadic operation. The electrons are also emitted at finite random velocities, leading to increased device noise and beam focussing problems.

2.2.1 Space Charge Limited Emission

As the temperature of the cathode is increased the emission increases; the emitted electrons depress the potential and if the emission continues to increase the potential could drop below zero forcing the electrons back to the cathode. If the electric field at the surface of the cathode is zero the cathode is said to operate in space charge limited (SCL) mode. This has a number of advantages in that the emitted charge becomes less dependent on the cathode characteristics. Electrons are essentially emitted at zero velocity and emission is uniform over the cathode surface even if the temperature is not. The supply of charge may also be taken to be infinite as long as the emission is less than that which would give zero field at the physical surface of the cathode. Increasing the emission would no longer result in space charge limited conditions while decreasing the emission would result in the point of zero electric field moving away from the cathode physical surface.

Thus, if operating in SCL mode (as is generally the case) the cathode may be considered ideal in the sense that it is a uniform emitter of electrons with zero initial velocity essentially acting as an infinite electron supply surface.

2.2.2 Secondary Emission

Crossed-field tube cathodes however are subjected to more harsh treatment than linear beam tubes. Some electrons emitted from the cathode surface, if phased so as to gain energy from the RF field, are returned to the cathode with increased energy. This bombardment of the surface liberates further electrons which may contribute to the

interaction process but may also reduce the cathode life. In addition the liberated secondary electrons generally have a higher energy than thermally generated electrons, resulting in increased device noise. In terms of device modelling, even if the cathode surface is operating under SCL conditions, electrons cannot be assumed to be emitted at zero velocity unless the temperature is increased substantially.

2.2.3 The Cathode Model

Detailed modelling of cathodes is a field of its own (see for example Beck and Ahmed[40] or Buck and Clogston[41]). For the purpose of the model presented in Chapter 3 however, the cathode will be presumed ideal. As long as the cathode is operated in space charge limited mode the random emission of secondary and thermal electrons will do little to affect the overall device performance. The real device will however continue to plague the tube designer, particularly with respect to its pulsed performance.

2.3 Electron Motion in the Absence of RF Fields

2.3.1 General Considerations

In the absence of an electric field but in the presence of a magnetic field an electron with initial velocity u_o will move in a circular orbit of radius u_o/w_c and will rotate at the cyclotron frequency $w_c=eB/m$. If an electric field is applied the electron path will be a cycloid with an average drift motion in a direction perpendicular to both the electric and the magnetic field. An example of this is shown in Figure 2.3.1.

If the electron has an initial velocity $u_o=E/B$ it will continue in a straight line at an unchanged velocity. Under these conditions a stream of charge exhibiting laminar flow with an initial velocity E/B will continue to exhibit laminar flow. If the electron enters at a velocity $u_o>E/B$ it will initially be deflected in the direction of the electric field and if $u_o<E/B$ the electron will be deflected in the

opposite direction to that of the electric field.

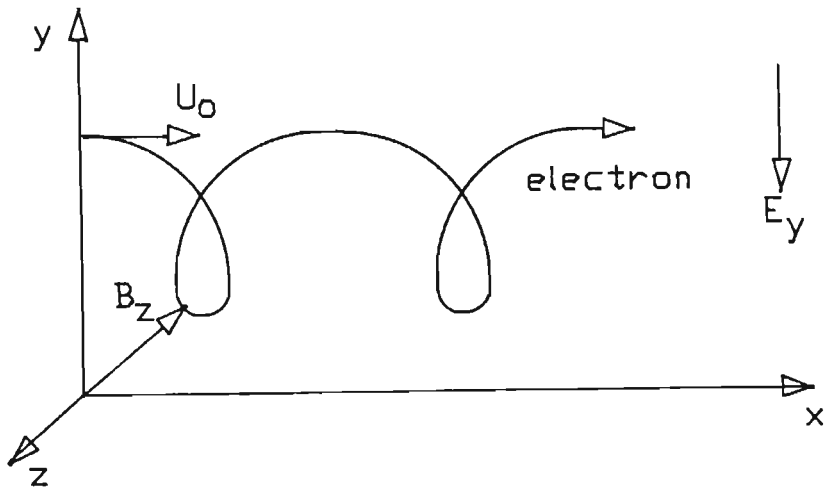

Fig. 2.3.1 : Cycloidal Electron Trajectories

An electron starting at rest at the cathode of a magnetron will follow a path shown in Figure 2.3.2.

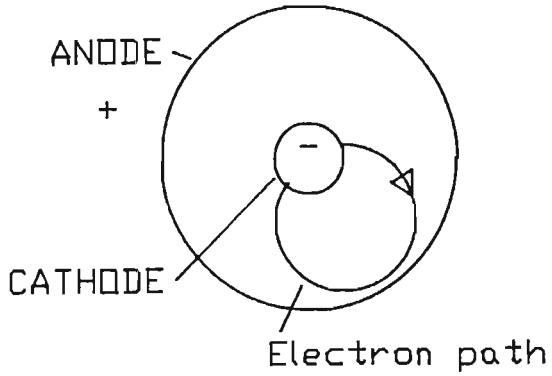

Fig. 2.3.2 : Electron Trajectory in a Cylindrical Cathode

If the electron path just touches the anode the electric and magnetic fields are said to satisfy the Hull cut-off condition. This is illustrated in Figure 2.3.3 which shows the relationship between anode voltage and magnetic field which gives current flow. This curve is termed the Hull cut-off parabola. Normally magnetrons operate far away from the cut-off parabola, at higher magnetic fields where no current would theoretically flow if no RF fields existed.

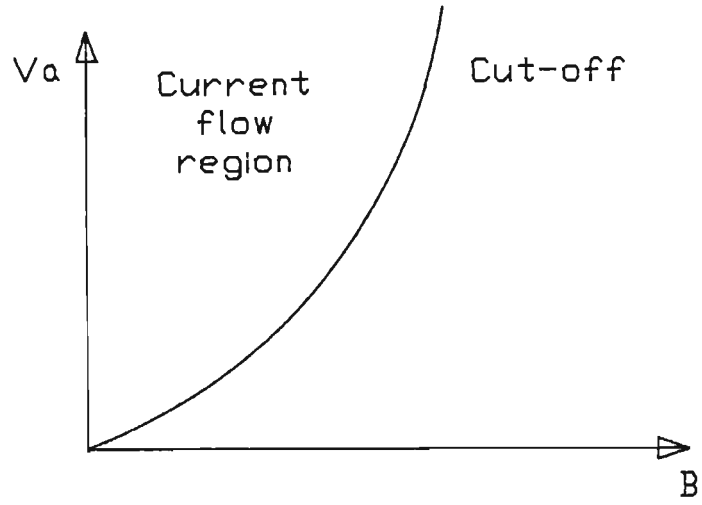

Fig. 2.3.3 : The Hull Cut-off Condition

2.3.2 Electron Motion near the Cathode

Examining the charge flow in the absence of an RF electric field is of importance since it gives a starting point to the analysis. It will also be shown later that the RF electric field near the cathode is small so that the pre-oscillation condition is a valid picture of conditions at the cathode during oscillation. The exact nature of charge flow at the cathode is today still a matter of debate. Is it laminar or is it cycloidal ? Or does it exhibit characteristics of both ? Numerical particle simulations appear to indicate that the flow at the cathode is highly turbulent[14] while considerable theoretical and practical evidence[42] exists that it approximates laminar flow. Figure 2.3.4 illustrates an electron stream exhibiting laminar flow. The charge cloud is termed the Brillouin layer and the stream is said to exhibit Brillouin flow.

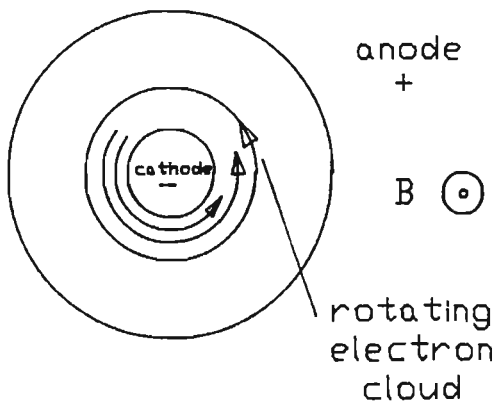

Fig. 2.3.4 : Pre-oscillating Electron Stream

In the Brillouin layer the radial component of charge velocity is zero but the tangential component changes with distance from the cathode.

2.4 Electron Motion in the Presence of RF Fields

It turns out that under certain conditions it is possible to assign a fairly simple formula to the drift motion of the electrons even in the presence of more complex static and RF electric fields. The full analysis may be found in various texts[43,44] and is not repeated here. It is found that if the cyclotron frequency w_c is much greater than the RF frequency w the RF field may be considered to be static; the cycloidal motion will be small compared to the drift motion of the charge. The mean trajectory can then be obtained by considering the velocity of the charge at each point to be $(\bar{E} \times \bar{B})/|\bar{B}|^2$. It turns out that even for ratios of $w/w_c = 0,7$ good agreement is obtained between this simplified expression and that of a more accurate analysis. Figure 2.4.1 shows the typical motion of an electronic charge. It is clear that the average drift motion is along lines of constant potential.

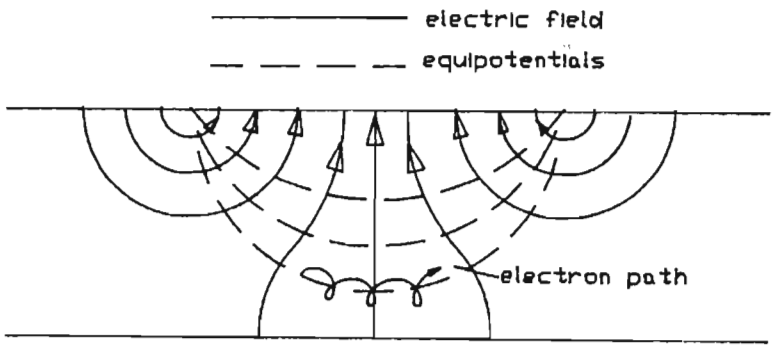

Fig. 2.4.1 : Electron Drift in a more complex Field Configuration

In the case of the magnetron the RF wave moves with respect to the structure. In this case a frame of reference moving at the velocity of the wave is chosen and again the RF field may be taken to appear static.

2.5 The Microwave Circuit

2.5.1 The Lumped Equivalent Circuit

For interaction to occur, the microwave circuit must present to the electron stream a retarding electric field which remains in synchronism with the electron stream over as many RF periods as is necessary for the electron to traverse the distance from cathode to anode. Synchronism with the charge determines the use of delay lines, and provided the orientation of the RF electric field is in a retarding direction, interaction will occur. The delay line must be of sufficiently low loss so that power may be extracted.

Generally the delay line may be represented as a series of interconnected resonator elements. The most simple lumped equivalent circuit representation of a resonator is the parallel combination of an inductor and a capacitor shown in Figure 2.5.1.

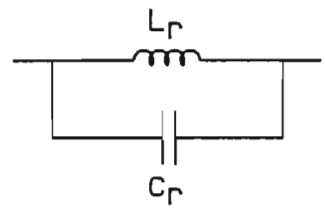

Figure 2.5.1 Single Resonator Equivalent Circuit

The anode block representation thus becomes the transmission line shown in Figure 2.5.2. Here C represents the distributed capacitance between anode and cathode.

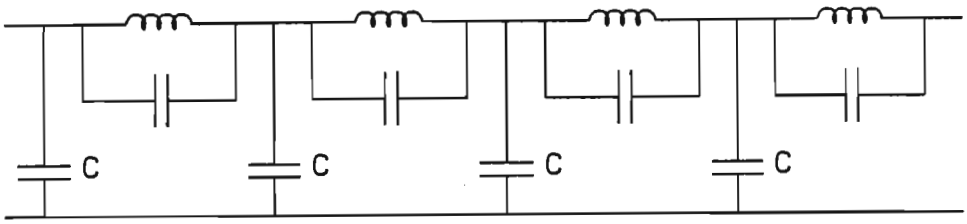

Figure 2.5.2 Anode Block Equivalent Circuit

2.5.2 General Resonator Characteristics

Figure 2.5.3(a) shows a view of the well known slot-and-hole resonator. Such a structure may resonate in an infinite number of modes; however it is useful to examine in detail only the mode that will give maximum interaction with the electron stream. Such a field will have no axial variation and will have an electric field component parallel to the resonator faces A and B.

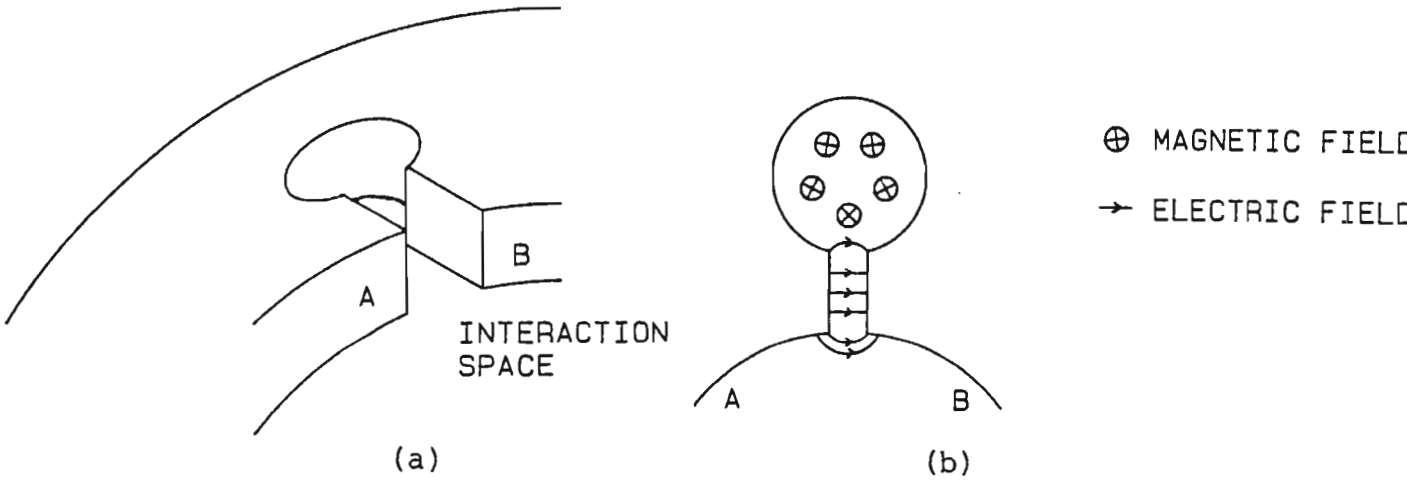

Figure 2.5.3 The Slot and Hole Resonator

Faces A and B can be thought of as the 'terminals' of the resonator through which the electron stream interacts. If only the mode having a tangential electric field with no axial variation is considered then since for free space

$$\bar{\nabla} \times \bar{E} + \partial\bar{B}/\partial t = 0 \qquad (2.5.1)$$

it follows that the magnetic field is axial and has no variation in that direction. Such a field configuration is shown in Figure 2.5.3(b) This circuit element will present some admittance Y_r to the interaction space. If this field is static the voltage between the vane tips A and B is given as

$$V = -\int_A^B \bar{E}\cdot d\bar{S} \qquad (2.5.2)$$

The admittance may be written in terms of the power as[45]

$$Y_r = 2P_s^*/V^2 \qquad (2.5.3)$$

P_s is the time average power transmitted across a closed surface S which may be written in terms of the Poynting vector as[46]

$$P_s = 1/2 \oint \bar{E} \times \bar{H}^* \cdot \bar{n}\, dS \qquad (2.5.4)$$

P_s^* is the complex conjugate of P_s. Thus (2.5.3) may be written as

$$Y_r = \frac{h \int \bar{E} \times \bar{H}^* \cdot \bar{n}\, dS}{\left|\int E \cdot dS\right|^2} \qquad (2.5.5)$$

This is of course only one of several definitions but one which has proved useful in analysing the characteristics of real resonator systems. In order to evaluate (2.5.5) Maxwell's equations must be evaluated for the particular configuration in question.

2.5.3 Admittance Calculations

Determining the admittance of the resonator has a number of uses. Firstly, the frequencies at which the admittance reduces to zero gives the resonant frequencies and secondly it provides the designer with a value for the characteristic admittance of the resonator block, thus facilitating power calculations. By assuming only field configurations corresponding to the pi-mode, the pi-mode resonant frequency may be determined.

Numerous alternative methods exist to calculate resonator admittances and hence resonator frequencies. However, in practice wavelength presetting is common practice to accurately determine the operating frequency. Thus analysis of the complete resonator system using field theory techniques is undesirable because of the reduced accuracy obtained; the cold resonant frequency should be an input parameter for any analysis.

2.5.4 The Slot and Hole Resonator

The slot and hole resonator of Figure 2.5.3 may be analysed by dividing the resonator into two separate components and determining the admittance of the slot terminated by the hole. Though lengthy the final admittance equations obtained[45] may be quickly evaluated by computer with appropriate expansion of the Bessel functions. This has been implemented by the author in the program CAMPA, and has been found to give fairly accurate results. The strapping dimensions may then be altered to give the correct measured frequency.

Typical strapped systems will offer relatively little additional inductance to the resonator operating in the pi-mode. The overall resonator equivalent inductance is thus obtained by a theoretical estimate of the resonator capacitance by use of a simple parallel plate capacitance formula. The capacitance 'contribution' is associated with the slot shown in Figure 2.5.3.

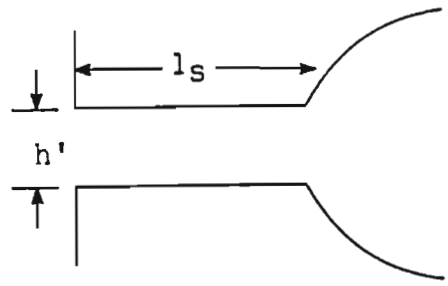

Figure 2.5.3 The Capacitive Slot

Thus

$$C_r = \frac{\varepsilon_o l_s L}{h'} \qquad (2.5.6)$$

Strapping alters the equivalent resonator capacitance considerably. Figure 2.5.4 shows the equivalent circuit of a resonator with strapping capacitance.

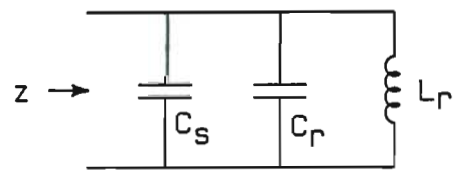

Figure 2.5.4 Resonator with Strapping

Thus the unstrapped resonant frequency w_u is given in terms of the equivalent circuit by

$$w_u = 1/(L_r C_r)^{1/2} \qquad (2.5.7)$$

This frequency may be calculated by field theory techniques as outlined in Section 2.5.3. With equation (2.5.6) giving an estimate for C_r an estimate may thus be obtained for L_r from equation (2.5.7).

The strapped resonant frequency w_s may be measured directly and is given by

$$w_s = 1/(L_r(C_r + C_s))^{1/2} \qquad (2.5.8)$$

This equation thus provides an estimate for the strapping capacitance, and finally the strapped resonator admittance may be estimated by

$$Y_r = 1/(w_s L_r) \qquad (2.5.9)$$

This method avoids the calculation of the strapping capacitance, though a good estimate may be obtained from the dimensions[47]. CAMPA uses a simplified form of the strapping capacitance by assuming the two straps to appear as a parallel plate capacitor.

2.5.5 The Anode Block Resonant Frequencies

Resonators of the type described in section 2.5.4 are connected in a ring to make up the anode circuit. Such a ring of resonators may oscillate at an infinite number of frequencies; Figure 2.5.5 shows a typical Brillouin diagram for an eight resonator unstrapped cavity block.

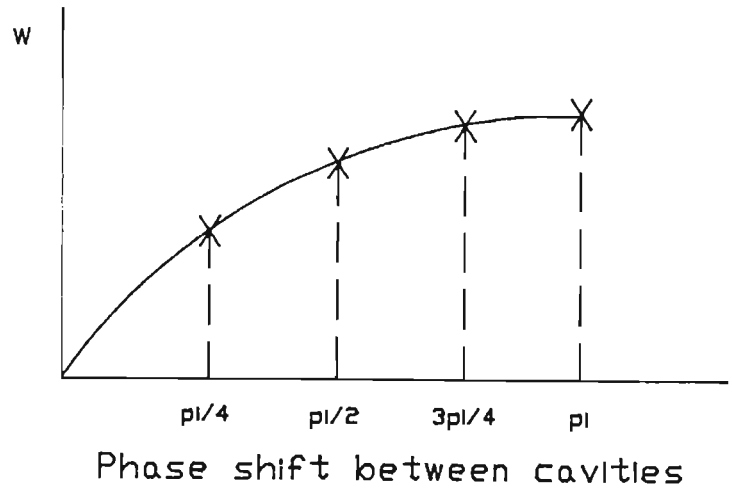

Fig. 2.5.5 : Brillouin Diagram for an eight-cavity Anode
(X - resonant frequency of the anode block)

The anode block is seen to be resonant in a number of modes depending on the phase shift per individual resonator. The prefered resonant

mode is the pi-mode where the phase shift between adjacent resonators is a half wavelength. The pi-mode is the only non-degenerate mode and tubes operating in this mode have the highest efficiency.

The electron stream circulating the anode may, if synchronous to the RF wave on the anode block, couple to it in such a way as to allow the transfer of energy from the dc electric field to the RF wave. However, the phase velocity of the RF wave, given by the slope of the line connecting the origin to the resonant point in Figure 2.5.5, does not change much for the different modes. The result is that the electron stream may couple to modes other than the pi-mode, resulting in random changes of operating frequencies or moding. A measure of stability of tube operation is the mode separation given by the difference between the pi-mode and the next resonant frequency.

$$\frac{\lambda_{(N/2-1)}}{\lambda_{\pi}} \qquad (2.5.10)$$

Strapping helps separate the pi and adjacent modes by effectively increasing the equivalent parallel capacitance of the resonant circuit in the pi-mode and not affecting the inductance. The result is to lower the resonant frequency of the pi-mode with respect to the other modes. Figure 2.5.6 shows a typical Brillouin diagram for a strapped eight cavity resonator system.

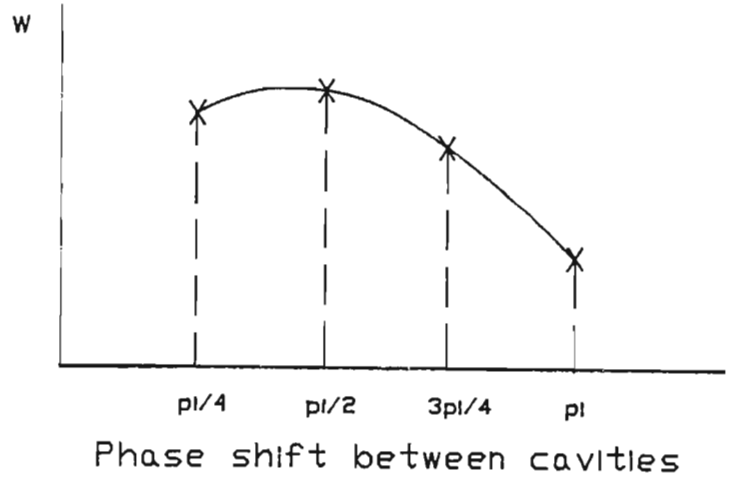

Fig. 2.5.6 : Brillouin Diagram for a Strapped Resonator

Now the phase velocity of the wave propagating in the pi-mode is substantially lower than that of the next resonant mode.

2.5.6 The Nature of the RF Wave

The resonant anode ring can support RF waves travelling in both directions. A resonant block with an RF signal fed in from an external sources will set up equal waves travelling in both directions which will combine to set up standing waves. However there is still some debate as to the nature of the waves in the oscillating tube. Experimental evidence appears to indicate the wave is strictly a travelling wave moving in one direction only, though it is beyond doubt that circuit asymmetry will result in reflected waves travelling in the opposite direction. However for the purposes of this model the wave travelling in the direction of the electron stream will be the only significant wave as far as energy exchange is concerned. The anode block will thus be presumed to support a wave travelling in the direction of the electron stream only; other wave components will be ignored.

2.6 The Output Circuit

A number of different output coupling systems may be used to extract energy from the magnetron. All have some preferred area of applicability, and all may be represented by the simplified lumped equivalent circuit shown in Figure 2.6.1. The output circuit consists of a coupling, an ideal transformer section and a load. This representation is valid at frequencies close to the pi-mode resonance[48]. Alternative though similar representations may be found elsewhere[1,36]. The coupling between the load and the resonator must be low enough so as to allow a suitable build-up of RF fields in the anode block, but still high enough allow sufficient extraction of energy. Too high a coupling will also allow excessive variation of the oscillation frequency as the load mismatch is changed. This change, termed frequency pushing, is the maximum frequency change measured as the load mismatch phase is changed over 360^{o} at a VSWR of 1,5:1.

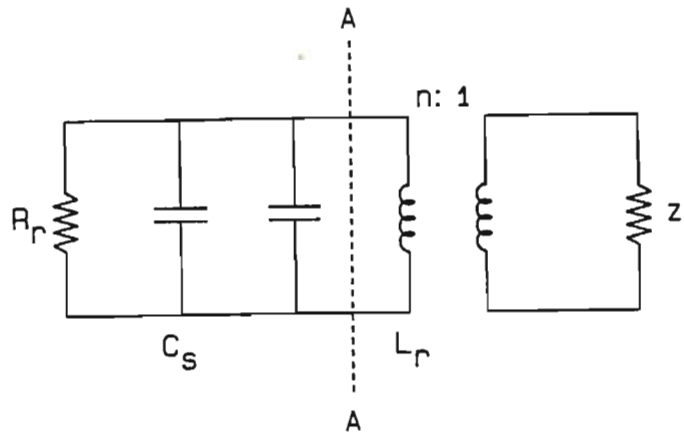

Figure 2.6.1 Output Equivalent Circuit

Analysing the output circuit provides the designer with important information, including the tube efficiency, pulling figure and output power.

2.6.1 Cold Tests and Q Values

Resistor R_r represents the resonator internal losses, Z is the terminating load and n represents the equivalent coupling transformer winding ratio. n is difficult to determine theoretically and depends on the coupling method employed, since different systems provide different ranges of coupling. In general, the coupling is adjusted during cold tests to give a required pulling figure.

The circuit quality factors are defined by :

Q_u - Unloaded Q representing anode block losses and is defined by :

$$Q_u = w_s L_r / R_r \qquad (2.6.1)$$

Q_e - External Q representing external losses and defined by :

$$Q_e = w_s L_r / R_{eq} \qquad (2.6.2)$$

where R_{eq} is the resistive component of the load transferred to the resonant circuit.

Q_l - Loaded (or overall) Q given by :

$$\frac{1}{Q_l} = \frac{1}{Q_e} + \frac{1}{Q_u} \qquad (2.6.3)$$

During cold tests the resonant circuit is connected to a signal generator via a matched transmission line and the resulting standing wave ratio is displayed as a function of frequency. The quality factors may then be determined in the usual way[1,48,49].

It can be shown[36,49] that the pulling figure is related to the load VSWR by the relation

$$\Delta F/F_o = 1/2\ (S - 1/S)/Q_e \qquad (2.6.4)$$

Here is S is the VSWR. For VSWR = 1,5:1 this becomes

$$\Delta F/F_o = 0,416/Q_e \qquad (2.6.5)$$

2.6.2 Experimental Determination of Equivalent Circuit Parameters

It is possible to determine the unloaded Q from a theoretically determined value of the strapping capacitance[50]. Thus, given the pulling figure and making use of equation (2.6.5) all the equivalent circuit parameters of Figure 2.6.1 may be theoretically determined.

Equation (2.6.5) is used to determine Q_e. The unloaded Q may be determined theoretically[50] or by measurement[47]. The loaded Q may then be determined from equation (2.6.3). Using (2.5.6) to estimate C_r and estimating w_u[50] gives L_r from equation (2.5.7).

A measured value for w_s and equation (2.5.8) gives $(C_r + C_s)$; equation (2.6.1) gives R_r and (2.6.2) gives R_{eq}. A knowledge of the actual value of Z (nominally 50 Ohm) gives n since

$$n^2 Re(Z) = R_{eq} \qquad (2.6.6)$$

The problem that arises however is that the determination of these parameters depends upon estimates based on a knowledge of the internal dimensions of the tube. It is not always possible to have access to these details, and ideally the parameters need to be determined from external measurements.

This is unfortunately not possible. The resonator component values referred to the load side may be determined by means of impedance measurements.

$$w_s = 1/(L_{eq}C_{eq})^{1/2} \qquad (2.6.7)$$

At resonance $Z = R_{eq} = R_r/n^2$ (2.6.8)

while $Q_u = w_s L_r/R_r$ see (2.6.1)

$$= w_s L_r/(R_{eq}n^2) \qquad (2.6.9)$$

Thus by measuring Q_u, w_s and R_{eq} an estimate for the resonator inductance in terms of n may be obtained :

$$L_r/n^2 = Q_u R_{eq}/w_s \qquad (2.6.10)$$

and so from (2.6.7)

$$C_r n^2 = w_s^2/(L_r/n^2) \qquad (2.6.11)$$

By purely external measurements it is thus only possible to determine the component values in terms of n.

2.7 Electron-RF Wave Interaction and Energy Exchange

What follows is a qualitative description of the interaction between the RF wave and the electron stream. Interaction will allow an exchange of energy from the dc electric field to the RF wave. Current will then flow from the Brillouin stream to the anode in charge

'spokes'. Conditions for interaction are established and the possible shape of these spokes discussed by examining a simplified planar magnetron configuration. Analytic formulations for the interaction processes are developed in Chapter 3.

2.7.1 The Brillouin Stream and Threshold Conditions

The Brillouin stream is a laminar flow of charge parallel to the cathode surface, and extends from the cathode surface to some maximum radius called the Brillouin radius r_b. The radial component of the charge velocity is zero, but the tangential velocity is obtained from energy considerations and depends on position :

$$eP_e = 1/2\ mv_x^2 \qquad (2.7.1)$$

This equation is obtained simply by considering that the potential energy lost in moving from the cathode surface to the laminar orbit must equal the kinetic energy gained. Increasing the static electric field increases r_b; increasing the magnetic field decreases r_b. If energy is extracted from the stream the stream will move away from the cathode and towards the anode. Energy will be extracted if a retarding electric field is allowed to interact with the stream. If the interaction persists the stream will continue moving towards the anode until it is intercepted by the anode.

The anode structure described in Section 2.5.4 will in resonance generate an electric field that can act as a retarding force on the electron stream. Since the anode may support a rotating wave, there exists the possibility that if a part of the electron stream is synchronised with this wave interaction may take place. The radius at which the electron stream angular velocity equals that of the RF wave is termed the synchronous radius r_s which may be less than the Brillouin radius. The anode voltage corresponding to synchronism between the electrons at the surface of the stream (at r_b) and the RF wave is termed the Hartree voltage V_s (also called the synchronous or threshold voltage). The velocity of the stream must at least be equal to the synchronous value so that if r_b exceeds r_s then charge between r_b and r_s is able to transfer energy to the rotating wave. Since the

phase velocity of the RF wave on the resonator block depends on the oscillation mode, the Hartree voltage will also depend on this mode; here, however, only the preferred pi-mode is considered.

2.7.2 The Interaction Conditions

Conditions for oscillation have thus been established : a) An anode delay-line circuit supporting a travelling RF wave in a mode so as to generate a suitable decelerating RF electric field within the interaction space; b) An output circuit capable of coupling out a significant amount of power but with a high enough Q to allow suitable RF voltage build up within the interaction space; c) An electron stream exhibiting Brillouin Flow near the cathode with $r_b > r_s$. These conditions will result in a flow of charge from cathode to anode with the charge potential and kinetic energy being transferred to the RF wave.

2.7.3 The Spoke Shape

Since the average drift velocity of the electrons can, to a close approximation, be taken to be along lines of constant potential, a clearer picture of charge movement in the presence of the RF electric field can be obtained by plotting the lines of constant potential in the interaction region. Examining the equations of motion of electrons in a planar magnetron[43] shows that if a set of coordinates are chosen that move with the RF wave charge moving at the same velocity as the wave will experience only forces due to the RF fields and not due to the static electric fields. If the RF voltage has a sinusoidal distribution along the anode, the potential distribution in the interaction space due to the RF voltage may be calculated by solving Laplace's equation (see Appendix A).

$$P_e(x,y) = V_{rf} \frac{\mathrm{Sinh}(\beta y)}{\mathrm{Sinh}(\beta d)} \sin(\beta x) \qquad (2.7.2)$$

The author has incorporated (2.7.2) into a computer program to generate plots of the equipotentials. Plotting lines of equipotential

over one wavelength according to equation (2.7.2) using typical tube parameters results in the diagram shown in Figure 2.7.1. Here the lines of constant potential have not been drawn to scale but will simply be used to illustrate the spoke shape. The axis y=h corresponds to the edge of the Brillouin hub and may be regarded as the electron supply plane travelling at the RF wave phase velocity while y=d corresponds to the anode surface. The shaded section corresponds to the electron movement from cathode to anode along these lines of constant potential, and will form a charge spoke. Note that this proposed spoke shape does not take into account the spoke space charge. This spoke is symmetrical and becomes narrower closer to the anode where the RF fields increase.

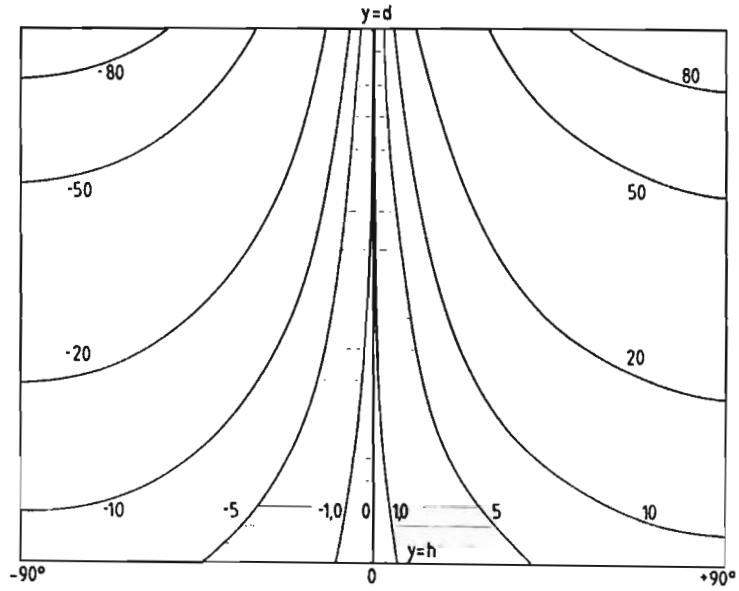

Figure 2.7.1 : Spoke Shape under Synchronous Conditions

If however the Brillouin stream does not move at the synchronous speed the spoke will be distorted as shown in Figure 2.7.2 (a) and (b). The degree of distortion will depend on the electron stream's departure from synchronism. As the departure from synchronism increases the charge will experience an increasing force due to the static dc electric field.

The spoke shape is indicated by the shaded portion of both Figure 2.7.2(a) and (b). Figure 2.7.2(a) has been drawn for $V_a = V_{rf}$ and Figure 2.7.2(b) has been drawn for $V_a = 3\ V_{rf}$. The spoke becomes asymmetrical and this lead or lag in the spoke relative to the RF wave results in a small magnetron oscillation frequency change. This undesirable change in frequency is called frequency pushing.

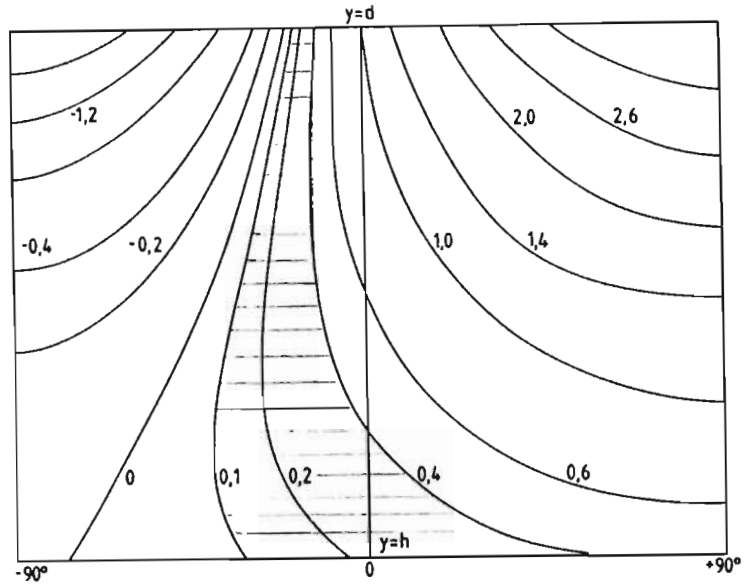

Figure 2.7.2(a) : Spoke Shape non-Synchronous Conditions

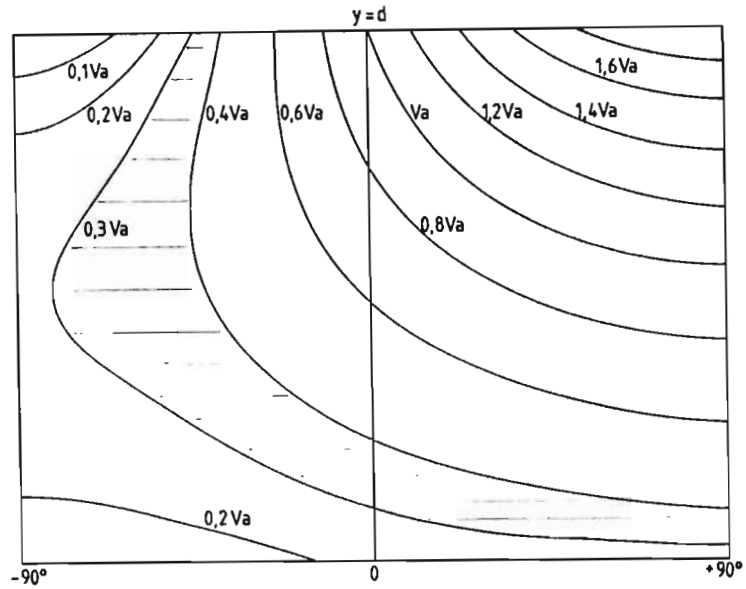

Figure 2.7.2(b) : Spoke Shape non-Synchronous Conditions

2.8 Conclusions

In this chapter the four components of the magnetron have been examined with the view of devising an analytic model in Chapter 3. The conditions of operation of a real magnetron have been examined and suitable simplifications made. The cathode is modelled as an ideal supply plane of electrons which under crossed field conditions allows

the formation of a laminar Brillouin stream of charge parallel to the cathode and anode surface. The RF field present in the interaction space during oscillation will act on the stream so as to allow the passage of charge from cathode to anode, the charge giving up potential energy and the RF wave grows in size. This passage of charge from cathode to anode will, to the first order, be along lines of equipotential in the form of 'spokes', the shape of which will depend on the degree of synchronisation between the Brillouin stream and the RF wave. RF energy is extracted by a suitable output circuit that has a low enough coupling to the resonators to allow the build up of RF fields.

It must always be born in mind that these simplifications will result in deviations of the model from the real device. If however the emphasis is on overall device performance and not individual trajectory prediction, good agreement may still be obtained.

CHAPTER 3

THE DEVELOPMENT OF A LUMPED-SPOKE MAGNETRON MODEL

Summary:
- Predicted I-V characteristics chapter 5.4
- High Power, High performance water load.

interaction equations are examined in
is developed, based on the interaction
.

eshold voltage is used to determine the
rmed in the interaction space. This
d by Welch[8], who used the equivalent
de to formulate the threshold criteria.
oncept is expanded by the author to a
mining the total electric fields at the
. Sections 3.3.5 to 3.3.7 introduce the
ula without the effects of space charge
e space charge effects in the threshold
e base of the electron spoke.

current flow in the spoke to determine
spoke current is limited by the spoke
tric fields and the space charge forces
e model has here been improved by the
ke current at the base of the spoke. The
ly enters into the equation as a second
amines the energy losses, and knowing the
wer an overall equation may be formulated
he conservation of energy. The magnetron
s may thus be determined and these equations
the author in the computer program CAMPA[47]
n Performance Analysis) as outlined in section

d the energy balance equation was first used by
del the cylindrical magnetron. More lately
Bayburin extended the model by reducing the dependency on

empirical formulations. In both cases the Welch's criteria was used in its voltage format and space charge fields were not included. Making use of the Welch criteria in the field format is a unique contribution to the modelling of magnetrons. Dependency on empirical formulae is reduced and space charge effects are taken into account.

3.2 Assumptions

a) For the sake of mathematical simplicity, the linear magnetron is analysed. In section 3.7 and Appendix D appropriate changes are made to the equations where the cylindrical magnetron differs significantly from its linear counterpart.

b) The system is two dimensional. There is no axial variation of fields, and all charge movement is in a two dimensional plane. This is consistent with the nature of the structure and the arguments presented in section 2.5.2.

c) The system is non-reentrant. This is consistent with the conditions at the cathode as outlined in section 2.4.1. The Brillouin single stream state, as described in section 2.3.2, is assumed within the subsynchronous space charge.

d) Electrons in the interaction space are presumed to drift with an average velocity $(\bar{E} \times \bar{B})/|\bar{B}|^2$ where $\bar{E}$ is the total electric field seen by the electron and $\bar{B}$ is the uniform static magnetic field. This has been discussed in section 2.4

e) The equations describing the RF electric fields within the interaction space are determined without taking into account the distortion introduced by the space charge.

f) The electric fields are presumed to change slowly enough to allow the use of quasi-static analysis.

g) Relativistic effects are ignored.

3.3 Electron Bunch Initiation

3.3.1 The Coordinate System

Figure 3.3.1 shows the general linear coordinate system used. The cathode is held at zero potential and the anode is biased positive. The dc electric field is thus in the negative-y direction. The electron stream exhibits Brillouin flow and at the surface of the cathode y=0; the magnetic field is into the page and the electrons move from left to right.

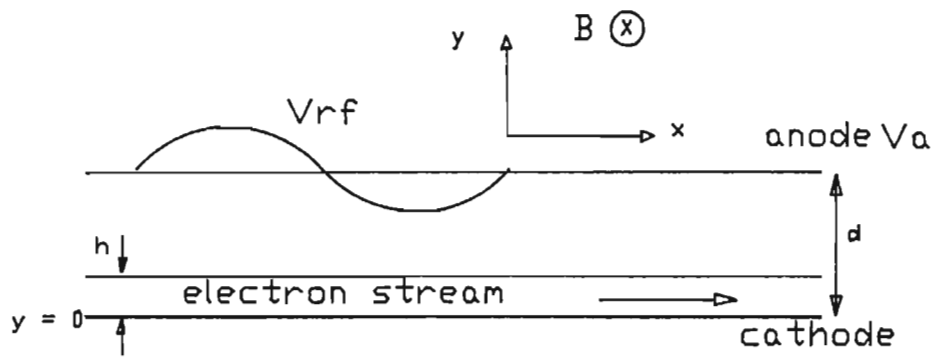

Figure 3.3.1 General Coordinate System

The anode-cathode spacing is d and the height of the Brillouin stream is h. The electron cloud charge density is negative, and in all analysis the direction of current flow is opposite to that of the movement of the electrons.

3.3.2 The Threshold Voltage

If the space charge cloud extends to a thickness h and the cathode-anode spacing is d then it may be shown that (see for example[44] or Appendix B and[50]) the anode voltage V_a is given by

$$V_a = (e/m)B^2h(d - h/2) \qquad (3.3.1)$$

All the other symbols have their usual meaning.

This determines the anode-cathode potential which must be applied in order to maintain an electron hub of thickness h. At the boundary and within the hub the y component of the electron velocity is zero.

If a small RF wave propagates along the anode circuit the phase velocity is

$$v_p = w/\beta \qquad (3.3.2)$$

where w is the wave frequency and β is the circuit propagation constant :

$$\beta = 2\pi/\lambda_c \qquad (3.3.3)$$

λ_c is the circuit wavelength. The velocity of the electrons at the swarm boundary is eBh/m and thus for synchronism the speed of propagation of the wave must equal that of the electrons at the edge of the stream :

$$eBh/m = w/\beta \qquad (3.3.4)$$

If P is the circuit period then for pi-mode operation

$$\beta = \pi/P \qquad (3.3.5)$$

Thus (3.3.4) becomes

$$(e/m)Bh = wP/\pi \qquad (3.3.6)$$

Substituting from (3.3.1) gives

$$V_{as} = wBd/\beta - (m/2e)(w/\beta)^2 \qquad (3.3.7)$$

This is the threshold condition (or Hartree Voltage) for the linear magnetron. For the electrons at the boundary of the stream to be in synchronism with the moving wave the anode voltage must be set to V_{as} as given in (3.3.7). Under these conditions a small retarding electric field will result in electrons moving from the synchronous boundary to

the anode. If the voltage exceeds V_{as}, the speed of the outer electrons will increase and become greater than the speed of the RF wave. Under these conditions synchronism will be forced by the increased RF retarding (focussing) fields. Thus favourable interaction will occur if

1) the anode voltage equals or exceeds the synchronous voltage and

2) a small retarding RF field exists over some portion of the RF period.

These two conditions are necessary and sufficient for interaction.

3.3.3 The Welch Voltage Criteria

Figure 3.3.2 shows a RF voltage V_{rf} superimposed on the anode voltage V_a. The RF wave is presumed a sinusoid; in practice it may deviate substantially from this shape but V_{rf} may be considered to represent the fundamental of the actual periodic voltage function propagating on the anode circuit.

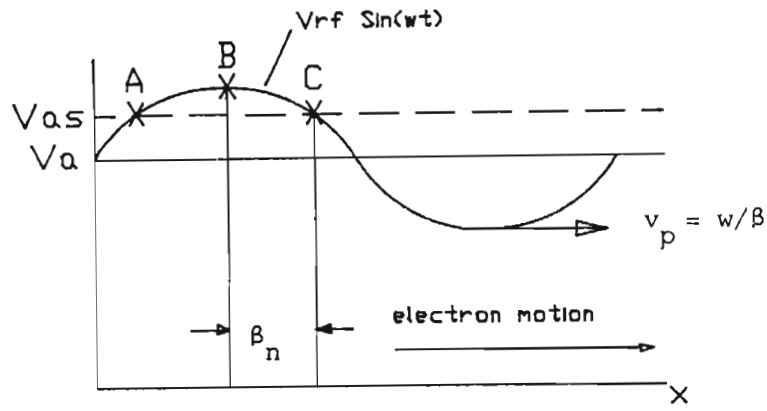

Figure 3.3.2 RF Voltage Representation

By conditions 1) and 2) of section 3.3.2 if the total anode voltage exceeds V_{as} and the field in that region is retarding, interaction will occur. Since the electron swarm moves left to right in this representation, a retarding field will exist in region BC as shown. The portion of the RF cycle for which the conditions are satisfied or

for which the electrons will interact and drift towards the anode is shown as the phase angle β_n. Thus

$$\beta_n = \text{acos}((V_{as} - V_a)/V_{rf}) \qquad (3.3.9)$$

This defines the phase angle as a function of operating conditions and the RF potential V_{rf}. For convenience (3.3.9) is termed the Welch Voltage Criteria, abbreviated to WVC.

3.3.4 The Threshold Field Criteria

The Welch Voltage Criteria was obtained by a simple superposition of voltages; this analysis is correct only if the field spreading effects of the RF field are minimised, ie. if the anode - cathode spacing is much smaller than the anode circuit periodicity. More accurately, favourable interaction and spoke formation will occur when the electric field at the boundary of the electron swarm exceeds the threshold field. In practice this makes a substantial difference to the analysis of practical tubes since in most cases the anode-cathode spacing is comparable to the RF periodicity.

In order to derive the field threshold conditions for the linear magnetron, Laplace's equation is solved subject to the boundary conditions of Figure 3.3.1 but ignoring the electron stream (see Appendix A, equation (A.5)).

$$P_e = V_{rf} \frac{\text{Sinh}(\beta y)}{\text{Sinh}(\beta d)} \sin(\beta x) \qquad (3.3.10)$$

The y-component of the RF electric field is thus

$$E_y^{rf} = - V_{rf} \beta \frac{\text{Cosh}(\beta y)}{\text{Sinh}(\beta d)} \sin(\beta x) \qquad (3.3.11)$$

while, if h << d, the static dc field is given by

$$E_y^{static} = -V_a/d \tag{3.3.12}$$

At the synchronous hub y=h thus the total electric field at the surface of the hub is

$$-E_y(h) = V_a/d + V_{rf} \frac{\beta \mathrm{Cosh}(\beta h)}{\mathrm{Sinh}(\beta d)} \sin(\beta x) \tag{3.3.13}$$

On the other hand, synchronism determines that the threshold field must equal

$$E_y^{th} = -(e/m)B^2 h \tag{3.3.14}$$

but h = wm/(βeB) for synchronism, thus the threshold condition becomes

$$-E_y^{th} = \frac{eB^2 wm}{m \beta eB} = Bw/\beta \tag{3.3.15}$$

Thus the threshold condition is exceeded if

$$V_a/d + \beta V_{rf} \frac{\mathrm{Cosh}(\beta h)}{\mathrm{Sinh}(\beta d)} \sin(\beta x) > Bw/\beta \tag{3.3.16}$$

Equation (3.3.16) is the Threshold Field Condition for the linear magnetron. In determining this relation, we have assumed that the space charge in the Brillouin hub has little effect on the fields. This simplification is necessary to reduce the mathematical complexity of the analysis and is consistent with approximations made further on in this chapter.

3.3.5 The Welch Field Criteria

From (3.3.16) substituting for h from (3.3.6) spoke formation will occur over a phase

$$\beta_n = \text{acos}\{(Bw/\beta - V_a/d)\frac{\text{Sinh}(\beta d)}{\text{Cosh}(wm/eB)\beta V_{rf}}\} \qquad (3.3.17)$$

Again, for convenience (3.3.17) is termed the Welch Field Criteria, abbreviated to WFC.

The WFC may be written in a more recognisable form similar to the WVC by making some simplifications. Firstly, if the product βd is small $\sinh(\beta d)$ may be replaced by βd. Then, since the Cyclotron frequency w_c given by

$$w_c = eB/m >> w \qquad (3.3.18)$$

is considerably greater than the frequency of oscillation w, we may write

$$\text{Cosh}(wm/eB) \approx 1 \qquad (3.3.19)$$

Therefore (3.3.17) becomes

$$\beta_n = \text{acos}\{(Bwd/\beta - V_a)/V_{rf}\} \qquad (3.3.20)$$

Equation (3.3.20) may be compared to (3.3.7), and noting that

$$V_{as} \approx Bwd/\beta$$

reduces (3.3.20) to the WVC equation (3.3.9)

In the case where βd is not small, (3.3.17) may be approximated by

$$\beta_n = \text{acos}\{(V_{as} - V_a)(1/V_{rf})\frac{\text{Sinh}(\beta d)}{\beta d}\} \qquad (3.3.21)$$

The difference between the Welch Field Criteria and the Voltage Criteria is thus a factor F where

$$F = \mathrm{Sinh}(\beta d)/\beta d \qquad (3.3.22)$$

As a practical example, if λ_c = 10,5mm and d = 4,3mm F = 2.53. The WVC thus holds as long as βd is small, or as long as the anode-cathode spacing is small compared to the circuit wavelength.

3.3.6 Brillouin hub modulation by RF fields

In establishing the criteria for spoke formation, the RF voltage was presumed small enough not to affect conditions at the Brillouin hub surface. At large RF voltages however, the fields may be sufficiently large to alter conditions at the hub surface. A RF field will result in a modulation of the hub thickness h, as well as a modulation of the stream velocity.

The effect that this has on the threshold criteria may be estimated by examining the intersection of two contours. The first contour is the edge of the Brillouin hub y = h(x) and the second is the threshold contour y = T(x). The threshold contour is the contour within the Brillouin stream at which the electron x velocity is synchronised with the RF wave.

The Brillouin hub contour h(x) may be found by equating the y-directed electric field at the edge of the swarm with the imposed fields. (see Appendix B)

Thus, the electric field at the edge of the swarm must be

$$E_y(x) = -eB^2h(x)/m \qquad (3.3.23)$$

while the fields due to the static and RF fields in the y direction may be approximated by

$$-E_y(x) = V_a/d + V_{rf}\,\beta\frac{\mathrm{Cosh}(\beta y)}{\mathrm{Sinh}(\beta d)}\,\mathrm{Sin}(\beta x) \qquad (3.3.24)$$

Thus,

$$y = h(x) = m/(eB^2)\,\left(V_a/d + V_{rf}\,\beta\frac{\mathrm{Cosh}(\beta y)}{\mathrm{Sinh}(\beta d)}\,\mathrm{Sin}(\beta x)\right) \qquad (3.3.25)$$

Again, when evaluated near the cathode, the Cosh term approximates unity for practical tubes. The threshold contour T(x) may be estimated by examining the x-directed electron velocity v_x given by $-E_y/B$ and equating that to the RF wave phase velocity. Thus

$$y = T(x) = m/(eB^2)\,\left(Bw/\beta - V_{rf}\,\frac{\beta\mathrm{Sin}(\beta x)}{\mathrm{Sinh}(\beta d)}\right) \qquad (3.3.26)$$

The two functions h(x) and T(x) are illustrated in Figure 3.3.3

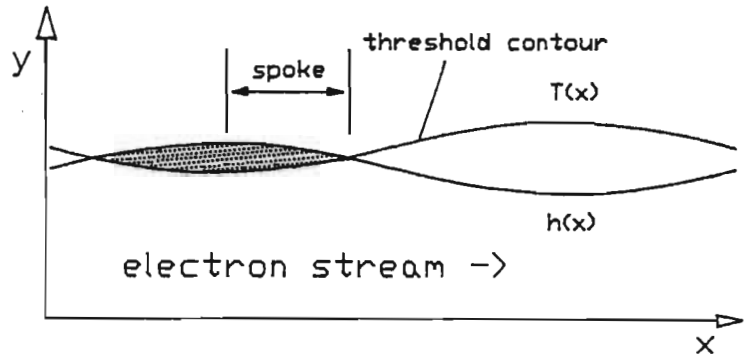

Fig. 3.3.3 : An Illustration of Contours T(x) and h(x)

Threshold conditions are exceeded where h(x) > T(x) as shown by the shaded portion of Figure 3.3.3. Considering the intersection of the two contours h(x) = T(x) gives

$$\mathrm{Sin}(\beta x) = (wB/\beta - V_a/d)\,\frac{\mathrm{Sinh}(\beta d)}{2V_{rf}\;\beta} \qquad (3.3.27)$$

Since the spoke will form only in the area of a retarding x-directed electric field the phase of spoke formation will be given by

$$\beta_n = \text{acos}\left[(V_{as} - V_a)\frac{\text{Sinh}(\beta d)}{V_{rf}\beta d}\right] \qquad (3.3.28)$$

This is an alternative method of obtaining the WFC; comparing this to equation 3.3.21 shows that an additional factor of 1/2 has been introduced due to the modulation of the Brillouin hub and the synchronous contours.

3.3.7 The effect of Anode Vane Shapes on the Threshold Criteria

The sinusoidal RF potential distribution used in the analysis thus far is an approximation (see Figure 3.3.2). The vane shapes play a role in shaping the fields as shown in Figure 3.3.4. The anode circuit phase constant β as well as the slot gap determine the interaction space RF fields. The voltage waveform at the anode face will tend to be stepped as shown, and not sinusoidal.

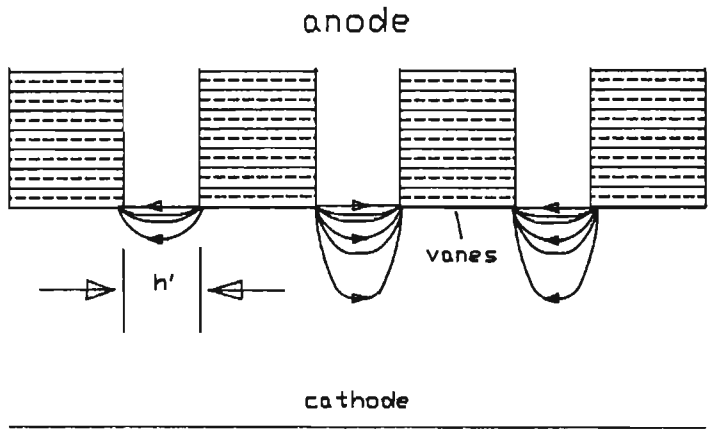

Fig. 3.3.4 : Anode Vane Shape Effect on RF Electric Fields

The peak electric field in the interaction space thus follows a $(V_{rf}/h')\sin(a)/a$ relation[54], where a is a constant depending on the ratio between slot width and circuit period. More precisely,

$$E_p^{rf} = V_{rf}\frac{\text{Sin}(\pi h'/P)}{h'(\pi\, h'/P)} \qquad (3.3.29)$$

This may be compared to the peak field in the interaction space for a

sinusoidal waveform of $E_p^{rf} = \beta V_{rf}$. This alters the WFC as follows :

$$\beta_n = \text{acos}\left[(V_{as} - V_a)\frac{\text{Sinh}(\beta d)\ h'(\pi h'/P)}{V_{rf}\ 2d\ \ \text{Sin}(\pi h'/P)}\right] \qquad (3.3.30)$$

3.4 Space Charge Effects

The spoke charge in the interaction region will reduce the field at the hub surface, thus reducing the spoke phase angle β_n given in equation (3.3.30). In order to estimate the space charge effects the space charge distribution needs to be known, which in turn depends upon the spoke width. Iterative techniques thus need to be employed to solve Poisson's equation in the interaction space. Again, matters are simplified by assuming that the presence of the spoke space charge does not significantly alter the shape of the RF fields in the interaction space.

We initially simplify matters by presuming some reasonable shape for the spoke and then equating it to an equivalent line charge located at the centre of the spoke, half way between the anode and the cathode. This will then be extended to more realistic spoke shapes.

3.4.1 A Rectangular Spoke Shape

It may be shown[55] that the spoke space charge density remains fairly constant throughout the spoke and is given by the Brillouin Hub density given by (see Appendix B)

$$\rho = -e\varepsilon_o B^2/m \qquad (3.4.1)$$

Since the spoke is of length d, height L and width β_n/β the total spoke charge is given by

$$q = \rho L \beta_n d/\beta \qquad (3.4.2)$$

or substituting

$$q = -(e/m)\,\varepsilon_o B^2 L d\beta_n / \beta \qquad (3.4.3)$$

If q is represented by a line charge L long situated halfway between anode and cathode in the centre of the spoke the electric field at the base of the spoke is (see Appendix C, equation (C.4))

$$E_y^{sc} = -1{,}6\rho_l L/(\pi\varepsilon_o d(L^2 + d^2)^{1/2})$$

or if d << L this reduces to the formula for an infinite line charge (equation C.3)

$$E_y^{sc} = -1{,}6\rho_l/(\pi\varepsilon_o d) \qquad (3.4.4)$$

where

$$\rho_l = q/L = -(e/m)\,\varepsilon_o B^2 d\beta_n / \beta \qquad (3.4.5)$$

Thus

$$E_y^{sc} = 1{,}6(e/m)B^2 L\beta_n/\{\pi\beta(L^2 + d^2)^{1/2}\} \qquad (3.4.6)$$

It is quite clear that the estimate for the space charge fields depends critically upon the spoke shape. The spoke will not remain a constant width if the charge density is constant. Charge will drift along lines of constant potential.

A qualitative account of the spoke shape has already been given in Chapter 2; a suitable analytic approximation will now be made.

3.4.2 Computing Spoke Shape from RF Fields

If the charge moves with a velocity $(\bar{E} \times \bar{B})/|\bar{B}|^2$, the y- component of the electron velocity may be written as

$$v_y = E_x/B = -V_{rf}\,\beta\,\frac{\mathrm{Sinh}(\beta y)}{B\,\mathrm{Sinh}(\beta d)}\cos(\beta x) \qquad (3.4.7)$$

The spoke will thus take on a shape similar to that shown in Figure 3.4.1

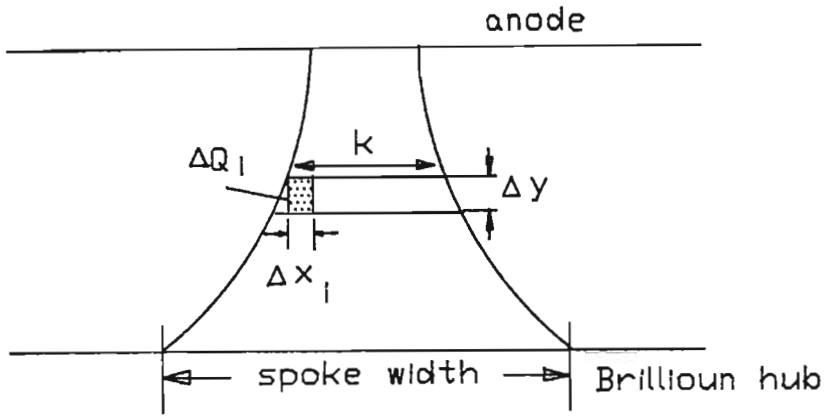

Figure 3.4.1 Spoke Shape based on Equipotentials

As before, the space charge density is assumed constant thoroughout the spoke, thus the small charge packet ΔQ_i may be written as

$$\Delta Q_i = \Delta x_i \Delta y L \rho \qquad (3.4.8)$$

and the current flowing across Δx_i is

$$I_i = \Delta Q_i / \Delta t_i \qquad (3.4.9)$$

where Δt_i is the time it takes for charge to move a distance Δy at x_i. Thus,

$$I_i = L \rho \quad \Delta x_i v_y \qquad (3.4.10)$$

where v_y is the y-direction charge velocity at (x_i, y)

The spoke shown in Figure 3.4.1 is symmetrical about x = P when the spoke phase $\beta_n = \pi$; in this case the spoke extends from x = P - k/2

to x = P + k/2. Thus the total spoke current may be expressed as an integral (if Δx_i is small enough) as

$$I^{spoke} = -\rho L \int_{P-k/2}^{P+k/2} V_{rf} B \beta \frac{Sinh(\beta y)}{Sinh(\beta d)} \cos(\beta x) dx \qquad (3.4.11)$$

Since the spoke current is constant and independant of y, the spoke width k may be expressed in terms of a constant A independant of y :

$$k = (2/\beta)\ asin(A/sinh(\beta y)) \qquad (3.4.12)$$

where

$$A = (I^{spoke} B\ Sinh(\beta d))/(2\rho L V_{rf}) \qquad (3.4.13)$$

Equation (3.4.12) thus gives the spoke width as a function of y.

For many practical substitutions (3.4.12) may be approximated by

$$k = 2A/(Sinh(\beta y)\beta) \qquad (3.4.14)$$

Figure 3.4.2 shows spoke shape drawn on the basis of equation (3.4.14). As a comparison, Welch's square[8] and Vaughan's triangle[7] are superimposed.

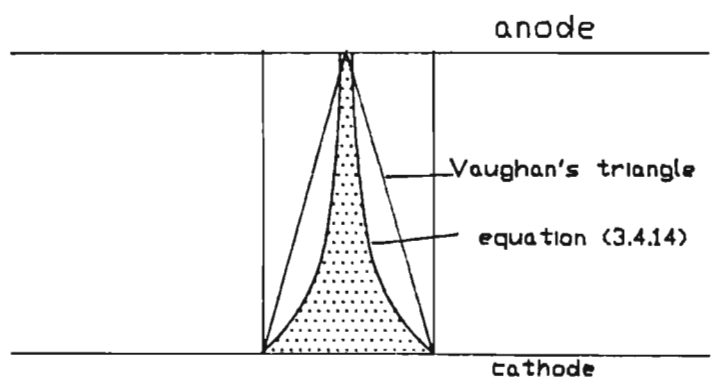

Fig. 3.4.2 : Spoke Shape Comparison

3.4.3 Spoke Charge

Equation (3.4.14) may be simplified in order to calculate the total charge Q^{spoke} of the spoke. If y is sufficiently small (close to the base of the spoke) then using (3.4.14) and setting y = h the constant A is evaluated at the base of the spoke :

$$A = \beta_n/2\beta h \qquad (3.4.15)$$

Thus

$$k = \beta_n/(\beta^2 h \, \mathrm{Sinh}(\beta y)) \qquad (3.4.16)$$

If however y is large (closer to the anode) equation (3.4.14) may be approximated by

$$k = 4A \, e^{-\beta y}/\beta \qquad (3.4.17)$$

When βy is less than 1,2 this approximation will introduce an error in excess of 10%; however if (3.4.17) is used directly to evaluate the constant A (instead of using (3.4.13)) at the base of the spoke, then

$$A = (\beta_n/4)e^{\beta h} \qquad (3.4.18)$$

and thus (3.4.17) becomes

$$k = (\beta_n/\beta)e^{\beta(h - y)} \qquad (3.4.19)$$

This spoke deviates somewhat from (3.4.14), but is a better aproximation than a triangular shaped spoke. The spoke charge may then be easily calculated by integrating

$$Q^{spoke} = \rho L(\beta_n/\beta^2)(1 - e^{\beta(h-d)}) \qquad (3.4.20)$$

3.4.4 The Spoke Shape Factor

Equation (3.4.19) merely serves the purpose of determining the shape of the spoke for the purposes of calculating spoke charge. A closer approximation to the ideal spoke shape may be obtained by writing the equation as

$$k = (\beta_n/\beta)e^{\beta S(h - y)} \qquad (3.4.21)$$

where S is a spoke 'shape factor'.

For example, setting S = 1,6 gives a spoke shape closely following that of equation (3.4.14). This is illustrated in Figure 3.4.3.

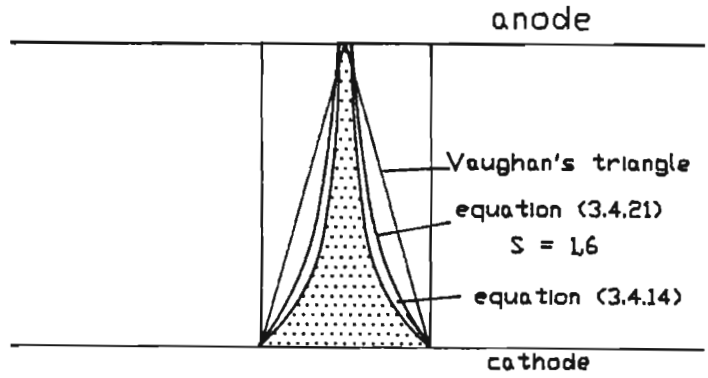

Fig. 3.4.3 : Comparison of Spoke Shapes using the Spoke Shape Factor

Carrying the shape factor through to the spoke charge calculations,

$$Q^{spoke} = \rho L\beta_n/(\beta^2 S)(1 - e^{S\beta(h - d)}) \qquad (3.4.22)$$

If d >> h (which is usually the case in practice) then (3.4.22) could be approximated by

$$Q^{spoke} = \rho L\beta_n/(\beta^2 S) \qquad (3.4.23)$$

3.4.5 Space Charge Field Effects

Following the method of section 3.4.1 the effect of the spoke space charge may be estimated by representing the spoke charge as an equivalent line charge L long situated in the centre of the spoke halfway between anode and cathode. In addition, since in most practical power tubes d << L the equivalent electric field due to space charge acting on the base of the spoke may be taken to appear like an infinite line charge. Thus

$$E_y^{sc} = -1,6\rho\beta_n/(\beta^2 S\pi\varepsilon_o d) \qquad (3.4.24)$$

If the magnetic field is held constant and the tube oscillates in the pi-mode at a constant frequency, the space charge field is dependant upon the spoke phase only. Thus

$$E_y^{sc} = S_c\beta_n \qquad (3.4.25)$$

where S_c is a constant. This field is taken to be uniform across the base of the spoke.

3.4.6 Inclusion of Space Charge Effects into the WFC

Space charge effects may be included into the WFC equation (3.3.17) by the use of superposition. Equation (3.3.29) is thus written as

$$\beta_n = \text{acos}\left[\frac{(V_{as} - V_a + V_{sc})}{V_{rf}}\frac{\text{Sinh}(\beta d)\ h'(\pi h'/P)}{2d\ \ \text{Sin}(\pi h'/P)}\right] \qquad (3.4.26)$$

where

$$V_{sc} = 1,6\,\rho\beta_n/(\pi S\beta^2\varepsilon_o) \qquad (3.4.27)$$

is the equivalent space charge voltage. Equations (3.4.26) and (3.4.27) thus define the width of the spoke base in the presence of space charge forces.

3.5 Spoke Current

As indicated in section 3.4.2 the spoke current is a constant independent of the position between anode and cathode. However it is possible to improve the model accuracy by careful selection of the position that the current is calculated. In order to calculate the current the spoke width and the x-directed electric fields need to be known at this point.

3.5.1 Calculating Current between Anode and Cathode

The spoke current I^{spoke} may be calculated as

$$I^{spoke} = \rho L k v_y \qquad (3.5.1)$$

where v_y is the velocity (in the y-direction) of the spoke charge given by

$$v_y = E_x^{rf}/B \qquad (3.5.2)$$

The problem is one of determining the RF electric field and the spoke width at some appropriate point between anode and cathode. The calculation should yield the same result for all positions between anode and cathode, but careful selection of y will improve the accuracy of the final result. The current may be evaluated at the base of the spoke since here the spoke width is a known quantity and does not depend upon spoke shape. Evaluating the spoke current at the anode introduces some uncertainty in the spoke width since here it does

depend on spoke shape. Vaughan[7] estimates the spoke current 1/3 of the distance between the anode and the Brillouin hub by assuming a triangular spoke shape. Here again the errors are mainly as a result of spoke shape uncertainty.

3.5.2 Current Calculation at the base of the spoke

The advantage of calculating the current at the base of the spoke is that the shape of the spoke enters into the expression only as a second order effect through the space charge forces in the WFC equation (3.4.26). It will further be shown in Chapter 5 that this results in a model that is consistent with measured results and is a closer representation of what is actually happening within the device; the current is drawn directly from the base of the spoke and thus should be calculated there. The uncertainty here however is the RF field since the fields depend on y and the presence of the space charge within the Brillouin hub and the spoke. The calculations of the RF fields in Appendix A do not take the space charge into account, and thus some error will be introduced (refer to the assumption (e), section 3.2). Inclusion of space charge directly in the calculation of the RF fields makes the analysis considerably more complex, and has not been included here. But, as will be shown in Chapter 5, the resulting simplified model still gives good agreement with measured results.

The x-directed RF electric field is given by equation 3.4.7, and since βy is small at the base of the spoke may be approximated by

$$E_x = -E_p^{rf} \beta y \frac{\mathrm{Cos}(\theta)}{\mathrm{Sinh}(\beta d)} \qquad (3.5.3)$$

where θ is the angle defining the centre of the spoke or

$$\theta = \pi/2 + \beta_n/2 \qquad (3.5.4)$$

The spoke current is therefore obtained from equations (3.5.1) - (3.5.4). The anode current may then be obtained by multiplying by the number of spokes N/2.

3.6 The Energy Balance Equation

In the previous sections it has been necessary to introduce two parameters internal to the tube operation, viz. the RF voltage V_{rf} and the spoke phase β_n. Equation (3.3.27) links these two parameters to the anode voltage V_a, while equation (3.5.1) links these two parameters to the spoke current I^{spoke}. The energy balance equation thus provides the additional link enabling the anode voltage to be expressed as a function of anode current. The input power is related to the output power and the power losses :

$$V_a I_a = P_c + P_a + P_u + P_x \qquad (3.6.1)$$

where P_c represents cathode back-heating losses
P_a represents anode (electron bombardment) losses
P_u represents anode resistive losses
P_x represents the output power

3.6.1 Anode Resistive Losses and Output Power

In terms of the anode block equivalent circuit we may write :

$$Y_o = N/Z \qquad (3.6.2)$$

$$G_e = Y_o/Q_e \qquad (3.6.3)$$

$$G_u = Y_o/Q_u \qquad (3.6.4)$$

$$G_l = Y_o/Q_l \qquad (3.6.5)$$

where the symbols have their usual meaning.

The external Q may be expressed in terms of the tube pulling figure (see equation (2.6.4))

$$Q_e = 0{,}416\ F/F_p \qquad (3.6.6)$$

where F = centre frequency

F_p = pulling figure

Thus the output power may be expressed in terms of the load conductance

$$P_x = 1/2\ V_{rf}^2 G_e \qquad (3.6.7)$$

and the anode resistive losses as

$$P_u = 1/2\ V_{rf}^2 G_u \qquad (3.6.8)$$

3.6.2 Anode Block Losses

Anode block losses result from either resistive losses (equation (3.6.8)) or from electron bombardment losses at the anode vanes. The y-component of velocity v_y is given by equation (3.4.7) and depends on the RF fields. The impact energy of one electron may be obtained from its y direction velocity given by

$$v_y^{imp} = -V_{rf}(\beta/B)\cos(\theta) \qquad (3.6.9)$$

Here θ is the phase angle defining the centre of the spoke. The x - direction impact velocity is made up of two components; the first component is due to the cycloidal motion of the electron and the second is due to the electron circulation at the synchronous velocity.

The synchronous velocity is given by

$$v_x^{sync} = w/\beta \qquad (3.6.10)$$

The rotational velocity of the electron may be estimated from the work of Shimizu[56] and Nishimaki[57].

The frequency of rotation of the electron is given by

$$w_1 = w_b + (w_b^2 - w_a^2)^{1/2} \qquad (3.6.11)$$

where

$$w_b = eB/(2m) \qquad (3.6.12)$$

and

$$w_a^2 = 2eV_a/(m(r_a^2 - r_c^2)) \qquad (3.6.13)$$

The radius of rotation is given by

$$R_1 = w_2 r_c/(w_1 - w_2) \qquad (3.6.14)$$

where

$$w_2 = w_b - (w_b^2 - w_a^2)^{1/2} \qquad (3.6.15)$$

The velocity of electron rotation is given by

$$v_x^{rot} = w_1 R_1 \qquad (3.6.16)$$

The equivalent impact voltage is thus

$$V_a^{loss} = m/(2e)\{(v_x^{sync} + v_x^{rot})^2 + (v_y^{imp})^2\} \qquad (3.6.17)$$

and finally the anode power loss as a result of electron bombardment is

$$P_a = V_a^{loss} I_a \qquad (3.6.18)$$

3.6.2 Cathode Back-Heating

Cathode back-heating is as a result of electrons in the swarm gaining energy from the RF wave and bombarding the cathode. Figure 3.6.1 shows the x and y RF fields in relation to the spoke formation.

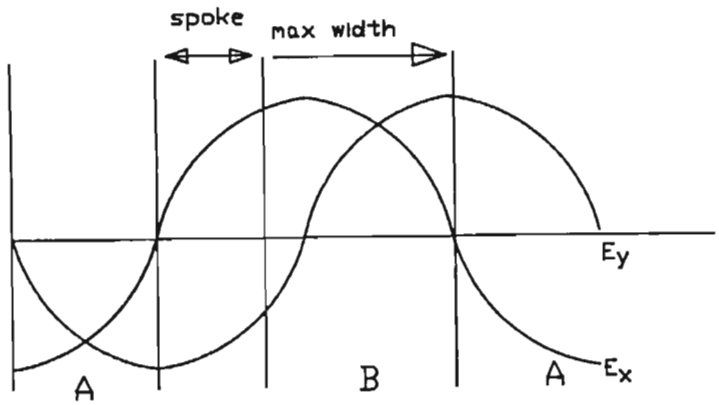

Figure 3.6.1 RF Electric Fields in the Interaction Region

The RF field in the x-direction determines if the swarm is accelerated or decelerated. In the region indicated favourable spoke formation exists and the x-direction field is retarding. In the region marked B the x field is retarding but no spoke is formed since the threshold field is not exceeded. In region A however the x-direction electric field is accelerating and electrons gain energy from the RF field. The total energy lost by the RF field (and thus gained by the electrons at the hub surface) is the difference between the energy gained in region A and that lost in region B. This energy will in general be dissipated in the cathode.

At y = h the x-directed electric field acts on the charge at the surface of the Brillouin hub and will determine the y-directed movement of the charge. In region A E_x is negative and electrons will be returned to the cathode with increased energy while in region B this field is positive and the electrons will move away from the cathode losing energy. To calculate the power loss we calculate the electron velocity in the negative y-direction, the equivalent electron current thus being

$$I_c = E_x \rho L \beta_n / (B\beta) \qquad (3.6.19)$$

The equivalent electron voltage is dependent on the velocity and given

by

$$V_c = mv_y^2/(2e) \qquad (3.6.20)$$

The power loss due to the electron bombardment is thus

$$P_c = E_x \rho L \beta_n \, m(E_x/B)^2/(2B\beta e) \qquad (3.6.21)$$

3.7 Program Implementation

3.7.1 Magnetron Performance Calculation

The set of equations of the preceding sections determine the magnetron performance characteristics. The variable that must be determined by iteration is the RF voltage V_{rf}.

For a given anode voltage, the synchronous voltage may be calculated directly from equation (3.3.7). For an initial estimate of the RF voltage, the spoke phase angle may be determined from equation (3.4.26). This has to be determined iteratively since the spoke phase appears on both sides of the equation. The spoke current may be determined from equation (3.5.1) and multiplied by the number of spokes to obtain the anode current. From equations (3.6.8), (3.6.18) and (3.6.21) the tube losses may be calculated. Equation (3.6.7) gives the output power and thus equation (3.6.1) may be used to test for the correct RF voltage. If the input power does not equal the output power the RF voltage is adjusted and the exercise repeated.

The exact methods used in CAMPA are not given here; they are simple iterative 'try and adjust' methods. The programming problem is trivial as long as a suitable minimum start value is used for the RF voltage in equation (3.4.26).

These equations may therefore be combined to calculate the magnetron performance data. The analysis thus far has been for a linear

magnetron and in certain cases these equations may be applied directly to the cylindrical tube, as long as the curvature effects are small. Often, however, these effects are significant and thus the pertinent equations should be adapted to the cylindrical configuration. This has been done in Appendix D, where the cylindrical equivalent of the various equations have been given. The major difference between the linear and cylindrical model is the width of the spoke base, that in the cylindrical model being substantially smaller than that in the linear case. The equations for the cylindrical model finally implemented in the computer program CAMPA are listed in Appendix D.

3.8 Conclusions

Through the use of the Welch spoke formation criteria a fairly simple analytic magnetron model may be constructed. In this chapter the Welsch criteria has been extended by examining the electric fields at the surface of the Brillouin stream. Space charge effects have been included in determining the spoke phase. In this phase current is drawn from the Brillouin stream. The spoke current is determined from the electric fields at the surface of the hub, and thus the total anode current may be calculated.

This model has several unique features; the threshold condition is based on total fields at the edge of the Brillouin stream; Brillouin hub modulation by RF fields is taken into account and the anode current calculated has only a second order dependence on the spoke shape.

These equations have been adapted for the cylindrical magnetron as shown in Appendix D and written into the program CAMPA. The performance of this model is assessed in Chapter 5.

CHAPTER 4

THE DEVELOPMENT OF A COMPUTER CONTROLLED MAGNETRON LOAD

4.1 Introduction

Normally two sets of tests are conducted during the manufacture of a magnetron. The first, called the 'cold' tests, are used to preset the magnetron wavelength and adjust the system Q. These tests are conducted before the final sealing off of the tube, and are performed at low power levels. Wavelength presetting is conducted by the adjustment of the strapping capacitance while the system Q may be adjusted by altering the output coupling. The second series of tests, called the 'hot' tests, are performed after the tube has been pumped down, baked out, had the cathode activated, and been sealed off. The purpose of the hot tests are to age (stabilize) the tube and to verify the tube performance at rated power. During the aging process the tube is allowed to arc internally under controlled conditions (i.e. allow the arc to clear before reapplying power), which vaporizes any mechanical protrusions and results in a more stable performance. Critical performance indicators include the power output (both average and peak if pulsed), frequency stability, pushing and pulling figures and missing pulse count. During the tests the applied voltage and current waveform and output spectrum would also be noted.

It is critical that the RF load connected to the tube is accurately characterised, since it will affect all of the these measurements. The load must not only present a low VSWR to the tube, but must also allow the variation of the VSWR in order to measure the pulling figure and plot the Rieke diagram. To the manufacturer the pulling figure represents the degree of coupling between the resonator system and the output circuit, normally adjusted during cold tests. For the tube user it represents the frequency deviation as the load VSWR is varied from a perfect match to VSWR=1,5:1. The tighter the coupling, the greater the pulling figure, but the higher the tube efficiency and the lower the internal RF voltage. If the pulling figure is too low, internal tube arcing[58] and multipactor[59] could occur, leading to a higher missing pulse count and possible tube damage.

The Rieke diagram is a useful performance chart which may be used to determine the pulling figure. This chart plots lines of constant frequency and constant power as the load VSWR is varied on the Smith Chart. Plotting this chart by hand is a tedious process, since both the magnitude and phase of the load reflection coefficient must be changed and the power and frequency measured. This process is repeated for every data point before the lines of constant power and frequency may be constructed.

The need therefore arose to design and construct a computer controlled magnetron load that could have an accurately determined reflection coefficient. The circuit had to have the ability to absorb full output power, provide a variable mismatch from VSWR = 1:1 to VSWR = 1,5:1 and alter the phase of the mismatch from 0 to 360^{o}. This last specification is the industrial standard used to determine the tube pulling figure. This would allow the load to be incorporated into a computer system to automatically generate Rieke diagrams and calculate pulling figures.

The circuit subsequently designed and built operates in the S-Band over the 2.7 - 3.0 GHz frequency range and is capable of handling powers of up to 1 MW peak and up to 1 kW average. It allows the operator to vary the magnitude and phase of the reflection coefficient within the VSWR = 1,5:1 circle or to move along any predefined path within that circle.

This chapter discusses the high power load in detail with emphasis on the development of the tuner section and its integration into the system. Section 4.2 examines a commonly used load design and discusses its limitations. Triple stub tuners are discussed, and Section 4.3 examines the problem of predicting the performance of the tuner. Initially it is assumed that the tuner section elements are ideal, and that the load controller has some means of adjusting the individual elements directly. Section 4.4 examines the design of the tuner elements is some detail introducing a novel metal-loaded-dielectric stub. Section 4.5 examines the accuracy of the modelling. Section 4.6 discusses the design of the termination, and a new water load configuration that is simple to construct yet gives good matching characteristics is introduced. Finally Section 4.7 discusses the

problem of implementing the circuit, and gives the low power test results. System limitations and some additional applications are discussed in the concluding paragraph.

4.2 Design Alternatives

4.2.1 Conventional Designs

It is usual to regard the output circuit as three separate entities viz. a perfect load, a variable mismatch and a phase changer. These three entities may essentially be designed separately and then integrated into a single waveguide system. At powers above 1 kW the load would tend to be water cooled. The mismatch would typically be a dielectric stub inserted into the guide by a motor driven linkage, while the phase changer would be a dielectric wedge or transformer section that may be moved from the edge of the waveguide wall to the centre, again by mechanical linkages. A typical configuration is shown in Figure 4.2.1.

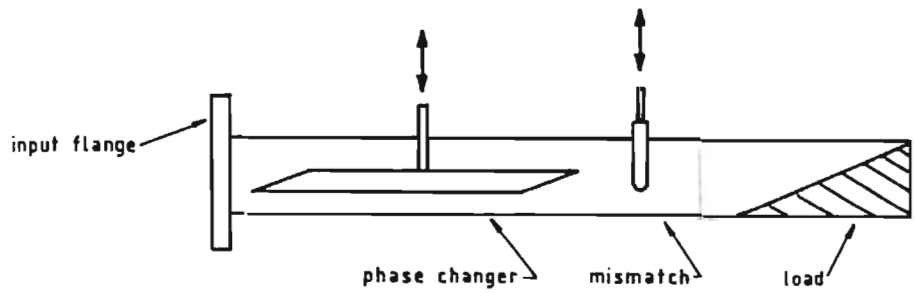

FIG.4.2.1 : A Common Circuit Configuration

This system has been widely adopted by the tube industry, but has a number of serious disadvantages : (a) the phase changer will alter the mismatch[60,61], (b) due to its length, the mechanical stability of the phase changer is poor and (c) a very precise load is required. Even if these conditions were met, the VSWR with the mismatch stub

withdrawn would be limited by the reflection due to the holes in the waveguide walls, the phase changer and the load (typically in the range 1,15-1,20:1). In addition, the phase of the reflection coefficient is not easily determined from the position of the phase changer, and the complete unit can become excessively long (up to 2m for S-band). Not knowing the load phase and not being able to obtain a good match means that the load cannot be used directly to construct Rieke diagrams and thus does not lend itself to the type of versatility that would be necessary when conducting aging tests.

4.2.2 Triple Stub Tuners

The triple stub tuner shown diagramatically in figure 4.2.2 has the potential to produce a mismatch of any magnitude and phase[62]. However, this requires the individual tuning elements to have a range of reactance from very large negative values (capacitive) to very large positive values (inductive). This is a difficult requirement in practice; and depending on the configuration, a limited range of mismatch is normally obtained .

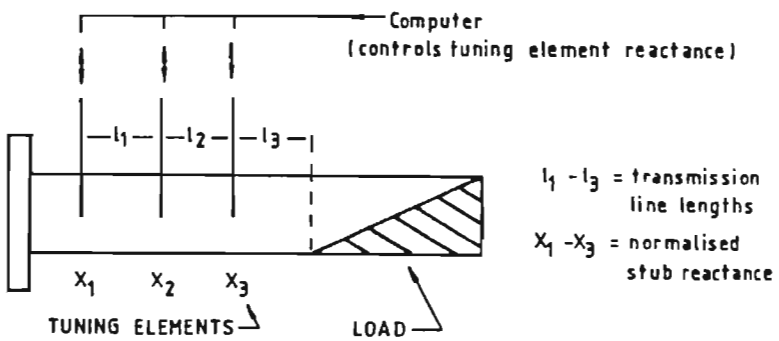

FIG.4.2.2 : Generalised Triple Stub Tuner Configuration

Here l_1 and l_2 are the lengths of transmission line between the tuning elements, X_1 to X_3 represent the normalised reactance of each tuning element number 1 to 3 and l_3 is the length of transmission line between stub 3 and the load. The computer must be able to adjust

the reactance of each tuning element. If these stubs are dielectric inserted stubs, stepper motors may be used to drive the stubs to positions determined by the computer. At all times the controller must know what reflection coefficient the magnetron sees, and thus the reflection coefficient may be adjusted to any value (magnitude and phase) within the VSWR=1,5:1 circle.

Short tuning elements must be used to increase mechanical stability and the unit should be physically short. Since it is possible to move to any position within the VSWR circle, the effects of waveguide holes and imperfect loads could be eliminated by appropriately positioning the stubs. With computer control, Rieke diagrams can then be automatically plotted and the aging process optimised by adjusting the mismatch and phase to a value resulting in a maximum missing pulse count. Arcing would be limited by repositioning the stubs to a match when necessary.

Such a system would remove all the objections raised against the conventional design. The purpose of the initial study was to investigate the performance of this configuration assuming a limited range of tuner reactance. The best method of determining the load reflection coefficient from the mechanical positions of the tuner elements could then be determined.

4.3 Triple Stub Performance Prediction

Any stub inserted into a waveguide represents an extremely complex 3-dimensional disturbance to the dominant TE mode electric field, generating higher order modes with non-zero x, y and z electric field components. Unless considerable mathematical simplifications are made, this prohibits a simple solution - and computer-aided numerical techniques would generally have to be employed [63].

However, for the purposes of the initial design it suffices to assume only that the disturbance is lossless - or near lossless. Thus, in terms of the equivalent circuit, a simple shunt susceptance may be assigned to the disturbance - provided a suitable measurement

reference plane is chosen. This reference may need to vary with frequency, and in the final implementation this would need to be taken into account by the computer controller. The model used to predict the 3-stub tuner performance is shown in Figure 4.3.1.

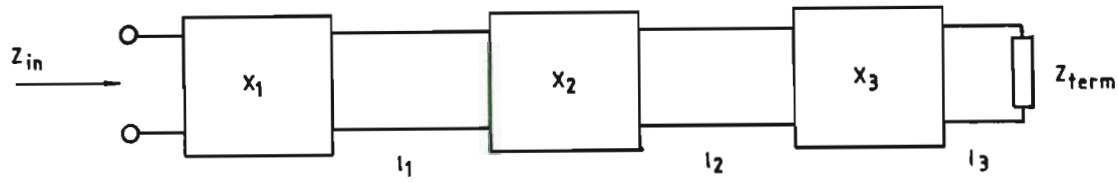

FIG.4.3.1 : Triple Stub Tuner Model

Three lossless mismatch stubs 1,2,3 with respective normalised reactance X_1, X_2, X_3 are interconnected with lengths of lossless transmission line l_1, and l_2, while stub 3 is connected to a terminating load Z by a length of line l_3. This termination may not be a perfect match to the length of line l_3, and will in general have a finite mismatch. For convenience, the measurement reference plane is chosen at the input terminals of X_1.

4.3.1 Computer Solutions

The transmission line representation of each of the circuit component parts follows the usual format[62] . The resulting equations however are rather tedious to solve by hand, and a computer program was therefore written which produced a graphics output showing the effect that stub size, stub position, distance between stubs, termination and frequency have on the reflection coefficient . This program has a second use in that it allows the user to specify the operating frequency and termination - then by a series of iterations gives the distances between the stubs and the required reactance of the stubs,

in order to achieve the maximum coverage of the Smith Chart.

In order to illustrate the type of output obtained, the reflection coefficient polar plot locii are shown in Figure 4.3.2 at an operating frequency of 2,8GHz.

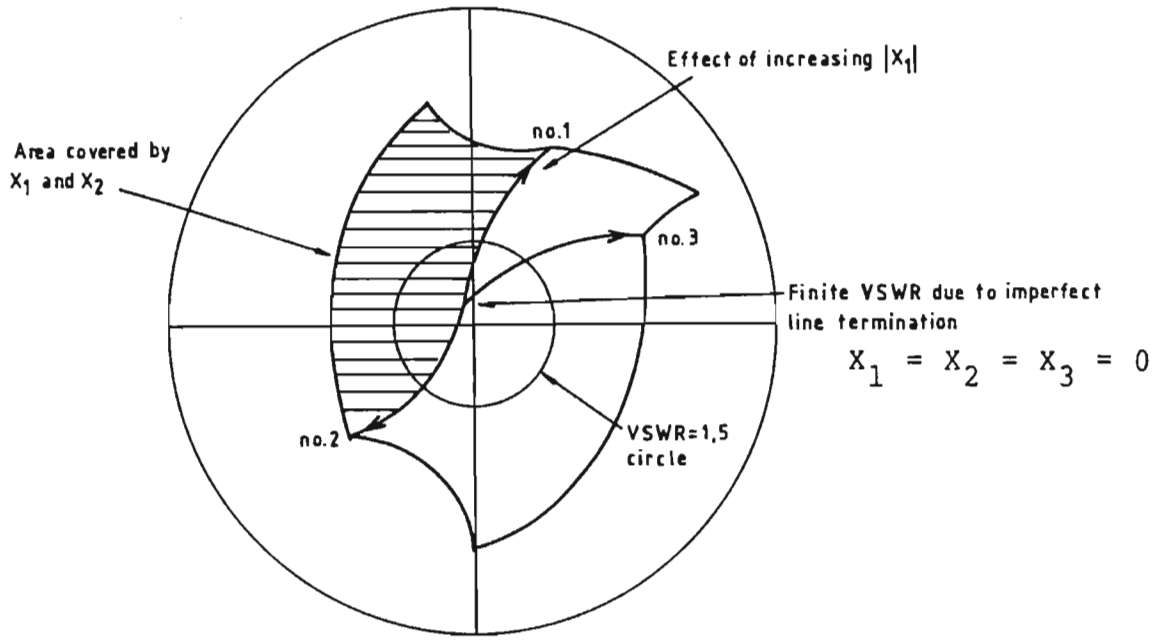

FIG.4.3.2 : Reflection Coefficient Variation with Stub Position

For example, if all stub reactances were reduced to zero, a finite mismatch would exist due to the imperfect termination (see the point $X_1 = X_2 = X_3 = 0$ in Figure 4.3.2). The three lines radiating from this point represent the reflection coefficient locii as a result of increasing one reactance only. Thus, as $|X_1|$ is increased, the reflection would increase along the path as shown. If $|X_2|$ is now increased, the reflection would change, and move into the shaded area shown. Since the objective is to cover the VSWR = 1,5:1 circle, the area within the circle must be covered by a combination of stub positions. The variation of stub reactance thus describes a path that depends on the position of the other two stubs. To avoid complex paths

which could run into 'dead-ends' and result in excessively complex controlling programs, only two stubs are allowed to have a non-zero reactance at any one time. The locii shape follows the expected shape for a pure reactance.

4.3.2 Optimised Output for a 2,6-3,0 GHz Tuner

The designer has essentially two circuit parameters under his control. The first is the stub separation, and the second is the maximum reactance of a stub. An optimum design would therefore be one that gave maximum coverage for minimum stub reactance. Three reflection coefficient plots are shown in Figure 4.3.3 at 2,6; 2,8 and 3,0GHz respectively. The optimum circuit parameters here are: 1) equal separation between stubs (44mm) 2) perfect termination 3) $|X_1| = |X_2| = |X_3| = 0,9$

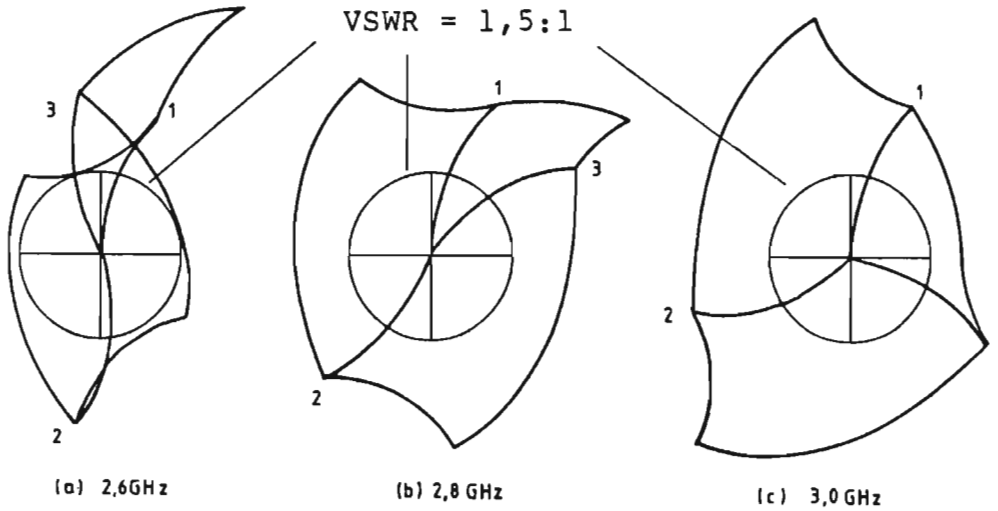

FIG.4.3.3 : Reflection Coefficient Variation at Lower and Upper Frequency Limits

Again, points labeled 1,2 and 3 in figure 4.3.3 represent the maximum individual stub movements of stubs no.1, 2, and 3

respectively, and the area enclosed is the maximum coverage at the specified frequency. The centre circle represents the VSWR = 1,5:1 locus. As the frequency changes, the phase between the three stub locii will change as shown. At both frequencies the circle is covered by a combination of any two stubs. A point of note is that the stub separation is not the recommended 3/8 (centre-frequency wavelength) [61], but is approximately 3/10 (centre frequency wavelength). In fact, using the recommended spacing does not give the desired coverage of the VSWR = 1,5:1 circle. The first and third stub would be 3/4 wavelength apart, and the combined effect of these two stubs does not give any additional coverage of the VSWR = 1,5:1 circle, but leaves a large section of the circle uncovered. This is a direct consequence of having limited the individual stub reactances.

Figure 4.3.4 shows two additional reflection coefficient plots. The first is calculated as before at 2,6GHz with a 44mm stub separation, but with smaller stubs. The second is calculated at 3,0GHz using an unchanged stub size but with the stub separation increased to 45mm.

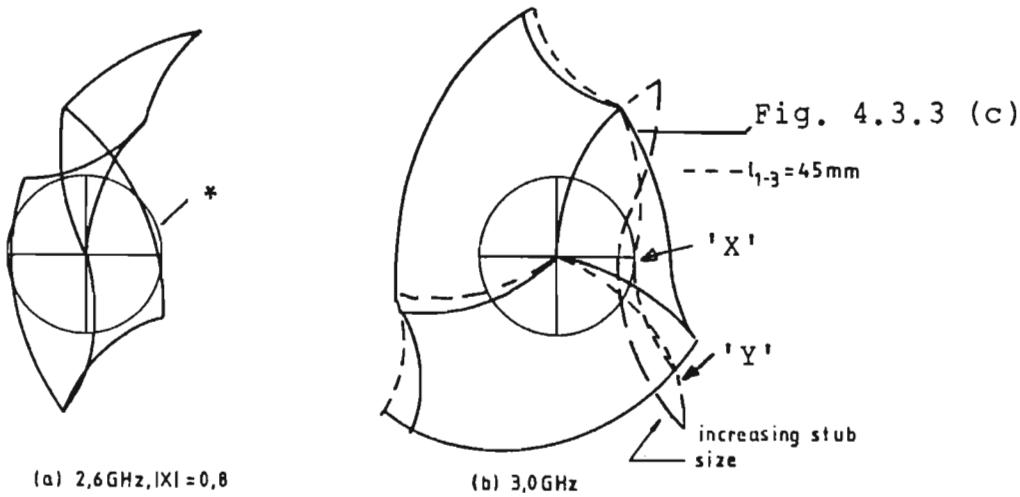

FIG.4.3.4 : The Effect of Changing Stub Size and Stub Position at 2,6 and 3,0 GHz Respectively

In Figure 4.3.4(a) reducing the stub size from |X| = 0,9 to |X| = 0,8 has resulted in part of the VSWR = 1,5:1 circle not being covered (see area marked *). In Figure 4.3.4(b) on the other hand, increasing stub separation by 1mm results in a locii which just covers the VSWR = 1,5:1 circle, but any further increase in separation will result in part of the circle being exposed (see area marked x). Increasing the stub size does not improve matters since it merely results in a 'folding back' of area covered (see area marked y).

Two conclusions may be drawn:

1) the high frequency plot is more sensitive to stub position and less to stub size

2) the low frequency plot is more sensitive to stub size and less to stub position

The upper operating frequency therefore largely determines the stub separation, while the lower end of the operating bandwidth depends largely on the stub size. Increasing stub size does not continuously increase the bandwidth; it is clear that operation will again be limited below 2,6GHz in a manner similar to the limitations at 3,0GHz.

This therefore illustrates the inherent limitations of a fixed position 3-stub tuner which has only a limited range of tuner element reactance - the operating bandwidth could, however, be extended by use of four or more tuning elements.

4.3.4 Incorporation of a non-perfect Termination

The use of the 3-stub tuner is further enhanced by its ability to 'tune-out' any imperfections in the termination. To design a load with a VSWR better than 1:1,08 is fairly straight forward[64]. This corresponds to a reflection coefficient of 0,04; and incorporating this into the circuit produces a shift of the locus diagrams (see for example Figure 4.3.2). The amount of shift allowed is clearly dependant upon the performance at the extreme ends of the operating

band. The termination must therefore be designed bearing in mind the limitations imposed by the finite reactance achievable with a real stub.

4.4 Mismatch Stub Design

Power handling requirements determine the use of hollow rectangular waveguide; use was made of standard 2,65-4,05 GHz brass rectangular guide. There are a vast number of alternative methods that can be used to produce a lossless mismatch in a rectangular guide[65]. Mechanical stability and power requirements reduce the alternatives, and the best solution is the introduction of a lossless dielectric into the guide; the quantity and position within the guide determining the reactance. Again, the number of alternatives as to the shape of the dielectric are endless; however, a circular cross-section rod provides the best volume:cross-sectional area ratio thus reducing the overall length of the tuning stub.

4.4.1 Choice of Stub Configuration

The dielectric may be inserted parallel or perpendicular to the direction of the $\bar{E}$ field of the dominant TE mode. Figure 4.4.1 shows the two orientations that are possible.

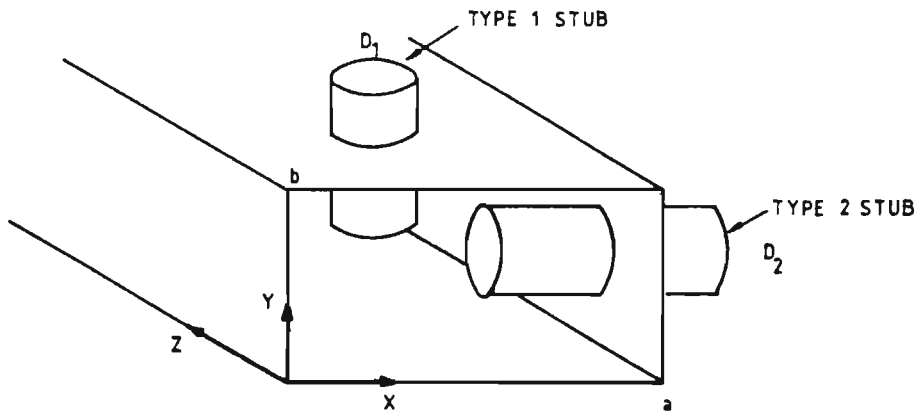

FIG.4.4.1 : Rectangular Guide Cross-Section

The magnitude of the resultant stub reactance $|X|$ is proportional to the volume integral of the dominant mode $\bar{E}$ field squared[66].

Thus $|X| \propto \int |E|^2 \, dV$; V denotes the dielectric volume. (1)

For the dominant mode $\bar{E}$ is a function of x, and

$$|E| = E_o \sin(\pi x/a) \tag{2}$$

$$\text{so } |X| \propto A \int_0^1 E_o^2 \sin^2(\pi x/a) dx \tag{3}$$

where A = stub cross-sectional area,
l = length of stub.

Moreover, since RF arcing is most likely to occur in the airgap, a measure of the peak power handling capabilities of the guide is the length of this gap at the centre of the guide. Hence, presuming equal peak powers and stub reactance for both configurations shown in Figure 4.4.1 above, a simple relationship between the stub diameters may be found:

$$D_1 = \sqrt{aD_2/2} \tag{4}$$

Thus, if $D_2 = b/4 = a/8$ then $D_1 = 0{,}25a$ or $D_1/D_2 = 2$

This simple analysis serves to illustrate the difference in diameters between a type 1 and a type 2 stub: the D_1/D_2 ratio would be further increased if the ends of the stubs are fully radiused.

A type 2 stub therefore has an advantage over a type 1 stub. Longer travel makes precise tuning easier (smaller reactance change for the same mechanical movement) while the smaller diameter reduces stub/guide pressure sealing problems. Lower pressure due to reduced areas and smaller stub circumference results in lower mechanical torques required, and subsequently smaller driving motors.

4.4.2 Stub Construction

Results from initial simulations indicated that each single stub should have a normalised reactance of approximately $|X| = 1,0$. Initial tests conducted using Nylon stubs showed that a 18mm diameter rod would be suitable. However, Nylon retains water and the resultant high microwave loss makes it an unsuitable high power stub. Since, to the first order, the magnitude of the reflection coefficient is proportional to the product of dielectric volume and dielectric constant, an equivalent PTFE stub would have to have a diameter of 25mm, since its dielectric constant is approximately half that of Nylon. This leaves only a small air gap between the waveguide wall and the dielectric - reducing peak power capabilities of the circuit. One method of increasing the reactance is to choose a material with a higher dielectric constant; for example Dystrene or Aluminium Oxide. The disadvantage of using these materials is reduced availability and higher tooling costs.

An alternative method of increasing the stub reactance but decreasing the stub diameter is to increase the electrical stress in the dielectric by insertion of a metal rod into the dielectric material. In this particular design, an 18mm PTFE stub loaded with a 10mm brass rod was found to give the required results. The brass rod is fully radiused and machined slightly larger to provide an interference fit. After degreasing to remove machining oils, the stub is assembled under vacuum, to prevent the formation of trapped air pockets.The final construction detail is shown in Figure 4.4.2. Power loss through the dielectric at the waveguide hole was assessed using an HP8510 Network analyser. A single stub was inserted into a length of guide and the S-parameters measured. Results showed that the power loss was negligible.

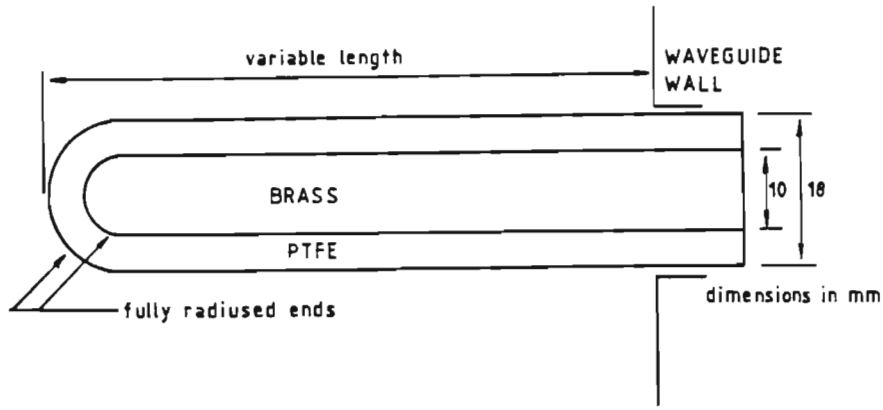

FIG.4.4.2 : Stub Construction Detail

4.5 Accuracy of the Models

In order to assess the accuracy of the models, a number of tests were carried out using Nylon stubs. All measurements were made using an HP8510 Network Analyser. The analyser was calibrated for the waveguide using two offset shorts and a fixed waveguide load with a VSWR better than 1.01:1. As a comparison, an alternative low power reference was constructed from a 1,5m tapered timber wedge. The calibrated analyser returned a VSWR of 1,01:1 for this wedge, providing confidence in the measurements. Initial tests were designed to characterise a single stub in order to compare it to the initially assumed ideal lossless reactance. This was done by inserting a 15mm stub into a short section of guide and measuring the resulting S-parameters. Using this data obtained, a program was written which used this tabulated data to predict the performance of the 3-stub tuner. A comparison could thus be made between predictions of the triple stub tuner performance using the simple shunt capacitor model and the performance predicted from data obtained from 2-port characterisation of a single stub. Results were evaluated at a fixed frequency for varying stub size and at variable frequency for fixed stub size.

Figure 4.5.1 shows a comparison of results obtained at 3.0 GHz.

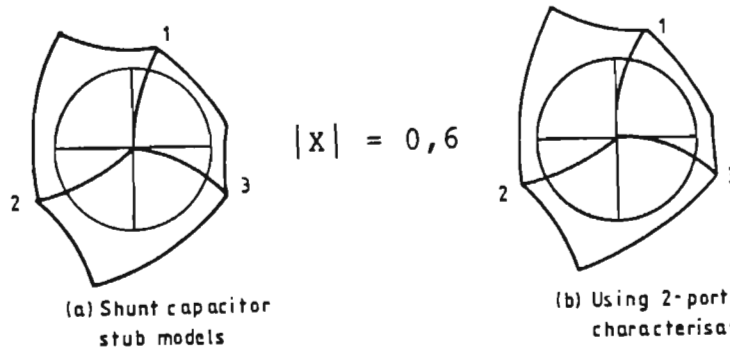

(a) shunt capacitor stub models (b) 2-port stub characterisation

FIG.4.5.1 : Performance Prediction Comparison at 3GHz

Figure 4.5.2 shows a comparison of performance at a fixed stub position as the frequency is varied from 2.6 to 3.0 GHz. Data points denoted by 'X' represent predictions using 2 port characterisations.

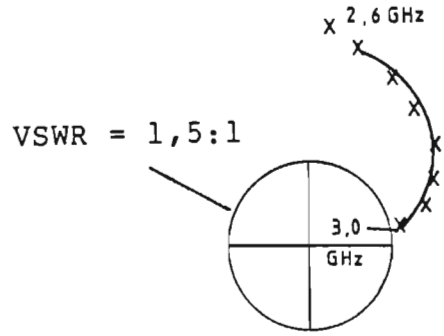

shunt capacitor stub models ; X - 2-port stub characterisation

FIG.4.5.2 : Performance Prediction Comparison
Frequency Range 2,6 - 3,0GHz

Performance prediction is clearly in close agreement when a single frequency is considered, as in Figure 4.5.1. The agreement in Figure 4.5.2, however is not as good, showing in this example a significant difference at 2.6 GHz. This illustrates the limitations of using single lumped elements to model the stubs whose diameters are a

significant fraction of the guide wavelength.

Figure 4.5.3 compares the performance predicted, using the simple theoretical model, to measured results obtained from a prototype 3 stub tuner.

Again, at a fixed frequency good agreement is obtained.

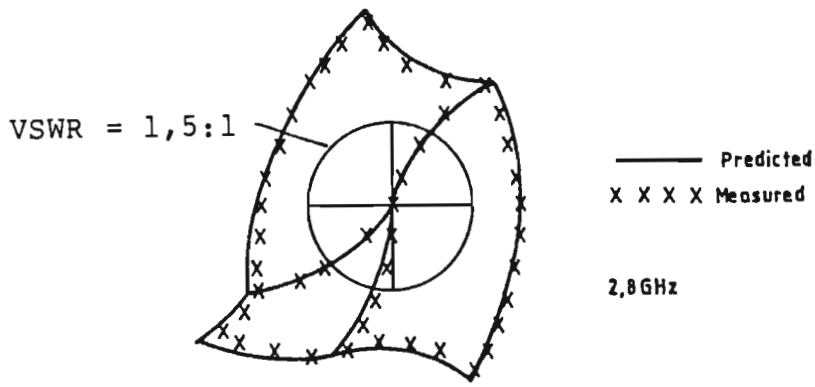

FIG.4.5.3 : Comparison between Measured and Predicted Performance at 2,8GHz using the Shunt Capacitor Model

4.6 Termination Design and Construction

4.6.1 Termination Requirements

The constraint thus far imposed on the termination is that in order to keep to a reasonable stub diameter and still have good band coverage the VSWR of the termination must be better than 1,08:1. An additional requirement of a magnetron test load is to measure the output power and spectrum. At power levels in excess of 100 kW it is best to measure power by means of a calorimetric load. Accuracies around 5% can be obtained using a calorimetric load compared to an error in the order of 2dB in 50dB or 40% if a calibrated coupling system is used. The output frequency may be measured by sampling the power through a

suitable waveguide coupling.

The termination requirements can thus be summarised as follows :

Type : Calorimetric water load
Frequency : 2,6-3,0 GHz
Match : Maximum VSWR over operating band 1,08:1
Stability : 1%
RF pickoff : -50dB

There are a number of differing load configurations possible that would satisfy these requirements[64]. Since the constraint on the VSWR is not exceedingly tight, and since it is desirable to simplify construction as much as possible, only designs that employ relatively simple waveguide designs have been investigated. All configurations will have the same fundamental considerations viz. 1) a gradual introduction of the lossy medium, 2) sufficient loss to reduce the power reflected off the guide short circuit at the end of the load, 3) sufficient thermal insulation to provide accurate power measurement and 4) ease of construction. The design has for convenience has been divided up into three areas : loss introduction, loss section and loss termination.

4.6.2 Introducing the Loss

To reduce the overall VSWR the loss must be introduced into an area of low electric field intensity over a sufficient number of wavelengths. The lossy medium (water in this case) must be contained in a suitably thermally insulating but microwave-transparent envelope. Pyrex glass was used in this instance; it is inexpensive, and may be worked into virtually any shape. Two methods of introducing the loss are discussed here; the first has been termed the 'Hole-in-Waveguide' (HIW); the second the 'Hairpin-Bend'(HPB) method. The latter is a novel approach to loss introduction.

4.6.3 Amount of Lossy Material Required

Tests conducted on S-Band waveguide have shown that over a 150 mm length a 30 mm diameter tube of water provides a loss of approximately 30dB (about 2dB/cm). A total loss of at least 30dB is required if the load is to be within specification. Thus, depending on the size of the water tube the length may have to be increased or decreased.

4.6.4 Load Termination

To prevent any hazardous radiation from the load the end of the guide must be terminated with a short circuit. Any reflection at this point must therefore be sufficiently low to reduce the overall VSWR.

4.6.5 The HIW Load

Figure 4.6.1 is a conceptual diagram of the HIW system showing the major reflections expected. The water is introduced into the narrow side of the waveguide through a hole in the waveguide. Incident wave reflection will be as a result of the disruption of the sidewall currents as well as the introduction of the Pyrex/water tube into the guide. The tube is tapered in diameter to gradually increase the loss and angled to move towards the centre in the guide where the RF electric field strength is greatest.

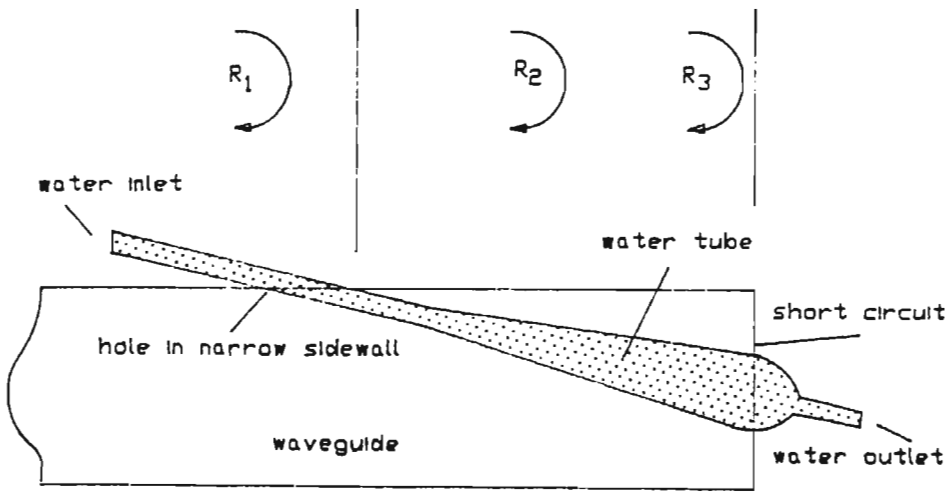

Fig. 4.6.1 Hole-in-Waveguide introduction of the lossy medium

Experiments conducted on S-Band waveguide show that the reflection due to a 10mm hole in the narrow wall of the guide gives a VSWR of 1,07:1.

To design a load to the required specification reflections R_2 and R_3 must be made insignificant. Fortunately this is possible by using sufficiently narrow tapers and long loss sections.

The advantages of a HIW system are :

1) The glass construction is simple and construction therefore repeatable

2)The reflected wave R_2 can be made as small as desired by using a very narrow taper.

3) The reflected wave R_3 can be made as small as desired by using a long loss section

The disadvantages are :

1) A more complex waveguide construction is required
2) The hole in the guide sidewall resulting in the reflected wave R_1 is the main reflection component and cannot easily be reduced.

4.6.6 The HPB Load

Water is introduced into the guide by a series of thin-walled Pyrex tubes. Figure 4.6.2 shows the arrangement of the tubes. The leading edges of the tubes are staggered to form a 1/4 wave transformer to reduce the reflection and the tubes are extended to the rear of the load (to the short circuit) and cross-coupled to balance the water heating effects. Figure 4.6.3 shows the major reflections expected from this load. There is no hole in the guide so that reflected wave R_1 is cancelled by R_2. A taper section (if used) and a loss section make up the complete load.

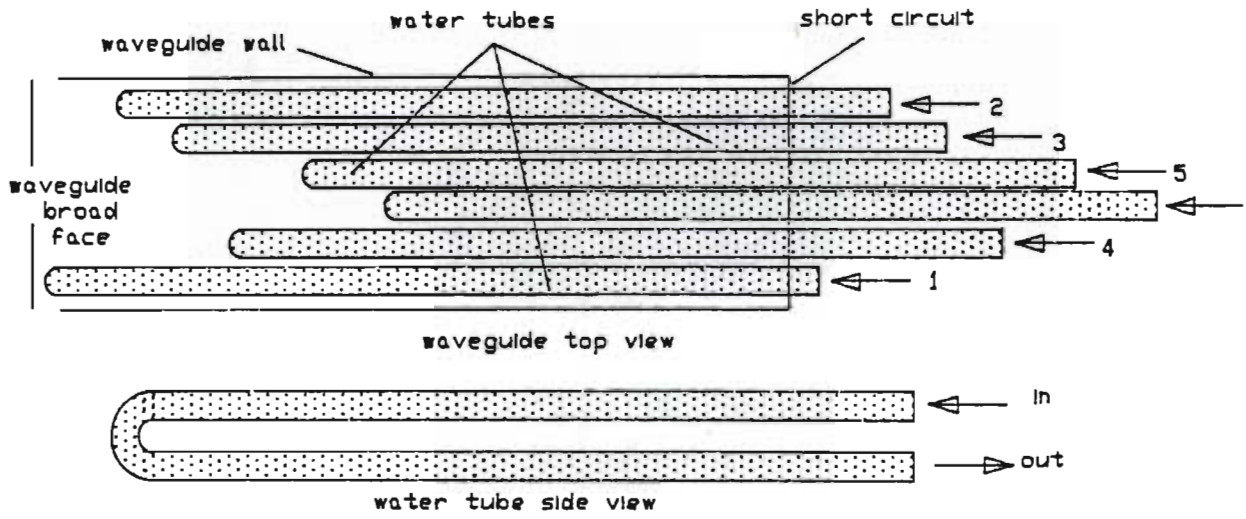

Fig. 4.6.2 The Hairpin-Bend Load

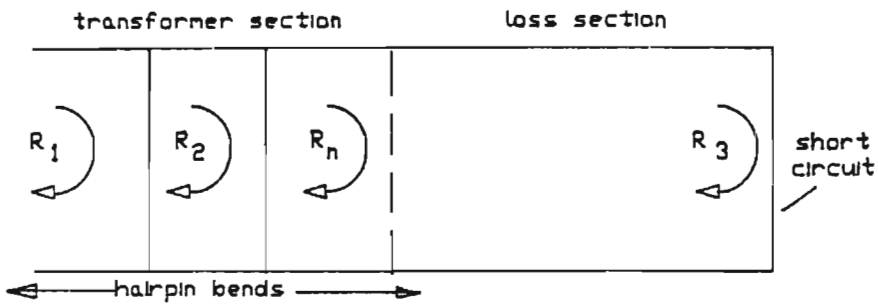

Fig. 4.6.3 Reflections in the HPB Load

Figure 4.6.4 shows the measured VSWR for both a single 4mm diameter hairpin and a pair of hairpin bends spaced 1/4 wavelength apart. The maximum VSWR for the single hairpin is 1,044:1 while the maximum VSWR for the dual hairpins is 1,020:1. In both cases measurements were made using a standard low power load to terminate the waveguide.

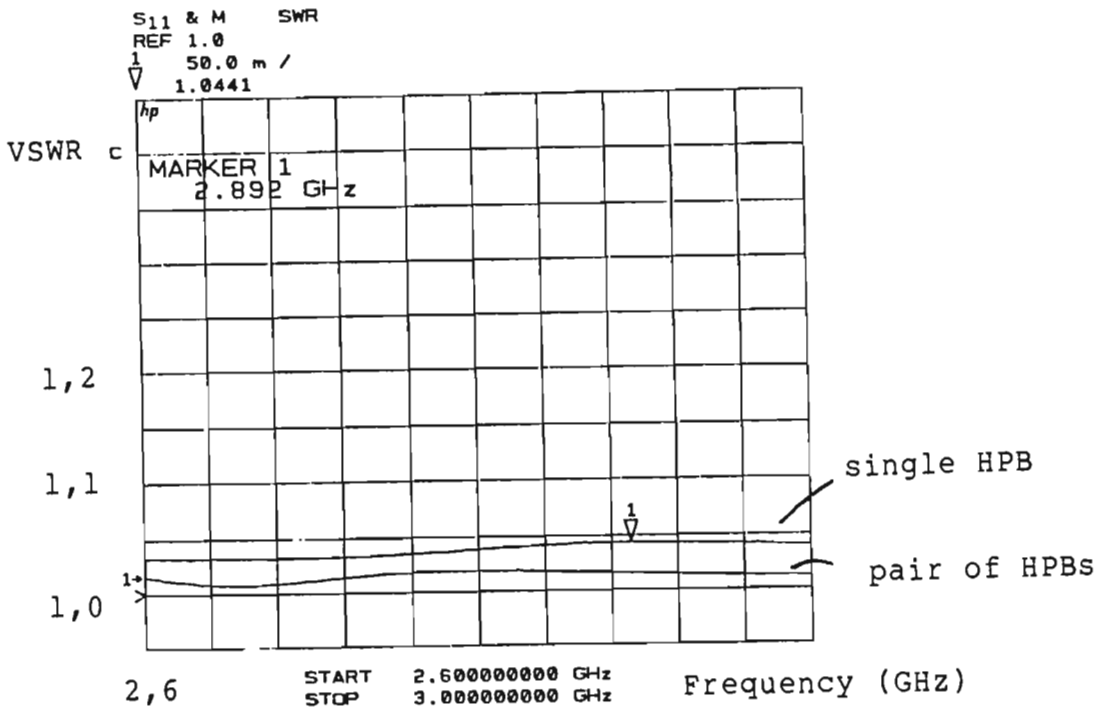

Fig. 4.6.4 VSWR for a Single Hairpin and a Pair of 1/4 wavelength Spaced Hairpins using 4mm diameter Pyrex Tube

Hairpins are staggered as shown in Figure 4.6.2 to optimise the VSWR across the band. Experiments were conducted using two pairs of 1/4-wavelength spaced hairpins constructed from 11mm diameter Pyrex tube to achieve a VSWR of better than 1,04:1. The overall length of the load is 500mm.

The advantages of the HPB construction are :

1) Simple waveguide construction. The waveguide is standard and unmodified. The tube assembly is inserted from the short circuit end.

2) Lower overall VSWR

The disadvantages are :

1) More complex glass construction.

2) The main reflection is due to the hairpins. This means that the construction of the bends must be standardised to ensure that the RF characteristics are repeatable.

3) The overall construction is twice as long as the HIW design

4) Greater thermal loss than the HIW design due to the greater surface area to water volume ratio.

4.6.7 Considerations when Integrating the Load and Tuner

The one advantage of the Triple Stub Tuner is its ability to eliminate the effects due to imperfect loads. This implies that the load characteristics must not alter with time (both in magnitude and phase) otherwise the calibration will become invalid. In this respect the HIW design will be more stable since its RF characteristics are determined largely by the sidewall hole. The RF characteristics of the HPB design are however determined by the hairpins themselves; both the Pyrex tube construction (wall thickness, bend shape) and the water (purity, temperature). In this case the HIW is the better system choice even though the VSWR of the load on its own is higher. The other significant advantage in this particular application is the reduced length of the load.

4.7 Circuit Implementation and Measured Performance

4.7.1 The Triple Stub Tuner

The circuit controller in use is a HP9816 16-bit desktop computer with graphics capabilities. The stubs are stepper-motor driven via zero-backlash gears, and include opto-sensors to detect the mechanical datum. Appendix F details the system operation. System pressure sealing is achieved through the use of 'O' ring seals. The system may be pressurised using either dry nitrogen or preferably SF_6 [67], since

the latter calls for lower waveguide pressures. The stepper controller used allowed the movement of only one motor at a time, which reduced the speed at which the mismatch could be changed. Computer control of the motors is via GPIB and is interrupt driven to allow the controller to calculate the stub movements in advance and to perform 'housekeeping' operations such as checking motor status while the motors move to their new position.

The calibration procedure is simple. The stubs are set up to a pre-determined position, and S_{11} measured by the HP8510. The process is repeated for other stub positions until a complete calibration table is set up. The controlling program then uses this table to determine the required stub positions for a particular reflection coefficient. This calibration table will represent the mapping of a stub position function onto the Smith Chart, and movement of the stubs 1; 2 or 3 will generate a set of intersecting curves. A particular position of stubs will correspond to only one position on the Smith Chart at a fixed frequency, but a particular point on the Smith Chart may correspond to a number of points on the stub position function. It is important to ensure that where possible the calibration represents a one-to-one mapping. This is achieved by allowing only two stubs to assume non-zero positions at any one time. The only problem may then occur at the low frequency end of the operating band. A 'Path-finder' routine with look-ahead buffering allows the continious variation of reflection coefficient along a set path. The proposed path is divided up into segments and the movement between points takes the form of a straight line. At any point the controller thus needs to determine the movement required by the stubs to reach that position. The additional complication was that only one motor could be moved at a time. Movement along the 'straight line' thus took the form of a zig-zag approximation illustrated in Figure 4.7.1

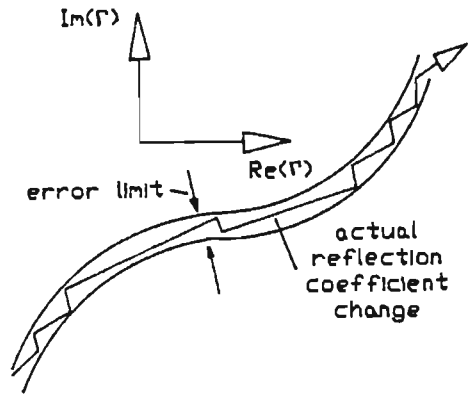

Fig. 4.7.1 A Typical Pathfinder Path

At each point the controller must check that the deviation from the set path was not outside user defined limits.

Figure 4.7.2 shows a measured plot of the reflection coefficient as the phase is varied through 360^{o} at VSWR = 1,5:1. The plot indicates good tracking ability around the prescribed path. The accuracy of the track can be reduced with a subsequent increase in the speed of the phase rotation.

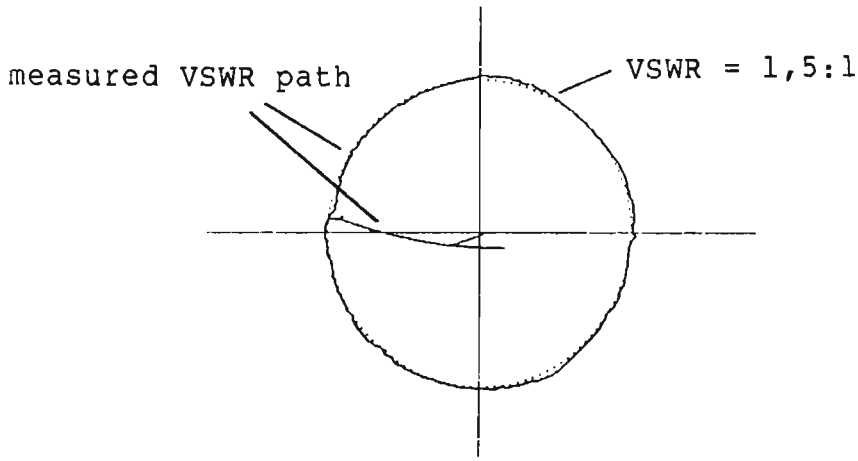

FIG.4.7.2 : Polar Plot of the Measured Reflection Coefficient Phase Change

4.7.2 The Water Load

The Pyrex tube is supported by two thermally insulated supports at either end. Viton 'O' rings are used to provide the necessary water and gas seals.

Figure 4.7.3 shows how the 3 stub circuit may be used to obtain a very accurate match at a specific frequency. Typically the VSWR at the frequency of interest is in the order of 1,02:1. This is considerably better than that achieved by most power water loads.

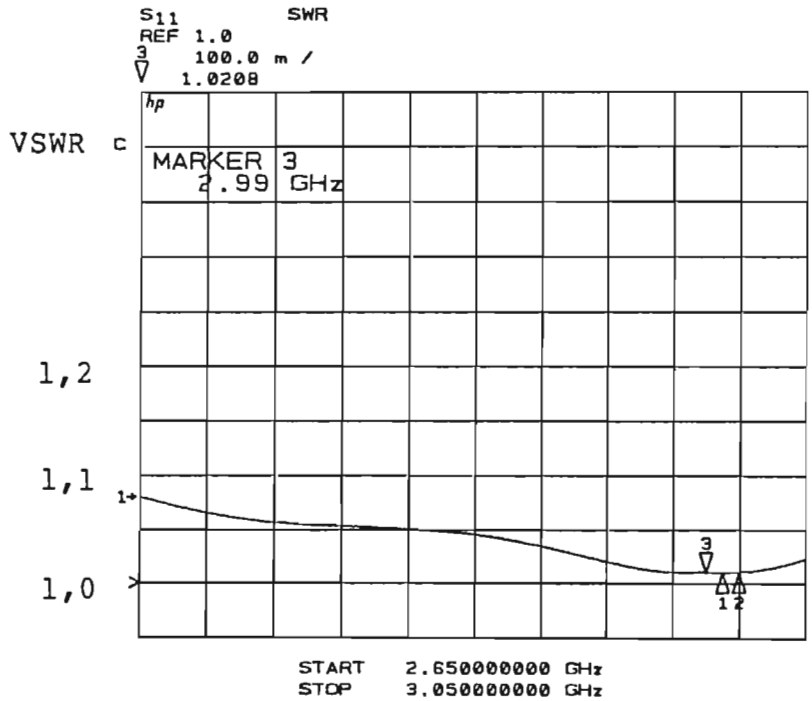

FIG.4.7.3 : Match obtained at 3,0GHz

4.7.3 The RF Pick-off

The probe used is a coaxial E-field type using SMA (7mm) connectors. The probe is designed to give a coupling factor of approximately - 50dB[68].

4.7.4 High Power Tests

The unit was pressurised with SF_6 to reduce the internal pressures, but has been run satisfactorily using dry nitrogen at a pressure of

1,5 bar. The lower pressures required by SF_6 allow the stepper motors to be driven at higher speeds. The unit has at the time of writing been satisfactorily tested at powers up to 850 KW peak and 700W continuous. Tests conducted on an S-Band pulsed magnetron are presented in Chapter 5.

Figure 4.7.4 shows the plan and side view of the completed design.

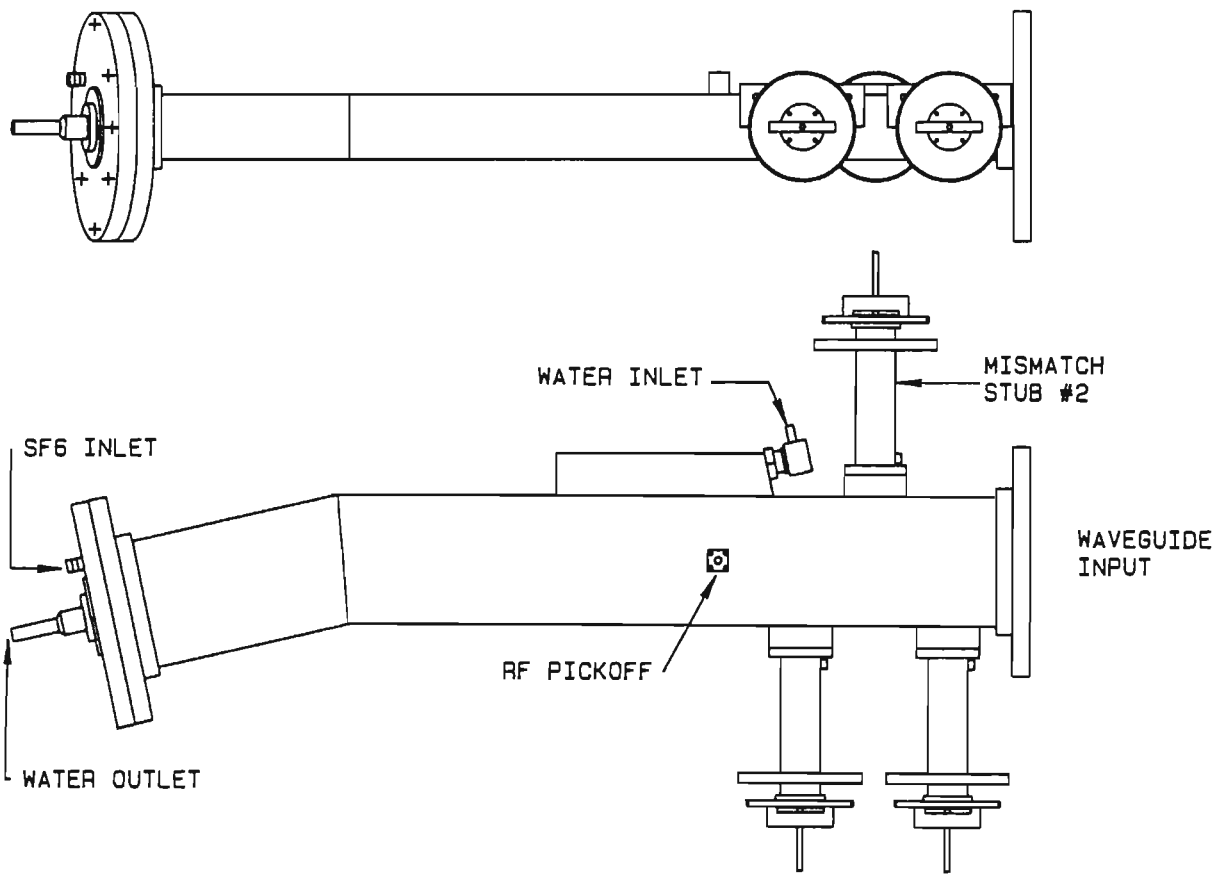

Fig.4.7.4 : Plan and side view of the completed Load

A view of the load installed in the modulator bay is shown in Plate 4.1. This may be compared to the original load shown in Plate 4.2, a design based on the block diagram of Figure 4.2.1.

Plate 4.1 Triple Stub Tuner installed in the modulator cabinet

Plate 4.2 The original magnetron test load. Note the increased length

4.8 Conclusion

Through the use of modern computer based test eguipment and controllers, a high power microwave mismatch unit has been developed and built with a performance that cannot be matched by conventional designs. By employing computer aided analysis the solution is simple, and the employment of exact field solutions, or more complex models, are found to be unneccesary. This technique is well suited to the microwave engineer, who often has to be satisfied with conventional, well proven but at times inferior solutions to his design problems.

At the selected frequency the resulting VSWR of the load is less than 1,02:1, considerably lower than standard designs. Though the concept of using a mechanically driven stub system to match a waveguide system is not new, past systems have not been versatile enough to be of practical use. This control system is simple enough to be incorporated on a single board microprocessor system. This computer controller allows the selected frequency to be altered dynamically, thus the load may be used in an environment where a constantly changing mismatch (e.g. rotating antenna) needs to be tuned out. In this case the VSWR would need to be moved rapidly; this may be achieved through the use of pneumatically operated stubs.

CHAPTER 5

MEASUREMENTS AND SIMULATION RESULTS

5.1 Introduction

This chapter has been divided into two; the first deals with the tests conducted on the Triple Stub Tuner UNMS01 while the second compares the results of simulation runs from the Computer Aided Performance Analysis program CAMPA to measured tube performance curves.

Section 5.2 is essentially a condensation of a report by the author[69] on tests conducted at the CSIR in 1986. Some comments are made on the results obtained from tests conducted on two CSIR manufactured S-Band tubes. Section 5.2.2 shows some typical Rieke plots obtained using the UNMS01 load. With the use of this load the time taken to plot these curves is considerably reduced.

Section 5.3 compares and discusses simulation results from the program CAMPA. Four slot-and-hole magnetrons were modelled. These were chosen from the limited available data in an attempt to obtain as wide a spectrum of tube types as was possible. Two tubes are CSIR manufactured tubes no. 8 and no. 21. The other two tubes are the 4J50 and 2J32 X and S-Band tubes respectively. The data for these last two tubes was obtained from Collins[70].

Measurements were compared to simulated data for various magnetic field strengths. The improvement of the simulations over those of previous workers is discussed. The model equations are reduced to a first order approximation to highlight certain differences between the model and those of other workers.

5.2 UNMS01 Test Results

5.2.1 High Power Tests

The tubes used to test the load were S-Band tubes with an output of 850kW peak, 600W average giving a duty cycle of 0,00071. The load was pressurised using SF_6 to increase the stepper motor speed (Chapter 4). At a VSWR of 1,5:1 the peak power output measured exceeded 900kW. The load operated reliably at these powers; unfortunately no higher power tubes were available to be able to check the load above 1MW.

Increased arcing at these power levels initially resulted in unreliable computer and stepper controller operation. It turned out that the HP9816 computer was more prone to malfunction in the presence of mains noise than a IBM PC connected to the same supply. Mains and GPIB bus filtering reduced the problem; however the only reliable method of controlling the motors would be by complete isolation using fibre optic links between controller and load.

5.2.2 Rieke Plots

Figures 5.1 and 5.2 overleaf show Rieke plots of two of the S-Band magnetrons. Power indicated is average, and curves drawn beyond the reflection coefficient = 0,2 (VSWR = 1,5:1) circle are extrapolated.

The first, labeled the 4844, shows a higher average power output and hence a higher peak power output. This was at the expense of a higher measured pulling figure (12MHz compared to 6,5MHz for the magnetron no 8). Increased coupling in the case of magnetron no. 8 would increase the power output.

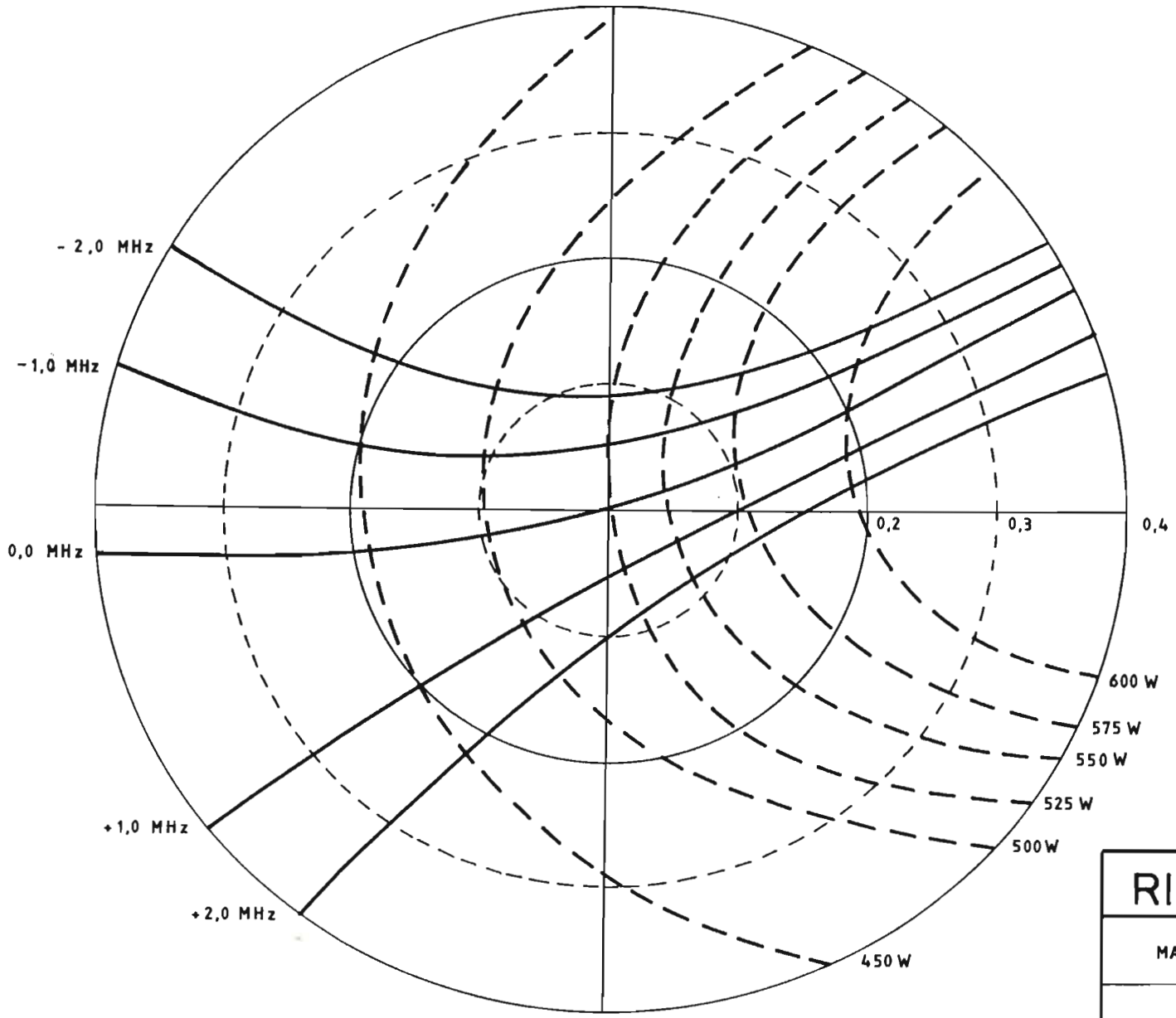

RIEKE DIAGRAM

MAGNETRON no. 4844	2,780 GHz
duty cycle 0,00072	16/6/86

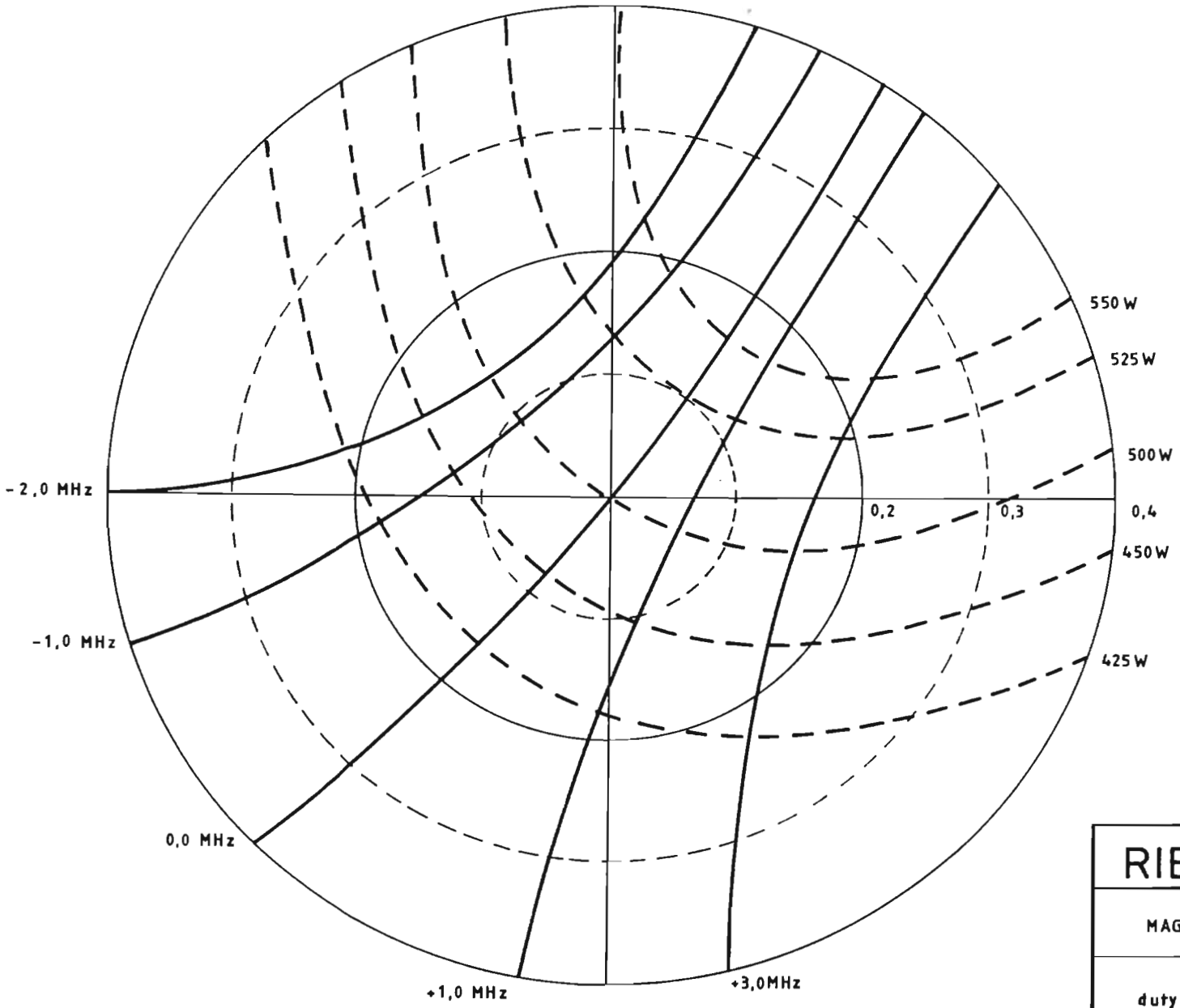

RIEKE DIAGRAM

MAGNETRON no. 8	2,823 GHz
duty cycle 0,00072	16/6/86

5.3 Simulation Test Results

Four magnetrons were modelled; two are S-Band tubes and two are X-Band tubes. One of the S-Band tubes (no. 8) and one of the X-Band tubes (no. 21) are CSIR manufactured tubes; while the other two tubes are modelled from mechanical data obtained from Collins[70]. The program CAMPA is capable of predicting the anode current, power output and efficiency as the anode voltage and the working magnetic field is changed. For illustrative purposes power output has been included in the plots only for the CSIR magnetron no. 8; for the other three tubes the main area of interest was the anode current-voltage curves as the magnetic field changed.

5.3.1 CSIR Magnetron No. 8

This is a tuned magnetron operating at a centre frequency of 2,8GHz. Figure 5.3.1 shows the predicted magnetron performance curves for four values of magnetic field. The solid lines indicate predicted curves while the squares represent measured data. Only data at one value of magnetic field could be obtained. Good agreement is obtained between the measured and predicted data, though it must be born in mind that the error in the measured data is fairly high : $\pm$ 5A and $\pm$ 3kV. The normal operating point for this tube is at 0,27 T and 40 A corresponding to a predicted peak power output of 800kW. The measured output at this current was 750kW $\pm$ 100kW.

5.3.2 CSIR Magnetron No. 21

This is a slot-and-hole fixed frequency magnetron operating at 9,5 GHz. Figure 5.3.2 shows a comparison between the predicted and the measured data for four values of magnetic field. The measured data was obtained from previous tests not conducted by the author, but the accuracy of these readings are in the order of $\pm$ 2A and $\pm$ 2kV. Again good agreement has been obtained between the measured and predicted curves.

Simulation results
CSIR Magnetron # 8

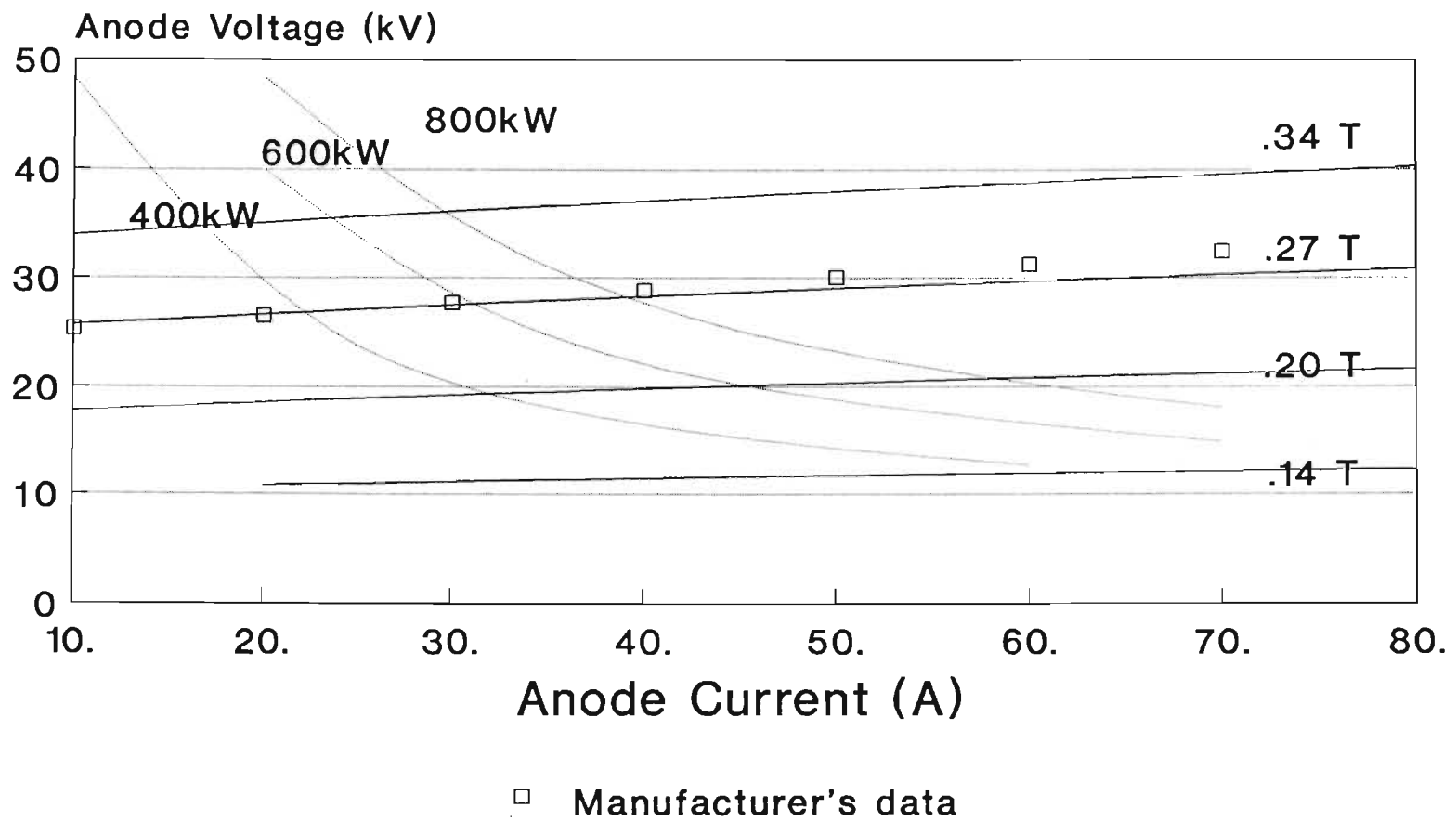

Frequency 2,813GHz Pulling Figure 15 MHz

Simulation Results
Magnetron MAG21

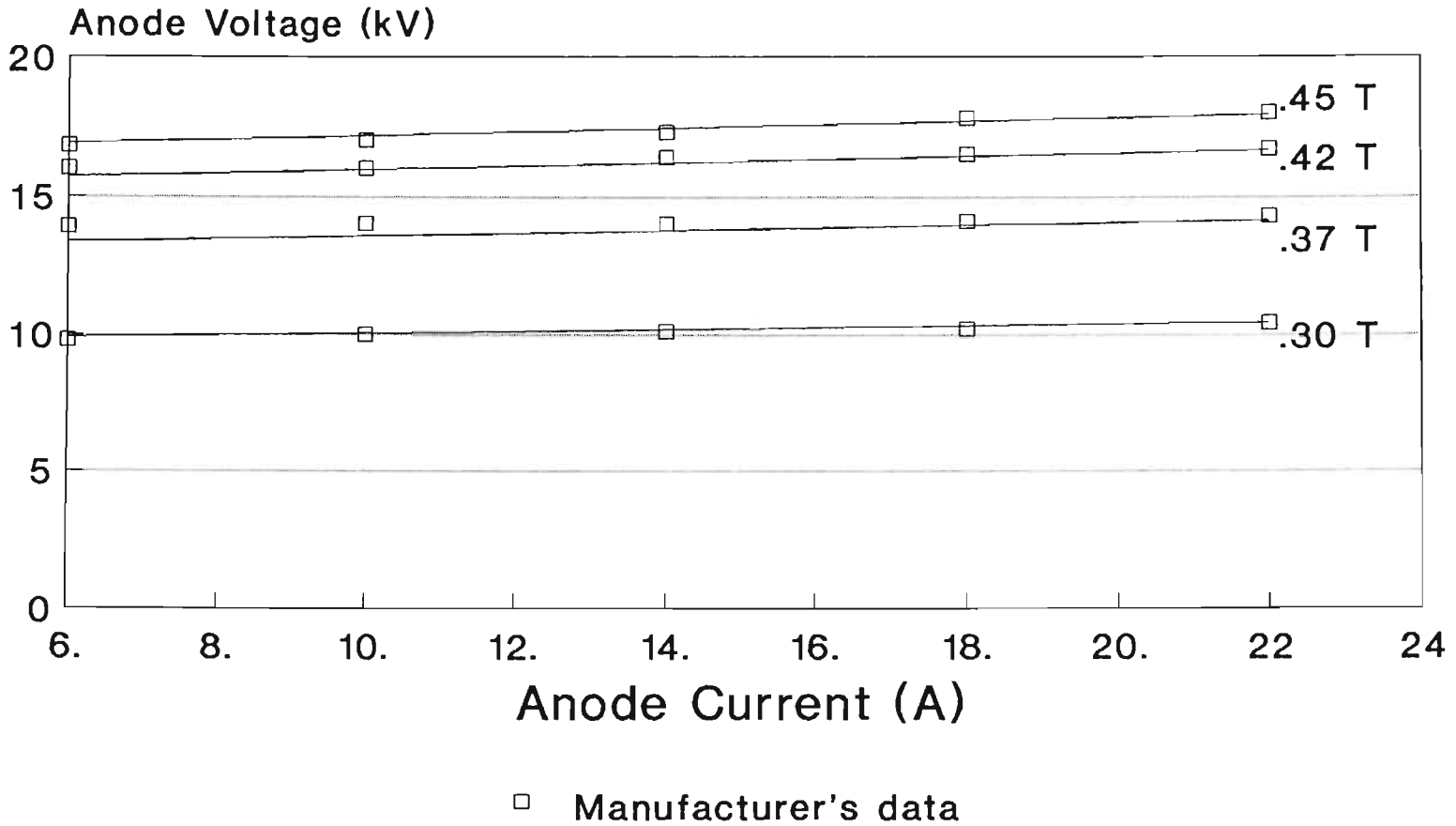

Frequency 9,492MHz Pulling Figure 18MHz

Figure 5.3.2

5.3.3 Magnetron 4J50

This is a fixed frequency slot-and-hole magnetron. Data has been obtained from Collins. Curves have been plotted for four values of magnetic field. The normal operating curve is the 0,63 T line. The predicted oscillating frequency is 9,161GHz but this may be altered by adjusting the strap spacing. Again, good agreement has been obtained between measured and predicted data.

5.3.4 Magnetron 2J32

This tube is one of a range of fixed frequency tubes operating in the S-Band. Two operating curves have been plotted. Again, relatively good agreement has been obtained between the predicted curves and the measured data provided by Collins.

Simulation Results

Magnetron 4j50

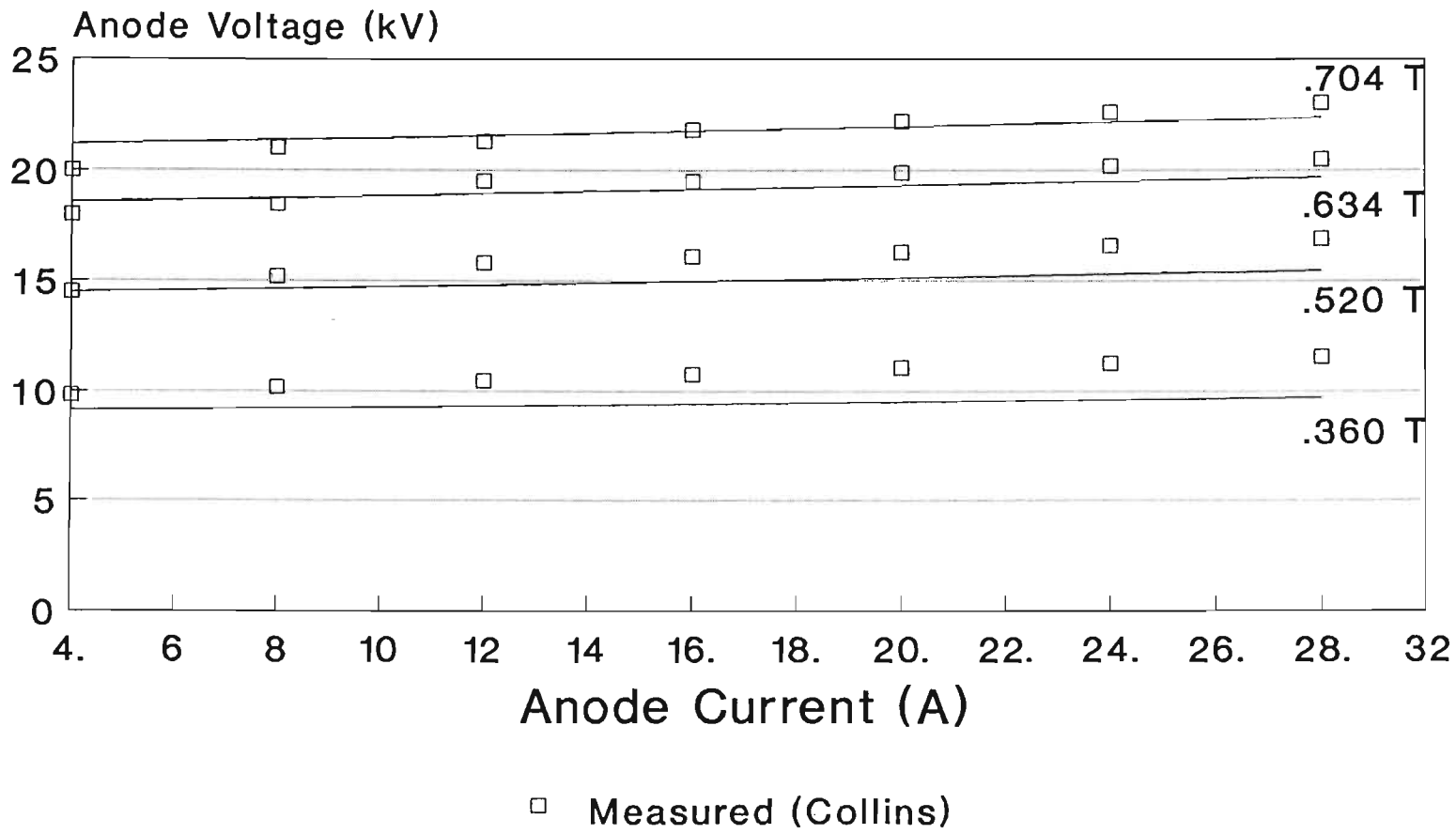

Frequency 9,161GHz Pulling Figure 12MHz

Simulation Results
Magnetron 2J32

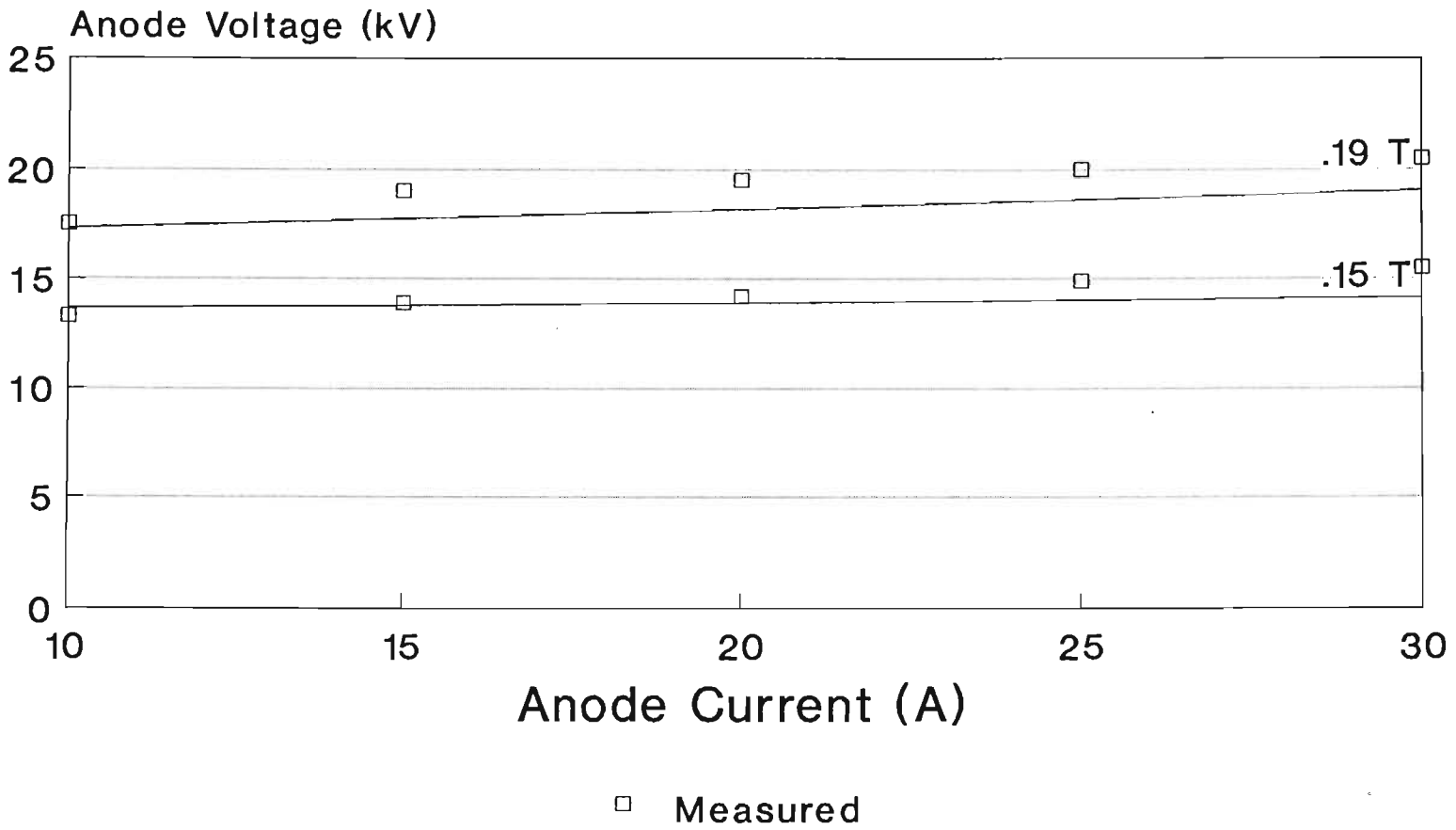

Frequency 2800MHz Pulling Figure 12MHz

Figure 5.3.4

5.4 Discussion of Results

5.4.1 Effect of the Welch Field Criteria

Figure 5.4.1 shows an expanded plot of data obtained from the program CAMPA for the CSIR magnetron no. 8 at a magnetic field of 0,27 T (top curve labeled Schumann). It has already been pointed out that this curve compares well with measured data obtained. This has been compared to data obtained by implementing Vaughan's model in a computer program (lower curve labeled Vaughan).

The first point to note is that Vaughan's curve has a higher dynamic impedance than the measured data. Applying the WFC to Vaughan's model changes that curve to the second lower curve (labeled Threshold). This now correctly predicts the dynamic impedance. The intersection between the two lower curves is at the Hartree voltage for the tube. This improvement has already been noted by Vaughan[71] in a correction note published subsequently to his original paper. It was noted that the introduction of a factor 2 in the Welch voltage threshold criteria resulted in this improvement (corresponding to F = 2 in equation (3.3.22)). The reason for introducing this additional factor was however an attempt to correct an earlier error, and not as a result of using field threshold conditions.

The second point to note is that the lower two curves lie considerably lower than the measured data. The difference is directly as a result of space charge effects. Space charge depression lowers the fields at the base of the spoke which ultimately results in an increased anode voltage. In this case the space charge effects correspond to an equivalent space charge voltage of approximately 5kV.

Comparing the simulations obtained from CAMPA to those of Bayburin[19] (who also predicted the performance of the 2J32 magnetron) reveals that though the dynamic impedance predicted is correct, his predicted curves lie above the measured data. This appears to be directly as a result of the formula used to calculate the spoke current. If the predicted data were to deviate from measured data it would be expected that the measured data would lie above the

Model Comparison
CSIR Magnetron 8

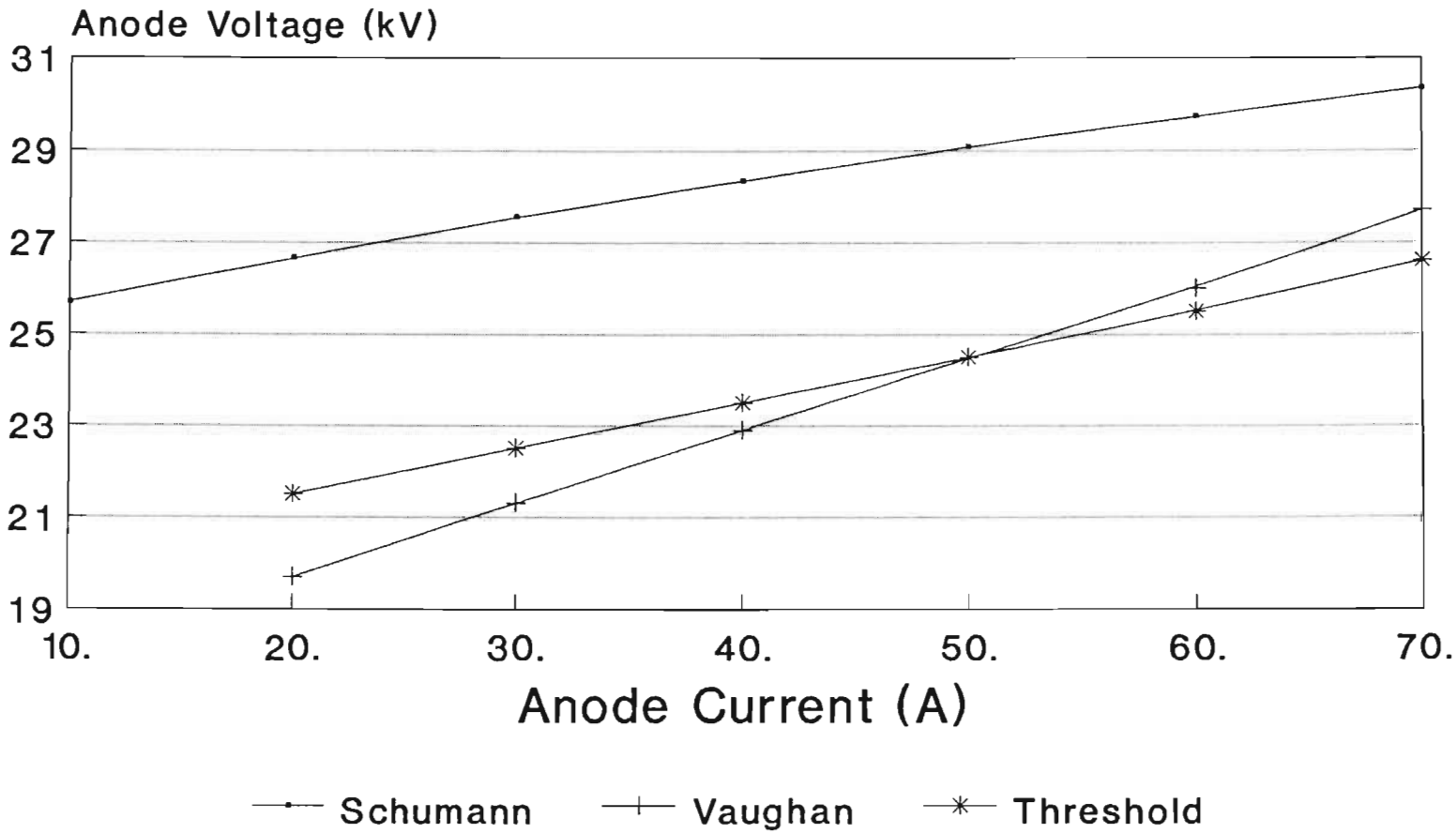

Frequency 2,813GHz Pulling Figure 15MHz

predicted data since a number of additional volt-drops (for example cathode leads) would be measured in the practical system that are not taken into account in the model.

5.4.2 Dynamic Impedance Change with a Change in Magnetic Field

The additional improvement to the model implemented in CAMPA is the form of the spoke current equation. Here spoke current is calculated at the base of the spoke, while in Vaughan's model the spoke current is obtained from a calculation of current between the anode and cathode. This relies on a presumed spoke shape, which as shown in Chapter 2 can be difficult to determine. Bayburin on the other hand calculated the spoke current by taking the charge between the synchronous and the Brillouin radii to contribute to the anode current. Here we briefly show that, even though the formula used in CAMPA to calculate the spoke current at the base of the spoke is a simplification, it is consistent with measured magnetron characteristics.

Measured magnetron characteristics show that the dynamic impedance of the magnetron decreases with a decrease in magnetic field strength. Predictions of magnetron performance obtained from Vaughan's model show the opposite; the dynamic impedance increases with a decrease in magnetic field strength. To examine why this should be the case, the pertinent model equations from Chapter 3 are simplified into first order approximations.

The Welch field criteria (equation (3.4.26)) may be linearised as follows :

$$(V_{as} - V_a + V_{sc})A_3 = (\pi/2 - \beta_n)V_{rf} \qquad (5.1)$$

Where A_3 is a constant independent of bias

$$A_3 = F \qquad (5.2)$$

The output power relationship becomes

$$I_a V_a = A_2 V_{rf}^2 \qquad (5.3)$$

where A_2 is related to the tube efficiency and depends on the magnetic field. It is often found that since tube losses are a fixed fraction of the input power the lines of constant efficiency lie along the operating curve for a particular value of magnetic field. The tube efficiency can thus to the first order be taken as independent of anode current and voltage and depending only on the magnetic field.

$$A_2 = 1/2\ G_e \eta \qquad (5.4)$$

The anode current equation (equation (3.5.1)) becomes

$$I_a = A_1 V_{rf} \beta_n \qquad (5.5)$$

These 3 equations may be used to obtain a current-voltage relation by eliminating V_{rf} and β_n.

Approximating (5.1) by taking $V_{sc} = 0$ we obtain

$$A_3 V_a + \pi/2\ (V_a I_a / A_2)^{1/2} - I_a/A_1 - A_3 V_{as} = 0 \qquad (5.6)$$

For a given V_a the corresponding anode current can be determined from (5.6) by iteration.

The dynamic impedance (dV_a/dI_a) at the threshold voltage V_{as} may be determined from (5.6)

$$dV_a/dI_a \Big|_{\text{threshold}} = m_1 = 1/(A_1(A_1\pi^2/4A_2 + 2A_3)) \qquad (5.7)$$

In order to estimate the change in dynamic impedance m_1 as the magnetic field is changed we examine the dependence of the constants A_1 A_2 and A_3 on the magnetic field.

The factor A_3 does not depend on magnetic field, while, to the first order A_2 may be taken to have a direct dependence on B. The factor A_1

has an inverse dependence on B since to the first order h depends on $1/B^2$ (equation B.11 and noting that V_a depends directly on B) and ρ depends on B^2 (equation (B.12)). Thus the factor A_1^2/A_2 in equation (5.7) will depend on B^{-3}. An increase in B will thus result in an increase in m_1. The higher the magnetic field, the higher the dynamic impedance. If however the spoke current is calculated within the interaction space (as in the case of Vaughan's model) the factor A_1 depends on B since the spoke current has no strong dependence on the thickness of the Brillouin hub h (or $r_b - r_c$ in the case of the cylindrical tube). The result is that the dynamic impedance m_1 depends on 1/B, and increases with a decrease in magnetic field strength. In the case of Bayburin's model the dynamic impedance will show little dependence on the magnetic field.

This argument is consistent with the interaction picture built up in Chapter 2. The current is drawn from the edge of the Brillouin hub and depends on the width of the hub and the transverse field at this point. An increased magnetic field will result in a decreased Brillouin hub thickness and thus the hub surface is further away from the influence of the RF electric field (the field depending approximately on y in this area). Thus a greater anode voltage change will be necessary to obtain the same current change resulting in a higher dynamic impedance.

5.5 Conclusion

High power tests conducted on the UNMS01 microwave power load were successful. The load has been used to generate Rieke plots for two of the CSIR's high power S-Band magnetrons. These diagrams may be plotted quickly and easily using this load. In addition the user knows that the accuracy of the load is better than could be expected with conventional designs.

The program CAMPA, an implementation of model equations from Chapter 3 and Appendix D, has been tested using four slot-and-hole magnetrons. Predicted results agree well with measured data. In addition the author's model improvements outlined in sections 3.3-3.5 of chapter 3 have resulted in a significant improvement in the model's ability to

predict the magnetron current-voltage curves, particually with respect to the dynamic impedance change with change in static magnetic field. As shown, these improvements result in a model representation that more closely agrees with the actual interaction phenomena within the device but keeps the analytical simplicity of previous models.

CHAPTER 6

CONCLUSION

A new and improved analytic magnetron model has been proposed that correctly models the performance of four selected magnetrons. This model has been implemented by the author in the Computer Aided Magnetron Performance Analysis program CAMPA. The model introduces threshold conditions that depend on electric field strengths at the surface of the Brillouin hub rather than voltages at the anode and cathode. This results in the correct prediction of the tube dynamic impedance. Space charge depression effects have been included to enable accurate performance prediction of the magnetron operating characteristics.

The methods previously used to calculate the anode current resulted in a tube dynamic impedance that decreased with an increased magnetic field. In practice however measurements show that the tube dynamic impedance increases with an increased magnetic field. This magnetron model evaluates the anode current at the base of the spoke. This results in a model that has only a second order effect on the spoke shape, and in addition correctly predicts the increase in the dynamic impedance with an increase in the magnetic field strength. Tests conducted on four magnetrons show that the performance predicted has been improved from that predicted by workers in the past using analytic models based on power conservation. The model nevertheless retains its desired analytic simplicity and may be implemented in any small computer system.

A novel high performance magnetron load has been developed that has characteristics superior to conventional available loads. The load allows the variation of VSWR along any path within the VSWR = 1,5:1 circle thus simplifying the plotting of Rieke diagrams and the determination of pulling figures. The VSWR at match is better than 1,02:1, and the load has been tested to powers in excess of 900kW peak. The load uses a stub construction technique which is unique. This construction is cost effective since it uses easily available materials.

A novel broadband high power water load has been proposed that returns a VSWR of better than 1,04:1. This load is relatively simple to construct and requires no waveguide modifications.

REFERENCES

1. Collins, G B, ed., "Microwave Magnetrons", McGraw-Hill, New York (1948)

2. Okress, E., ed., "Cross-Field Microwave Devices", Academic Press, New York, Vols. I and II (1961)

3. Yu, S.P., Kooyers, G.P., "Time-Dependent Computer Analysis of Electron-Wave Interaction in Crossed Fields", Journal of Applied Physics, 36, No. 8, 2550-2559 (1965)

4. Bayburin, V.B., Sobolev, G.L., "Calculation of Space-Charge Fields of a Planar Magnetron", Radio Eng. Electronic Physics, 11, 5, 742-750 (1966)

5. Bayburin, V.B., Sobolev, G.L., "Analysis of the Non-linear Regime of a Multi-Resonator Magnetron with Space", Radio Eng. Electronic Physics, 12, 3, 440-448 (1967)

6. Bayburin, V.B., Sobolev, G.L., "Design of Basic Electrical Parameters of Multicavity Magnetrons", Radio Eng. Electronic Physics, 12, 1493-1498 (1967)

7. Vaughan, J.R.M., " A Model for Calculation of Magnetron Performance", IEEE Trans. Electron. Devices, ED-20, 9, 818-826 (Sept 1973)

8. Welch, H.W., "Prediction of Travelling Wave Magnetron Frequency Characteristics", Proc. IRE, 41, 11 (Nov. 1953)

9. Shein, A.G., Gerasimov, V.P., " Electron Transjectories in Crossed Fields", Theoretical and Mathematical Physics, 45, 859-861 (July 1976)

10. Shaw, E.K., "Starting in the Cold Cathode Distributed Emission Crossed Field Amplifier", IEEE Trans. Electron Devices, ED-24, 1, 22-26 (Jan.1977)

11. Thomas, G.E., "A non-linear theory for a microwave crossed field amplifier", Int. Elec. Dev. Meet. Tech. Digest, 176-179 (Dec.1980)

12. Thomas, G.E., Wilczek, A.S., "Solitons and Microwave Crossed Field Amplifier Characteristics", International Electron Dev. Meet. Washington DC, 500-503 (Dec. 1981)

13. Palevsky, A., Bekefi, G., Drobot, A.T., "Numerical Simulation of Oscillating Magnetrons", J. Appl. Phys., 52, 8, 4938-4941 (Aug 1981)

14. Ludeking, L.D., et. al., "Simulation and Analysis of a re-enterant Planar Magnetron", International Electron Devices Meeting Wash. DC., 160-163 (Dec. 1987)

15. Tertyshnyi, A. S., "The use of the Structural Method to Calculate the Electrostatic Field of a Magnetron", Radioelectron. and Commun. Syst. (USA), 24, 12, 17-20 (1981)

16. Ruden, T.E., Dombrowski, G.E., "A field analysis for the identification of the spurious models of the Coaxial Magnetron", Conf. Proc. of the 11th European Microwave Conf., 650-654 (Sept 1981)

17. Zhou Yong-Liang, Hu Zhoa-Fu, "Computation of the Parameters of the Magnetron Resonator by Finite Element Method", NTG Fachber. (Germany), 85, 91-94 (1983)

18. Allen, R., Clark, M.J., "Application of the Symmetrized Transmission-Line Matrix Method to the Cold Modelling of Magnetrons ", International Journal of Numerical Modelling : Electronic Networks Devices and Fields, 1, 61-70 (Jan. 1988)

19. Bayburin, V.B., "An Analytical Model of the Magnetron", Radio Eng. And Electron. Phys. (USA), 28, 2, 78-85 (1983)

20. Krasnenko, M.U., "Analysis of Orbital Resonance Process at the Magnetron Oscillator Cathode", Radiotekh. and Electron. (USSR), 28, 8, 125 (Aug. 1983)

21. Bayburin, V.B., et. al., "Cylindrical Model of a Magnetron Amplifier with distributed Emission and a closed Electron Flow", Radio Eng. and Electron. Phys. (USA), 29, 3, 90-97 (1984)

22. Bayburin, V.B., Il'In Ye. M., "Analytical Estimate of the Limiting Parameters of Magnetron Oscillators", Soviet Journal of Communications Technology, 30, 9, 107-110 (1985)

23. Ludeking, L., pers. comm.(1987)

24. Granatstein, V.L., Alexeff, I.A., (eds.), "High Power Microwave Sources", Artech House Inc.,(1987)

25. Palevsky, A., et. al., "High Power Magnetron Experiments and Numerical Simulation", Proc. 4th Int. Topical Conf. on High Power, 2, 861-868 (June 1981)

26. Chekanova, L.N., et. al., "Investigation of High-Power Microwave Generation in Relativistic Magnetrons", Proc. 4th. Int. Topical Conf. on High-Power, 2, 839-846 (June 1981)

27. Ballard, W.P., et al., "A Relativistic Magnetron with a Thermionic Cathode", J. Appl. Phys. (USA), 53, 11,1, 7580-7591 (Nov. 1982)

28. Ballard, W.P., Self, S.A., Crawford, F.W., "Theoretical Considerations for Relativistic Magnetrons", Int. J. Electron. (GB), 55, 5, 687-697 (Nov. 1983)

29. Lovelace, R.V., Young, T.F.T., "Relativistic Hartree condition for magnetrons: Theory and comparison, Phys. Fluids, 28, 8, 2450-2452 (Aug. 1985)

30. Vaughan, J.R.M., "Some Closed-Form Expressions for Relativistic Crossed-Field Electron Trajectories", IEEE Trans. Electron. Devices, ED-30, 12, 1704-1709 (Dec. 1983)

31. Thomas, G.E., "An Alternative Theory for the Relativistic Magnetron", J. Appl. Phys. (USA), 53, 11,1, 7572-7579 (Nov. 1982)

32. Morton, A.R., Clark, M.J., "Electronic Tuning of Magnetron Oscillators using PIN Diodes", Int. Conf. on Microwave tubes in Systems Lon. Eng., 4-6 (Oct. 1984)

33. Gunnarsson, T.S., "A Design for a Stepper-Motor-Tuned magnetron", Int. Conf. on Microwave Tubes in Systems Lon. Eng., 1-3 (Oct. 1984)

34. "Magnetron's Tuning Fork gives it Frequency Agility", MSN Microwave Syst. News (USA), 14, 2, 138-139 (Feb. 1984)

35. Mitchell, B., "EE Valve debuts the 'dupletron'", Microwaves and RF (USA), 24, 8, 43-44 (Aug.1985)

36. Latham, R., King, A.H., Rushforth, L., "The Magnetron", Chapman & Hall Ltd., (1952)

37. Hinkel, K., "Electronic Valves Book XV : Magnetrons", Philips Technical Library, (1961)

38. Sims, G.D., Stephenson, I.M., "Microwave Tubes and Semiconductor Devices", Blackie and Son Ltd., (1963)

39. Article by J.J. Coupling, A Pseudonym of J.R. Pierce, which appeared in the February 1948 edition of "Astounding Science Fiction", a Street and Smith publication.

40. Beck, A.H.W, Ahmed, H., "An Introduction to Physical Electronics", Edward Arnold, (1973)

41. Buck, J.G., Clogston, A.M., "Microwave Magnetrons", Edited by G.B. Collins, McGraw-Hill Book Company, pp 503-539, (1948)

42. Buneman, O., "Crossed Field Microwave Devices", Edited by E. Okress Vol. 1 : "Principle Elements of Crossed Field Devices", Academic Press, pp 209-233, (1961)

43. Feinstein, J., "Crossed Field Microwave Devices", Edited by E.

Okress Vol. 1 : "Principle Elements of Crossed Field Devices", Academic Press, pp 554-579, (1961)

44. Slater, J.C., "Microwave Electronics", Van Nostrand, New York, (1950)

45. Kroll, N., "Microwave Magnetrons", Edited by G.B. Collins, McGraw-Hill Book Company, pp 49-82, (1948)

46. Collins, R.E., "Foundations for Microwave Engineering", McGraw Hill, (1966)

47. Schumann, E.W., "Computer Aided Magnetron Performance Analysis", Report no. EWSMAG02, University of Natal, (1986)

48. Altman, J.L., "Microwave Circuits", D. van Nostrand Company Inc., (1964)

49. Darko Kajfez, W. Perry Wheless, "Invariant Definitions of the Unloaded Q Factor", IEEE Trans. on Microwave Theory and Techniques, MTT34, 7, 840-841 (1986)

50. Walker, K.R., "Microwave Magnetrons", Edited by G.B. Collins, McGraw-Hill Book Company, pp 167-203, (1948)

51. Millman, S., Smith, W.V., "Microwave Magnetrons", Edited by G.B. Collins, McGraw-Hill Book Company, pp 460-501, (1948)

52. Bakish "Space-Charge Flow",

53. Hayt, W.H., "Engineering Electromagnetics", McGraw-Hill, (1974)

54. Novick, G., Hull, J.F., "Microwave Magentrons", Edited by G.B. Collins, McGraw-Hill Book Company, pp 580-588, (1948)

55. Hull, J.F., "Microwave Magnetrons", Edited by G.B. Collins, McGraw-Hill Book Company, pp 496-527, (1948)

56. Shimizu T., "Crossed Field Microwave Devices", Edited by E. Okress Vol. 1 : "Principle Elements of Crossed Field Devices", Academic Press, pp 589-595, (1961)

57. Nishimaki M., "Crossed Field Microwave Devices", Edited by E. Okress Vol. 1 : "Principle Elements of Crossed Field Devices", Academic Press, pp 596-607, (1961)

58. Herlin, M.A., Smith, A.G., "Microwave Magnetrons", Edited by G.B. Collins, McGraw-Hill Book Company, pp 698-738, (1948)

59. Vaughan, J.R.M., "Observations of Multipactor in Magnetrons", IEEE Trans. on Electron Devices, ED-15, 11, 883-889, (1968)

60. Arndt, F., Bornemann, J., Vahldieck, R., "Design of Multisection Impedance-Matched Dielectric-Slab filled Waveguide Phase Shifters", IEEE Trans. on Microwave Theory and Techniques, MTT-32, 1, 34-39, (1984)

61. Collin, R.E., "Waveguide Phase Changer", Wireless Engineer, 82-88, (March 1955)

62. Collin, R.E., "Foundations for Microwave Engineering", McGraw-Hill, (1966)

63. Csendes, Z.J., "Numerical Solution of Dielectric loaded Waveguides : I - Finite Element Analysis", IEEE Trans. on Microwave Theory and Techniques, MTT-18, 12, (1970)

64. Montgomery, C.G. Dicke, R.H., Purcell, E.M., eds., "Technique of Microwave Measurements", MIT Radiation Laboratory Series Vol. 11, McGraw-Hill, (1947)

65. Marcuvitz, N., ed., "Waveguide Handbook", MIT Radiation Laboratory Series Vol. 10, McGraw-Hill, (1951)

66. Harrington, R.F., "Time Harmonic Electromagnetic Fields", McGraw-Hill, (1961)

67. Ciavolella, J., "Take the Hassle out of High Power Design", Microwaves, (June 1972)

68. Burkhart, S., "Coaxial E-Field Probe for High-Power Microwave Measurement", IEEE Trans. on Microwave Theory and Techniques, MTT-33, 3, 262-265, (1985)

69. Schumann, E.W., "Report on CSIR visit 11/6/86 to 13/6/86", Report no. EWSMAG01, University of Natal, (1986)

70. Smith, A.G.,"Microwave Magnetrons", Edited by G.B. Collins, McGraw-Hill Book Company, pp 739-796, (1948)

71. Vaughan, J.R.M., "Discussion of Incorrect Equations in 'A Model for Calculation of Magnetron Performance'", IEEE Trans. on Electron Devices, ED-21, 1, (1974)

APPENDIX A

RF FIELD SOLUTION IN THE INTERACTION SPACE

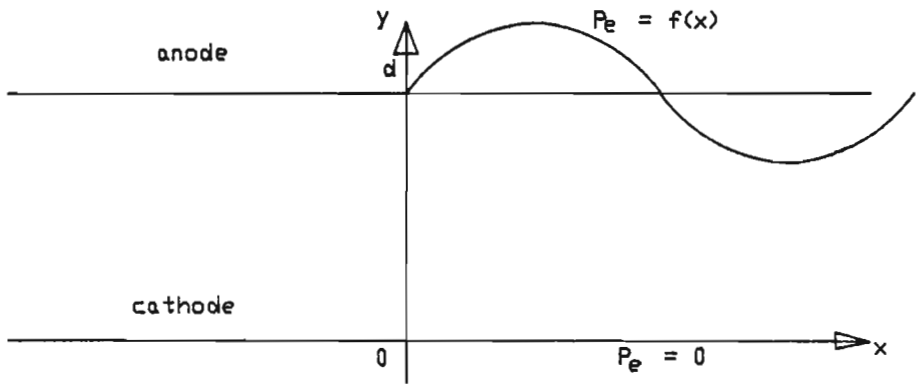

Coordinate System with Anode Potential Distribution

Assuming a static potential distribution at the anode

$f(x) = V_{rf}\sin(\beta x)$, then

$$\partial^2 P_e/\partial x^2 + \partial^2 P_e/\partial y^2 = 0 \qquad (A.1)$$

Set $P_e = XY$ where $X = X(x)$ and $Y = Y(y)$

As a trial solution choose

$X = b\mathrm{Sin}(kx)$

$$Y = a(e^{ky} - e^{-ky}) \qquad (A.2)$$

where a,b and k are constants
Then

$$X'' = -k^2 X \qquad (A.3)$$

and

$Y'' = k^2 Y$

P_e is thus a solution to Laplace's equation (A.1)

$$P_e = XY = ab(e^{kx} - e^{-kx})\mathrm{Sin}(ky)$$

Set m = ab then at x = a

$$XY = V_{rf}\mathrm{Sin}(\beta x) \qquad (A.4)$$

so

$$m(e^{kd} - e^{-kd})\mathrm{Sin}(kx) = V_{rf}\,\mathrm{Sin}(\beta x)$$

hence

$$m = V_{rf}/(e^{kd} - e^{-kd}) \text{ and } k = \beta$$

At x = 0 XY = 0

The solution thus becomes

$$P_e(x,y) = V_{rf}\,\frac{(e^{\beta y} - e^{-\beta y})}{(e^{\beta d} - e^{-\beta d})}\,\mathrm{Sin}(\beta x)$$

or

$$P_e(x,y) = V_{rf}\,\frac{\mathrm{Sinh}(\beta y)}{\mathrm{Sinh}(\beta d)}\,\sin(\beta x) \qquad (A.5)$$

The electric field components are thus

$$E_x^{rf} = -V_{rf}\,\frac{\mathrm{Sinh}(\beta y)\mathrm{Cos}(\beta x)}{\mathrm{Sinh}(\beta d)} \qquad (A.6)$$

and

$$E_y^{rf} = -V_{rf}\,\frac{\mathrm{Cosh}(\beta y)}{\mathrm{Sinh}(\beta d)}\,\mathrm{Sin}(\beta x) \qquad (A.7)$$

APPENDIX B

BRILLOUIN STREAM FOR THE LINEAR MAGNETRON

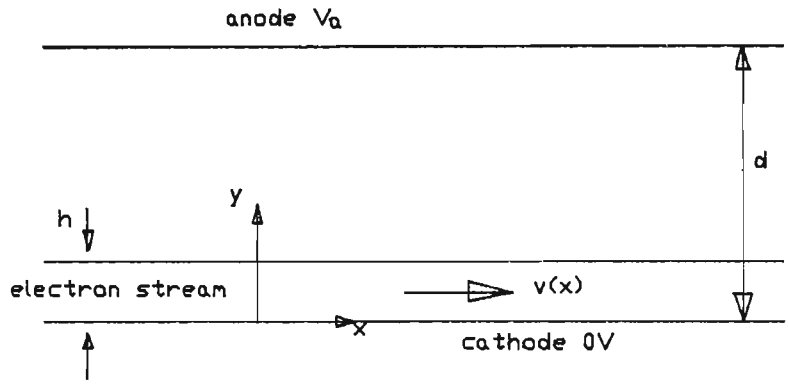

Coordinate System

Assuming Brillouin flow the velocity of the electrons within the stream is

$$v_x = -E_y/B \qquad (B.1)$$

The kinetic energy must equal the potential energy lost thus

$$eP_e = 1/2\ mv_x^2 \qquad (B.2)$$

$$dP_e/dy = mE_y/(eB^2)\ dE_y/dy = -E_y \qquad (B.3)$$

or

$$dE_y/dy = -eB^2/m \qquad (B.4)$$

thus

$$E_y = -eB^2y/m \qquad (B.5)$$

and

$$P_e = 1/2(eB^2/m)y^2 \qquad (B.6)$$

If the swarm height is h the electric field at the edge of the swarm is

$$E_y(h) = -eB^2h/m \qquad (B.7)$$

and the potential at the edge of the swarm is

$$P_e(h) = 1/2(eB^2/m)h^2 \qquad (B.8)$$

Thus the anode potential V_a is given by

$$V_a = 1/2(eB^2/m)h^2 + (eB^2/m)\, h(d - h) \qquad (B.9)$$

$$= \frac{eB^2}{m}h(d - h/2) \qquad (B.10)$$

Solving for h

$$h = d\left(1 - \sqrt{1 - \frac{2mV_a}{eB^2d^2}}\right) \qquad (B.11)$$

The space charge density may be obtained directly from Poisson's equation

$$\rho = -eB^2\varepsilon_o/m \qquad (B.12)$$

which is a constant independent of position.

APPENDIX C

SPACE CHARGE FIELDS

Electric field due to an infinite line charge is

$$E_y = -(\rho_l)/(2\pi\epsilon_o r) \qquad (C.1)$$

where r is the distance between the line charge and the measuring point and ρ_l is the line charge density.

The total field due to the line charge and its images is thus

$$E_y = -\rho_l/(2\pi\epsilon_o d)\ [1/(1/2) + 1/(1/2) - 1/(3/2) - 1/(3/2) \ldots] \qquad (C.2)$$

which approximates

$$E_y = -\rho_l/(\pi\epsilon_o d)\ (1,57) \qquad (C.3)$$

If the line charge is of finite length L then the electric field becomes

$$E_y = -\rho_l L/(\pi\epsilon_o d\sqrt{L^2 + d^2})\ (1,57) \qquad (C.4)$$

which reduces to equation (C.3) if $L >> d$

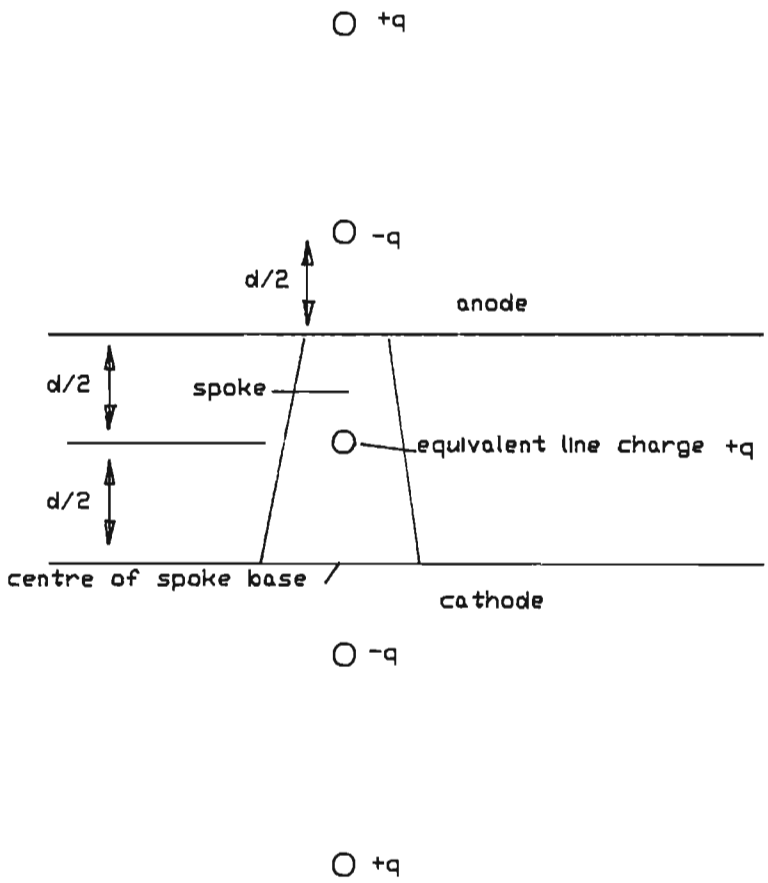

Equivalent Line Charges and their Images

APPENDIX D

PROGRAM IMPLEMENTATION

The program CAMPA was written by using the equations of Chapters 2 and 3. These equations were written for the linear magnetron but may easily be adjusted to suit the cylindrical magnetron. The equations used by CAMPA are given below.

The Hartree Voltage (equation 3.3.7) becomes

$$V_{as} = \frac{Bwr_a^2}{N}(1 - (r_c/r_a)^2) - \frac{2mw^2r_a^2}{eN^2} \qquad (D.1)$$

The Brillouin radius (equation (B.11)) becomes

$$\frac{8mV_a}{eB^2r_c^2} = 2\{(r_b/r_c)^2 - (r_c/r_b)^2\}\ln(r_a/r_b) + (r_b/r_c - r_c/r_b)^2 \qquad (D.2)$$

The Brillouin charge density (equation B.12) becomes

$$\rho = \varepsilon_o\frac{eB^2}{m}(1 + (r_c/r_b)^4)/2 \qquad (D.3)$$

The factor F (equation 3.3.22) becomes (taking into account 3.3.29)

$$F = \mathrm{Sinh}(\beta(r_a - r_c))\frac{h'(\pi h'/P)}{2(r_a - r_b)\mathrm{Sin}(\pi h'/P)} \qquad (D.4)$$

The spoke phase β_n thus becomes

$$\beta_n = \text{acos}[V_{as} - V_a + V_{sc}]F/V_{rf} \qquad (D.5)$$

Where V_{sc} the space charge voltage becomes (from equation 3.4.27)

$$V_{sc} = \frac{2L\,\beta_n r_b P \rho}{SN\pi^2 \varepsilon_o} \qquad (D.6)$$

The peak RF electric field E_p^{rf} at the anode (equation 3.3.28) becomes

$$E_p^{rf} = \frac{V_{rf}}{h'} \sin(\pi h'/P)/(\pi h'/P) \qquad (D.7)$$

The tangential RF electric field at the base of the spoke thus becomes (equation 3.5.4)

$$E_x = E_p^{rf} \frac{\pi(r_b - r_c)\text{Cos(theta)}}{P \quad \text{Sinh}(\pi(r_a - r_b)/P)} \qquad (D.8)$$

The spoke current (equation 3.5.1) thus becomes

$$I^{spoke} = 2\rho L \beta_n r_b E_x/(NB) \qquad (D.7)$$

The characteristic impedance of one resonator is given by (see Section 2.5)

$$Z_1 = 1/w(C_r + C_s) \qquad (D.8)$$

and thus the characteristic admittance of the resonator block is given by

$$Y_o = N/Z_1 \qquad (D.9)$$

The external Q is calculated as per equation (2.6.5) and this allows the calculation of the relevant conductances :

$$G_e = Y_o/Q_e \qquad (D.10)$$

$$G_u = Y_o/Q_u \qquad (D.11)$$

$$G_l = Y_o/Q_l \qquad (D.12)$$

The external power and anode block loss due to resistive heating is given by equations (3.6.6) and (3.6.7).

Anode block losses are given directly by the equations of Section 3.6.2.

Finally Cathode back-heating losses are given by equation (3.6.20)

APPENDIX E

Computer Aided Magnetron Performance Analysis

Report EWSMAG02

REPORT NO.EWSMAG02

COMPUTER AIDED MAGNETRON PERFORMANCE ANALYSIS

E.W. Schumann
Dept. Electronic Engineering
University of Natal
Durban
14/08/86

SUMMARY

This report describes the Computer Aided Magnetron Performance Analysis program CAMPA. This program has been written at the University of Natal to help the design engineer analyse the performance of existing magnetron designs or to predict the performance of new designs. The program is currently running on the Department of Electronic Engineering's A900 computer, accessible on the EENET network.

1.0 Introduction

CAMPA is an easy to use magnetron performance analysis program. The tube designer need simply specify the magnetron dimensions, working field and output load. A large amount of output data is generated, which includes power output, efficiency and anode current. Full details of the input requirements and outputs obtained are listed in Chapters 3 and 4. A sample input/output listing is provided in Chapter 5. Chapter 6 discusses the program accuracy, whilst Chapter 7 describes future development work.

A few general comments on the use of computer analysis programs are here in order. The program should be viewed as the design aid that it was intended to be - generally a fairly accurate indicator of changes of outputs as a result of design changes - rather than providing high absolute accuracy. In the case of CAMPA, the user must ensure he realises the limitations as spelt out in Section 6.0.

2.0 PROGRAM STRUCTURE AND COMMANDS

The program is fairly modular and consists of a number of routines as described in Apppendix A. The user-interface routines are easily altered to allow post-processing of the output data as required by individual users.

2.1 Commands

To run the program, type CAMPA, followed by a return. All the input options are displayed at the top of the screen, with the prompt 'what now?' appearing in the lower left hand corner.

The input can now be either a command or a tube specification. There are currently six commands available.

2.1.1 Analyse Tube Performance

Format:

```
      analyse
  or  analyse fully
  or  analyse graph*
  or  analyse sensitivity to  parameter
```

2.1.2 Recall a Tube on File

Format: recall filename

In all cases, filename is presumed to have a '.MAG' qualifier.

e.g. recall CSIR5586

recalls data for the 5586 magnetron, stored on a file CSIR5586.MAG

2.1.3 Store a Tube to File

Format: store filename

2.1.4 Scale Data

Format: scale = value

e.g. scale = 0,8

scales all dimensions by 0,8

2.1.5 Restore Display

Format: restore

2.1.6 Program Termination

Format: exit

2.2 Altering Tube Parameters

Tube parameters (dimensions or operating conditions) may be altered simply by typing

parameter = value

e.g. anode height = 1,5e-2

Note the parameter name must be typed as displayed on the screen. Parameter definitions are given in Section 3.0 below.

3.0 PROGRAM INPUT DEFINITIONS

3.1 Tube Dimensions

All dimensions are specified in metres. Fig.3.1 illustrates the definitions used:

1) anode radius
2) cathode radius
3) anode length
4) number of resonators

5) hole radius
6) slot width
7) slot length
8) average strap radius
9) strap height
10) strap width
11) strap separation
12) tuner pin diameter (if needed)
13) tuner pin penetration (maximum penetration)

Note: tuner dimensions are for a mechanical induction type tuner only.

3.2 Operating Conditions

i) working field: specifies the magnetic field at which analysis takes place (units : Tesla)

ii) pulling figure: specifies the output load (units : MHz)

4.0 PROGRAM OUTPUTS

Two printed output formats are possible:

4.1 'Analyse' Output

i) operating frequency : Pi-mode operating frequency
ii) tuner range : maximum deviation from operating frequency
iii) characteristic scaling parameters
iv) cutoff voltage
v) threshold (Hartree) voltage
vi) unloaded quality factor Qu
vii) mode separation : ratio between wavelengths corresponding to the Pi-mode and the next mode
viii) cold pulling figure : gives the 'cold pulling figure' adjustment parameter needed to obtain the hot pulling figure specified in 3.2 above
ix) summarised performance curve : lists operating points with the

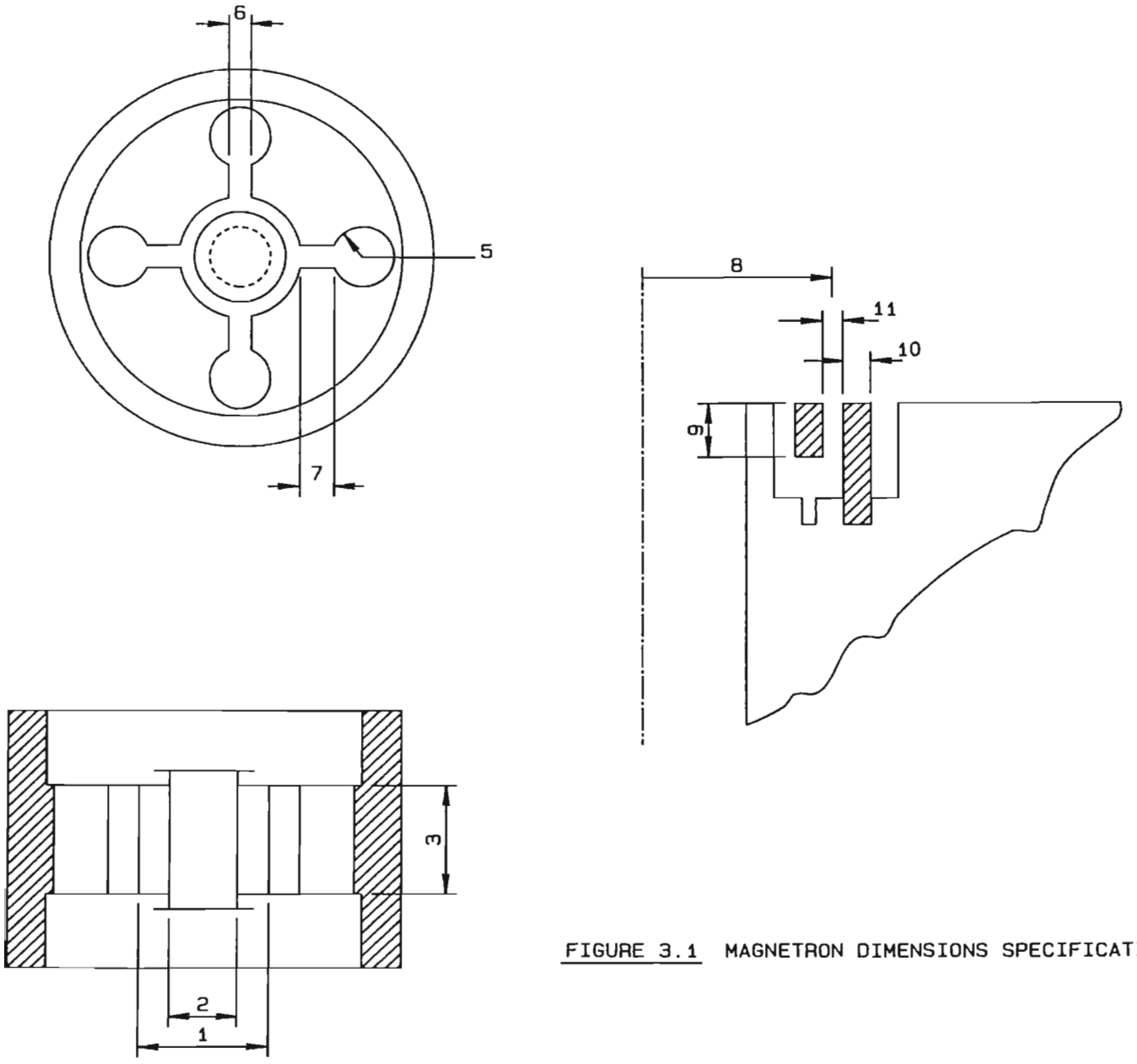

FIGURE 3.1 MAGNETRON DIMENSIONS SPECIFICATIONS.

anode voltage as the independent variable:

Va : anode voltage (V)
Ia : anode current (A)
Pe : output power (W)
eff : output efficiency
push : frequency pushing (Hz)

4.2 'Analyse Fully' Output

An expanded version of the above summarised performance chart is available listing the following outputs as the magnetrons voltage is increased:

Va : anode voltage (kV)
Idc : anode current (A)
Pe : external (output) power (kW)
Pu : internal anode block losses (kW)
Pa : anode losses due to electron bombardment (kW)
Eff : output efficiency (%)
Vrf : anode block r.f. voltage (kV peak)
theta : phase difference between the r.f. voltage and the electron spoke (degree)
Rb : 'virtual cathode' (or non-synchronous) radius (mm)
Push : pushing figure (MHz)
Cath : cathode current density (A/cm^2)

4.3 'Analyse Sensitivity' output

This analysis increases the specified parameter by 1% and lists the variation of most of the output parameters as a result of the increase. Note that the operating point is chosen so as to keep the anode current constant. This tends to give more meaningful results for efficiency and power variation.

5.0 SAMPLE OUTPUTS

Parameter information for the CSIR's 5586 magnetron is available on file 'CSIR5586'. The analysis output including the summarised performance information is given below.

Operating Conditions : working field : 0,25T
pulling figure : 6,5 MHz

frequency = 2.800 GHz
tuner range = 0,252 GHz

characteristic values:
voltage = 2,46 kV
field = 0,0501 T
current = 10,7 A
power = 26,4 kW
conductance = 0,0043 S

cutoff voltage : 61,6 kV
threshold voltage : 22,3 kV
unloaded quality factor : 1476
mode separation : 0,704
cold pulling factor : 17,3 MHz at $\pm$ 97°

Va	Idc	Pe	Eff	Pushing
20,7kV	24A	310kW	62%	-11MHz
23,2	47	640	58	-9,2
25,0	63	880	55	-8,4

For a detailed discussion of the 5586 performance curves, see Report No. EWSMAG03.

Other illustrative magnetron files available on disc include:

m4550 : 9,2 GHz 150 kW
a725 : 8,6 GHz 40 kW
csirhalfscale : 9,5 GHz 60 kW (scaled 5586)

csirdblscale : 1,4 GHz 1 MW (scaled 5586)

6.0 PROGRAM ACCURACY AND LIMITATIONS

6.1 Accuracy

The magnetron model presently employed scales well, with simulation accuracy being of the order of 10%. In general the predicted anode voltage appears a little lower than in practice; however, the dynamic impedance corresponds well to that measured. The formulas used for anode testing and cathode back-bombardinal are semi-empirical and may not work well at the extremes of operation. A most difficult parameter to calculate is the resonator admittance and the effect of the straps. CAMPA uses a field theory technique to solve the resonator admittance problem, and a simple capacitance formulae to access the influence of the strapping. This has proven to be fairly accurate for the tubes listed in Chapter 5 above.

A number of effects are not taken into account, however - end space effects, cathode limited emission, higher mode output coupling to name a few. If the deviation from existing magnetron designs is not too great, these effects will probably be of limited importance.

6.2 Limitations and Errors

6.2.1 Limitations

At present the analysis is restricted to slot-and-hole type magnetrons with double straps. It would however be a relatively simple task to extand the routines to handle vane type as well as rising sun type tubes.

6.2.2 Design Rule Checking

The program performs a limited number of 'design checks' to detect an impossible design configuration. An error 9 is reported if any of the following conditions occur:

1) cathode radius $>$ anode radius
2) 2π(anode radius)/number of resonators $<$ slot width
3) anode radius $>$ average strap radius
4) average strap radius $<$ anode radius + slot length
5) tuner pin diameter $>$ 2. hole radius
6) tuner penetration $>$ anode height
7) 2π(anode radius + slot length + hole radius)/number of resonators $<$ 2. hole radius

6.2.3 Precision Errors

All calculations are presently performed in single precision, an error 8 may occur if the iterations are limited by the variable precision.

6.2.4 Analysis Error

If at 0.8*(threshold voltage), the synchronous radius exceeds the anode radius, an error 7 is reported. This will probably be due to too small a magnetic field.

6.2.5 Iterative Errors

If convergance cannot be found, an error 3 is reported. This should, in general, not occur!

7. FUTURE WORK

At present, work is in progress to improve the model and replace some of the semi-empirical formulations. Alternate energy conservation analysis may improve the model, while finite element analysis will

provide the possibility of electron motation prediction.

8. PROGRAM LISTING

Program listings are given overleaf. A brief description of the routines is given:

Program	CAMPA	:	main program control
Subroutine	ANALYSE	:	analysis control and display
Subroutine	BOTTOMC	:	positions cursor to bottom of screen
Subroutine	ERROR_CHECK	:	checks errors and reports to screen
Subroutine	STORE_FILE	:	stores parameter information to file
Subroutine	RETRIEVE	:	recalls parameter imformation from file
Subroutine	NEXT	:	parses the next input parameter from string
Subroutine	CLRSCREEN	:	homes cursor and clears the scareen
Subroutine	DISPLAY	:	displays the specified parameter and value
Subroutine	HEAD	:	displays the headings
Subroutine	OP_POINT	:	determines the operating point
Subroutine	RF	:	optimises the operating point
Subroutine	RFOBJECT	:	calculates the operating parameters
Subroutine	RBOPT	:	optimises the syncronous radius
Subroutine	RBOBJECT	:	object file for optimisation
Subroutine	CHECK_DESIGN	:	design rule checker
Subroutine	INITIAL	:	initial analysis subprogram routine
Subroutine	PI_MODE_WAVELENG	:	includes strapping effects (slot+hole)
Subroutine	ZERO_ADMITTANCE	:	determines resonator resonant frequency
Subroutine	ADMITTANCE	:	determines the resonator admittance
Subroutine	CAPACITANCE	:	determines the capacitance of a resonator

APPENDIX F

Microwave Mismatch Unit UNMS01 : Operator's Manual

MICROWAVE MISMATCH UNIT UNMS01

OPERATORS' MANUAL

AND

ENGINEERING DRAWINGS

E W SCHUMANN
DEPARTMENT OF ELECTRONIC ENGINEERING
UNIVERSITY OF NATAL
KING GEORGE V AVENUE
DURBAN, 4001

15 FEBRUARY 1986

CONTENTS

1. INTRODUCTION

This manual describes the installation and operation of the 2,7 to 3,0GHz Triple Stub Mismatch unit UNMS01. The system consists of 3 major component parts: the mismatch/integral load unit, a HP9816 minicomputer and the 3-STUB CONTROLLER electronics. Section 3 of this manual describes the installation of the system and Section 4 describes its operation. Though the unit operation is normally automatic, manual operation is possible though special precautions must be noted. These are described in Section 5. Finally, Sections 6 and 7 are important if the unit needs to be adapted for any use other than that for which it was designed. Full engineering drawings are given and software changes are discussed.

2. SPECIFICATIONS

TYPE:	Triple stub with integral water load
FREQUENCY RANGE:	2,7 - 3,0GHz
MISMATCH RANGE:	VSWR = 1 to VSWR = 1,5
WATER LOAD:	Type: Calorimetric
	Flow rate: 1-2 lpm
	Input/Output connections: 8mm / hose
	Water envelope: tapered Pyrex glass
POWER HANDLING:	Max 1,5MW peak 1kW average

R.F. PICKOFF:	Coupling connection: SMA female
	Coupling factor: -49dB
	(Calibration graph supplied)
PRESSURISATION:	Dry nitrogen 1,5 bar for 1MW*
	SF_6 0,1 bar for 1MW
	0,2 bar min for specified accuracy
	*See software modifications, Section 6.
TEMPERATURE:	10-40^{o}C

3. INSTALLATION

The mismatch system consists of three major component parts:

1) mismatch plus integral waterload
2) HP9816 computer plus disc drives
3) 3-STUB DRIVE CONTROLLER electronics

3.1 Installing the Mismatch Unit

Securely bolt the mismatch unit to the magnetron adaptor. The orientation is not important but clamping the unit in the upright position makes it easier to clear the waterload of air on initial use. If a horizontal position is chosen, additional support on the mismatch unit will be necessary. Ensure that there is at least a 100mm clearance between the end of the stubs and any supporting structure.

Connect the water lines. The inlet tube should be connected to the stub end of the waterload while the outlet should be connected to the short circuit end of the load. These points are marked on the load.

Connect the gas line using 8mm pressure hosing. If SF_6 is used (supplied with the unit) set up the pressure to 0,1 Bar. If dry nitrogen is used, see Section 6 Software Modifications. The

nitrogen pressure should be set to 1,5 Bar.

Connect the RF pickoff. Note that this coupling has a -49dB coupling. Additional attenuation may be needed.

3.2 Installing the Computer and Peripherals

Position the computer at least 1m away from the mismatch unit or any other unscreened high voltage equipment.

Connect the mains filter (supplied) to a 240V 50Hz outlet. Connect to the filter the plug outlet supplied with the system. This provides outlets for the computer, disc drive unit and 3-STUB CONTROLLER. The additional power point may be used for any additional electronic equipment needing mains protection.

Interconnect the disc drive, computer and 3-STUB controller using the HPIB bus cable supplied.

Connect the computer asynchronous point to the 3-STUB RS232 point.

Connect the mismatch unit to the 3-STUB controller using the cable supplied.

Ensure all units are initially switched off.

3.3 Booting the System

Insert the software disc supplied into the left-hand drive. Switch on the disc drive, then switch on the computer. After approximately one minute, the message 'Basic ready' will appear on the screen. At this point type LOAD "maindrive", then press RUN. Respond to the prompt "Need to index" with a y followed by a RETURN. When the message "Please switch on 3-STUB CONTROLLER" appears, switch on the controller. The program de-energises the drives at this point to enable the stubs to be rotated by hand.

In response to the prompt "What is the calibration file?", type in calfile. As soon as the file has been read, the system is ready for use.

3.4 Initial Indexing

Even though the controller program stores the stub positions onto disc after every run, the actual position may differ after transport and it will be necessary to index the motors. To do this proceed as follows:

Press the "MANUAL RUN" softkey
Press the "INDEX MOTORS" softkey. Once the softkey menu reappears, press "MANUAL END" to return to the main menu. Indexing is now complete.

4. OPERATION

See sections 3.3 and 3.4 for initial startup. If the previous system status is known, it will not be necessary to do an initial index. However, if the stubs have been returned to the transport position from a previous run, indexing is recommended.

4.1 Modes of Operation

Two basic modes of operation are possible; the "meas freq" mode and the "spec freq" mode. The former measures the magnetron operating frequency before calculating the next tuner position while the latter presumes that the frequency is fixed to that specified. The "meas freq" mode is preferred for accuracy, while the "spec freq" mode is substantially faster in terms of cycle time. To toggle from or to either mode first press "MANUAL RUN" and then press the "meas freq" or "spec freq" button. The power up default is "meas freq".

4.2 The Auto Run Option

Pressing the "AUTO RUN" button initiates the following sequence:

- all stubs are indexed (if necessary)
- one stub is positioned to the VSWR required (default = 1,5)
- the mismatch phase is rotated (keeping the VSWR constant) through 360^{o}
- the stubs are returned to a matched condition

4.3 The Manual Run Option

This is similar to the AUTO RUN OPTION but allows the operator to separately execute the AUTO RUN sub-functions. In addition, the user may:

- specify the VSWR required
- specify the "spec freq" frequencies
- specify the calculation error

The last function is useful if the operator wants greater accuracy in the stub position calculations. Greater accuracy results in smaller stub steps while increasing the cycle time. As a guide:

Calculation limit = 0,02 (default) = cycle time 4 min
= 0,05 = cycle time 3 min
= 0,01 = cycle time 6 min
= 0,005 = cycle time 10 min

A calculation limit of 0,02 results in an error of roughly /p/=0,008 while a limit of 0,01 results in an error of roughly /p/=0,004.

4.4 The Display Options

Two display options are possible: "plot VSWR" and "plot delta f"

The operator may toggle from one to the other from either the AUTO or MANUAL menus. The "plot VSWR" option plots a polar linear display of the reflection coefficient as seen from the mismatch unit flange. The "plot delta f" option on the other hand plots the change in oscillator frequency as a function of mismatch VSWR and phase. Clearly, the latter is more useful but is used only in the "meas freq" mode.

4.5 Program Termination

To terminate the program, return to the "AUTO RUN" menu and press "END PROGRAM". The system will then display the storage positions possible. Select one and wait until the function is complete. When prompted to do so, switch off the 3-STUB CONTROLLER.

5. ERRORS AND SPECIAL PRECAUTIONS

5.1 System Operation Errors

5.1.1 POWER FAILURE

A power failure will result in the controller loosing synchronism with the stub drives. The system must therefore be reindexed before another run.

5.1.2 SPECIFYING FREQUENCY

Even though the current calibrated frequency range displayed is 2,65GHz to 3,05GHz, operation is only from 2,7 to 3,0Hz. Specifying frequencies lower than 2,7GHz can result in a non-converging path calculation - see 5.1.3.

5.1.3 NON CONVERGENCE OF THE PATHFINDER

It is possible that operation beyond the specified frequency

range will result in non-convergence of the "pathfinder" or path optimising routine. To terminate the program, press either "EMERGENCY STOP" while in "AUTO RUN" or "END MANUAL" while in "MANUAL RUN".

5.1.4 ABORTING A RUN

If the system operation is terminated as described in 5.1.3 above, the stubs must be reindexed before restarting. A run should be aborted only in an emergency.

5.1.5 SYSTEM ERRORS (HARDWARE)

Two error messages may de displayed: "SERIAL ERROR" and "NO RESPONSE FROM HPIB". Both will probably be due to a connection problem. However, refer to Section 7 to check on serial card clock frequency.

5.1.6 SYSTEM ERRORS (SOFTWARE)

System errors may occur as a result of incorrect operator responses e.g. an incorrect file name or specifying a frequency beyond that calibrated. In this event, the program will abort. Immediately re-run the program and reindex the motors.

5.2 Special Precautions

5.2.1 PROTECTION OF DRIVE MOTORS AND 3-STUB CONTROLLER

To prevent overheating the drive motors are de-energised when not in use. However, on powerup, the drives are automatically energised. As a result, any system malfunctions could leave the motors energised for long periods. To prevent this, switch off the 3-STUB DRIVE CONTROLLER if not in use or if a system error occurs.

5.2.2 PROTECTION OF MAGNETRON OSCILLATOR

If the drive stubs are in the "transport" position, all stubs are fully inserted into the guide and the reflection coefficient will be of the order of 0,7. Ensure therefore that the mismatch unit stubs are brought to index position or to matched condition before switching on the magnetron modulator. A 'cold' "AUTO RUN" is also recommended initially to reduce the possibility of a mismatch in excess of VSWR = 1,5 occuring.

6. SOFTWARE MODIFICATIONS

6.1 Using Nitrogen instead of SF_6

Since nitrogen needs a higher guide pressure than the SF_6, the stub motor drive speed must be reduced to increase the torque. Line number 150 should be modified as follows:

From: DATA "Y","X","Z",450,250,450,2,4,1,3,5,0,0,0,0

To: DATA "Y","X","Z",250,150,250,2,4,1,3,5,0,0,0,0

This reduces the motor speed for the three axes.

7. ENGINEERING DRAWINGS AND PROGRAM LISTINGS

Drawing No	Title
MS 302/001	WAVEGUIDE MISMATCH UNIT ASSEMBLY
MS 302/002	WAVEGUIDE ASSEMBLY
MS 302/003	WATER LOAD END FLANGE
MS 302/004	WATER LOAD OUTLET NOZZLE
MS 302/005	WATER LOAD OUTLET INSULATING WASHER
MS 302/006	WATER LOAD INLET INSULATOR
MS 302/007	WATER INLET
MS 302/008	MISMATCH STUB ASSEMBLY
MS 302/009	MISMATCH STUB: INNER
MS 302/010	MISMATCH STUB: OUTER
MS 302/011	MISMATCH STUB GUIDE
MS 302/012	MISMATCH STUB PULLER
MS 302/013	WATER LOAD ENVELOPE
MS 302/014	LIMIT SWITCH VALVE
MS 302/015	WASHER
MS 302/016	SERIAL BOARD
MS 302/017	COMPONENT SIDE SERIAL BOARD

7.1 Replacing the Water Load Envelope

To replace a damaged water load envelope, refer to MS302/001. Remove the mismatch stub assembly MS302/008 adjacent to the water inlet by removing the four bolts and withdrawing the unit. Remove the water outlet nozzle MS302/004 and its insulating washer MS302/005. Carefully remove the water load end flange MS302/003 by undoing the eight waveguide bolts. Remove the water load inlet insulator plus water inlet MS302/006 and 007. Withdraw the Pyrex glass envelope MS302/013.

Insert the new glass envelope taking care not to place [illegible]

order, taking note of the positions of the sealing '0' rings. Finally, secure the mismatch stub taking care that the stub moves freely. Test for water and gas leaks.

7.2 Adjusting Serial Card Clock Frequency

Refer to MS302/016 and MS302/017. Connect a frequency counter to TP1 and adjust the variable resistor RV1 to 2400Hz $\pm$ 100Hz. Check the frequency when the unit is cold. Repeat tests at operating temperatures.

7.3 Printed Circuit Masks

Photographic masks for the backplane, serial and power supply boards may be obtained from:

Department of Electronic Engineering
University of Natal
Durban, 4001
South Africa

quoting PHOTOGRAPHIC MASKS FOR UNMS01

8. SAMPLE RUN AND TEST RESULTS

8.1 Match at 3,0GHz
8.2 Match at 2,8GHz
8.3 Match at 2,7GHz
8.4 Reflection coefficient measured for a 2,8GHz "AUTO RUN" sequence
8.5 R.F. pickoff calibration chart
8.6 R.F. pickoff calibration chart (expanded)

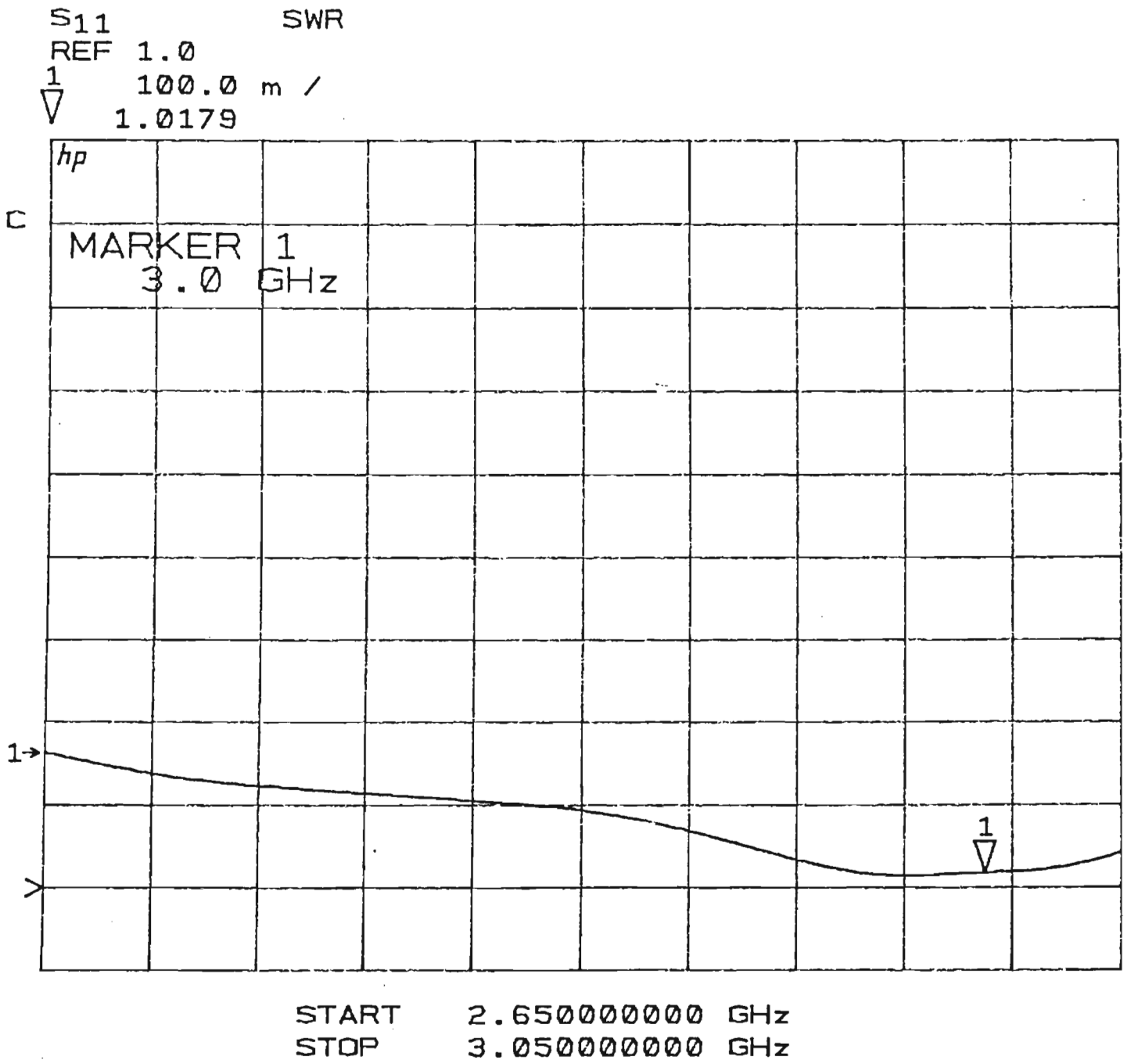
S11
SWR
REF 1.0
1
100.0 m /
1.0179
hp
MARKER 1
3.0 GHz
1
1
START 2.650000000 GHz
STOP 3.050000000 GHz

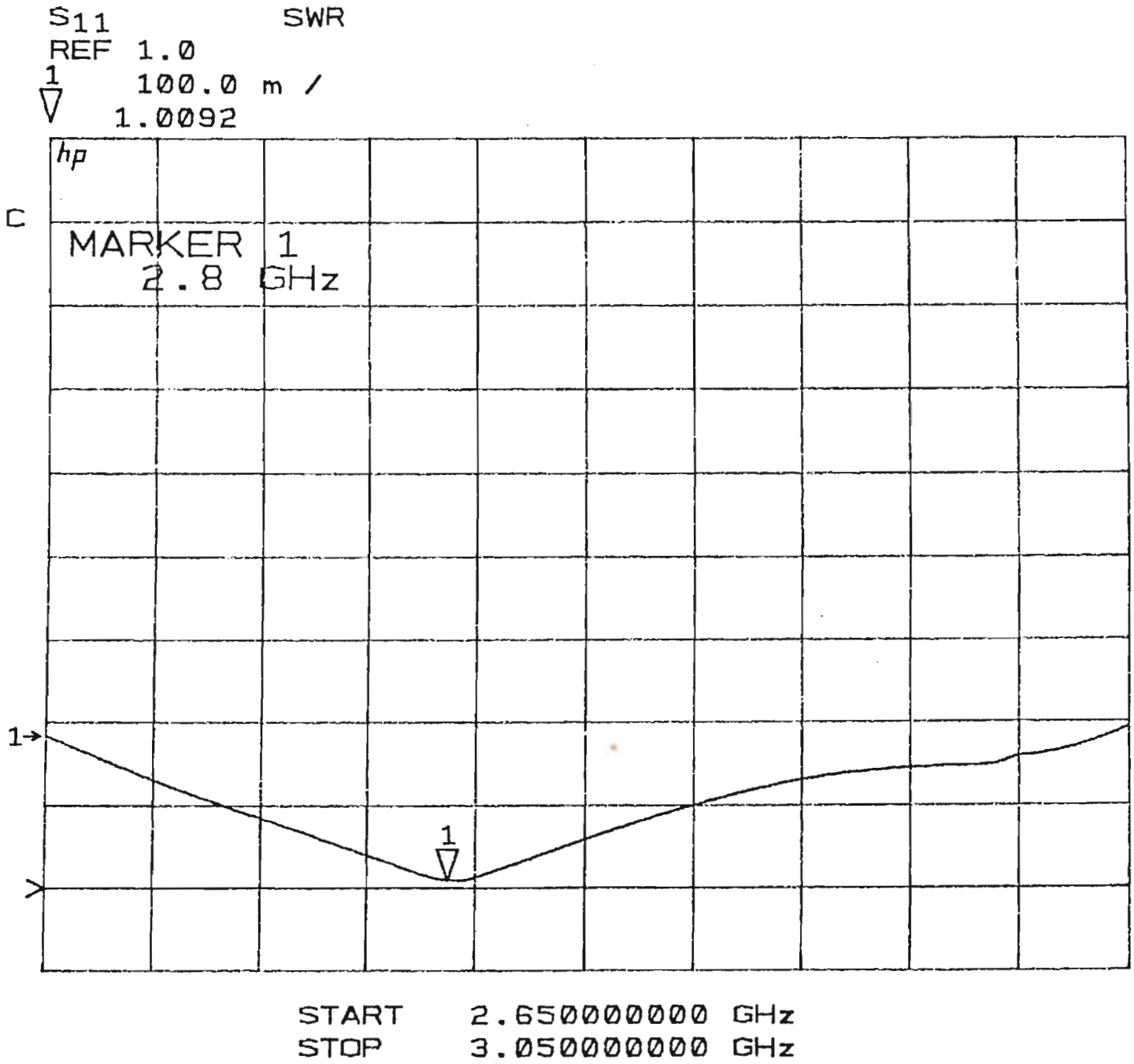
S11
SWR
REF 1.0
1
100.0 m /
1.0092
hp
C
MARKER 1
2.8 GHz
1→
1
START 2.650000000 GHz
STOP 3.050000000 GHz

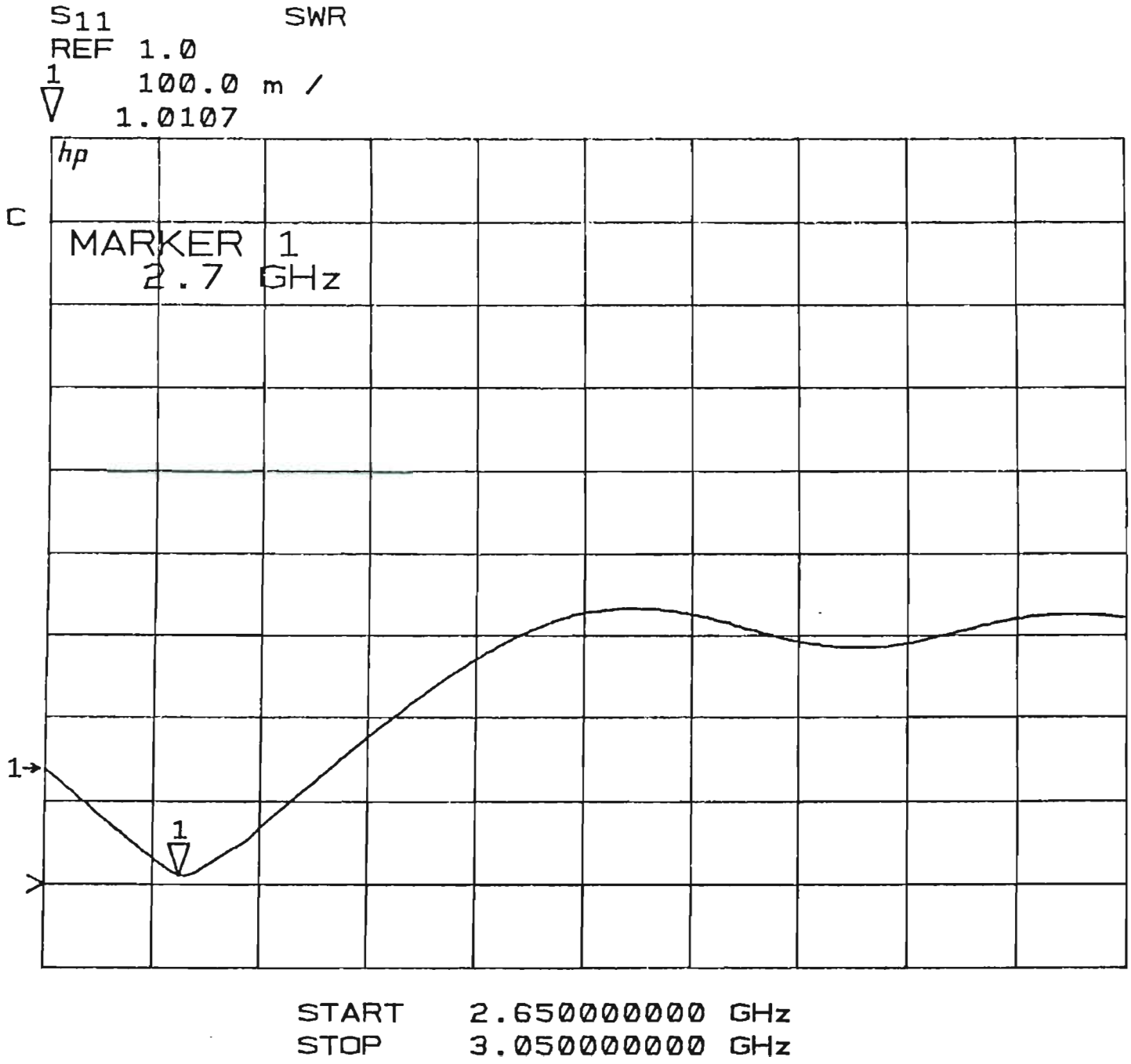
S11
SWR
REF 1.0
1
100.0 m /
1.0107
hp
C
MARKER 1
2.7 GHz
1→
1
START 2.650000000 GHz
STOP 3.050000000 GHz

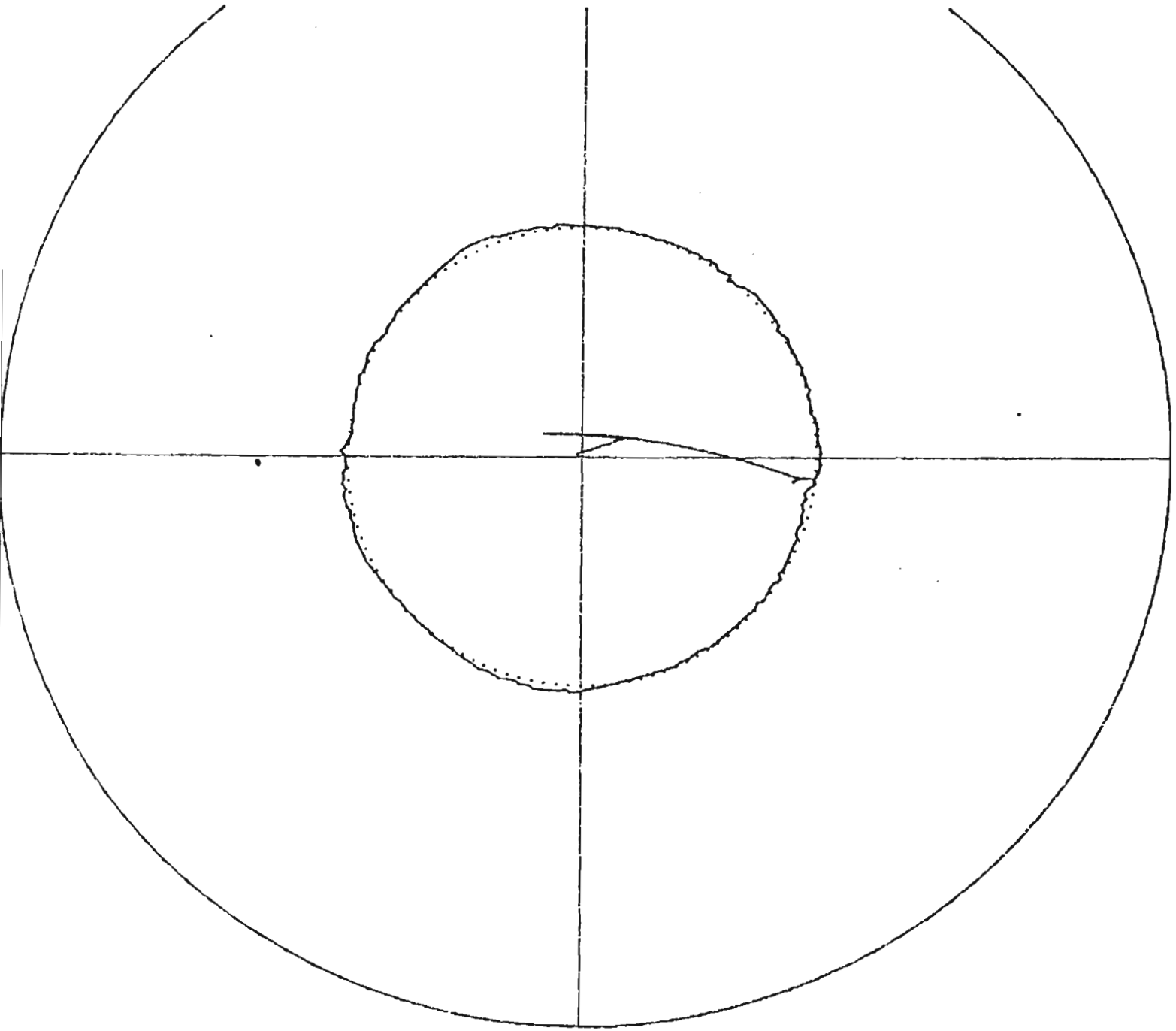

MEASURED REFLECTION COEFFICIENT
FOR AN "AUTORUN" SEQUENCE.

f = 2,8GHz ERROR = 0,005

VSWR = 1,5

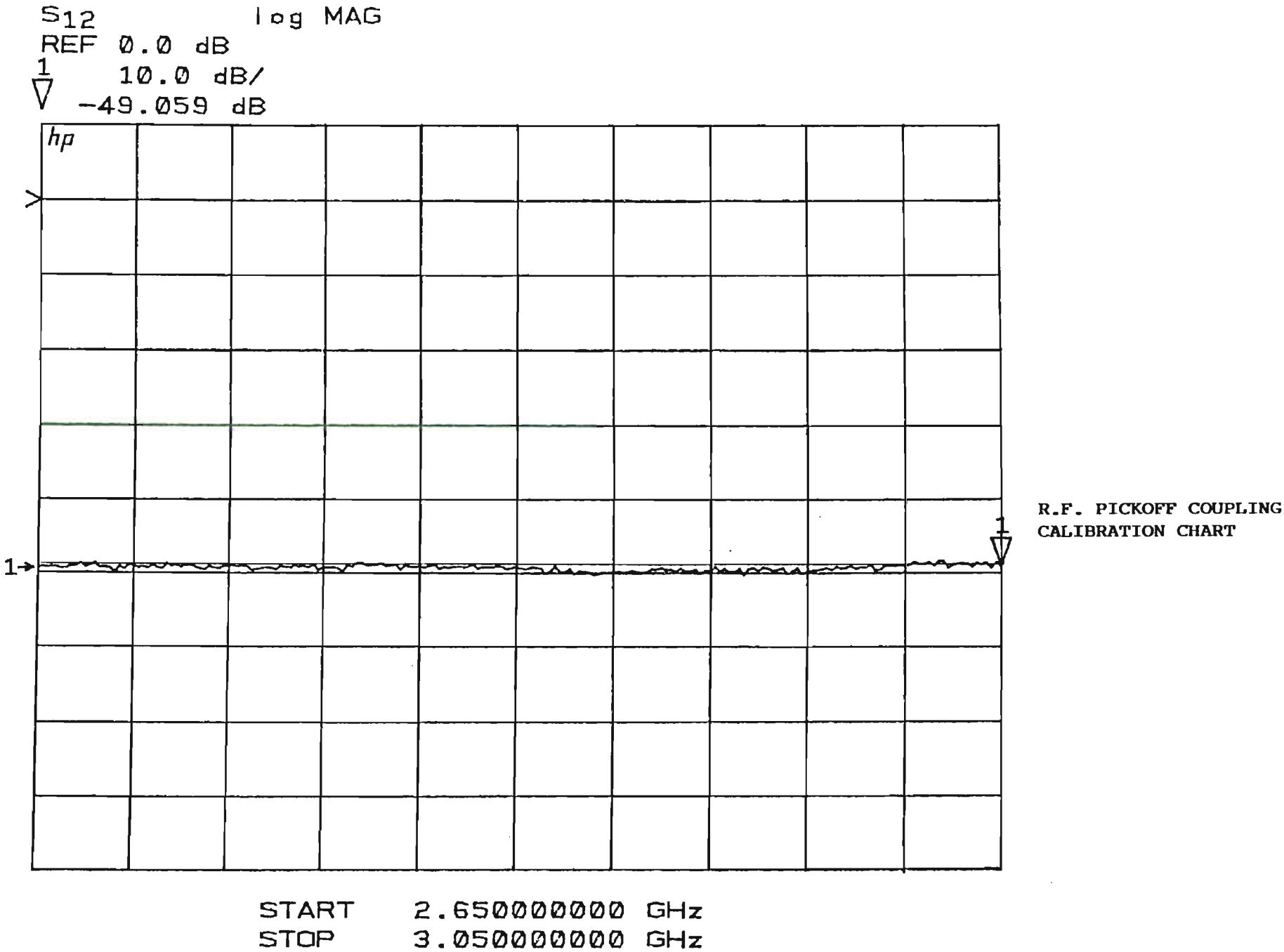

R.F. PICKOFF COUPLING
CALIBRATION CHART

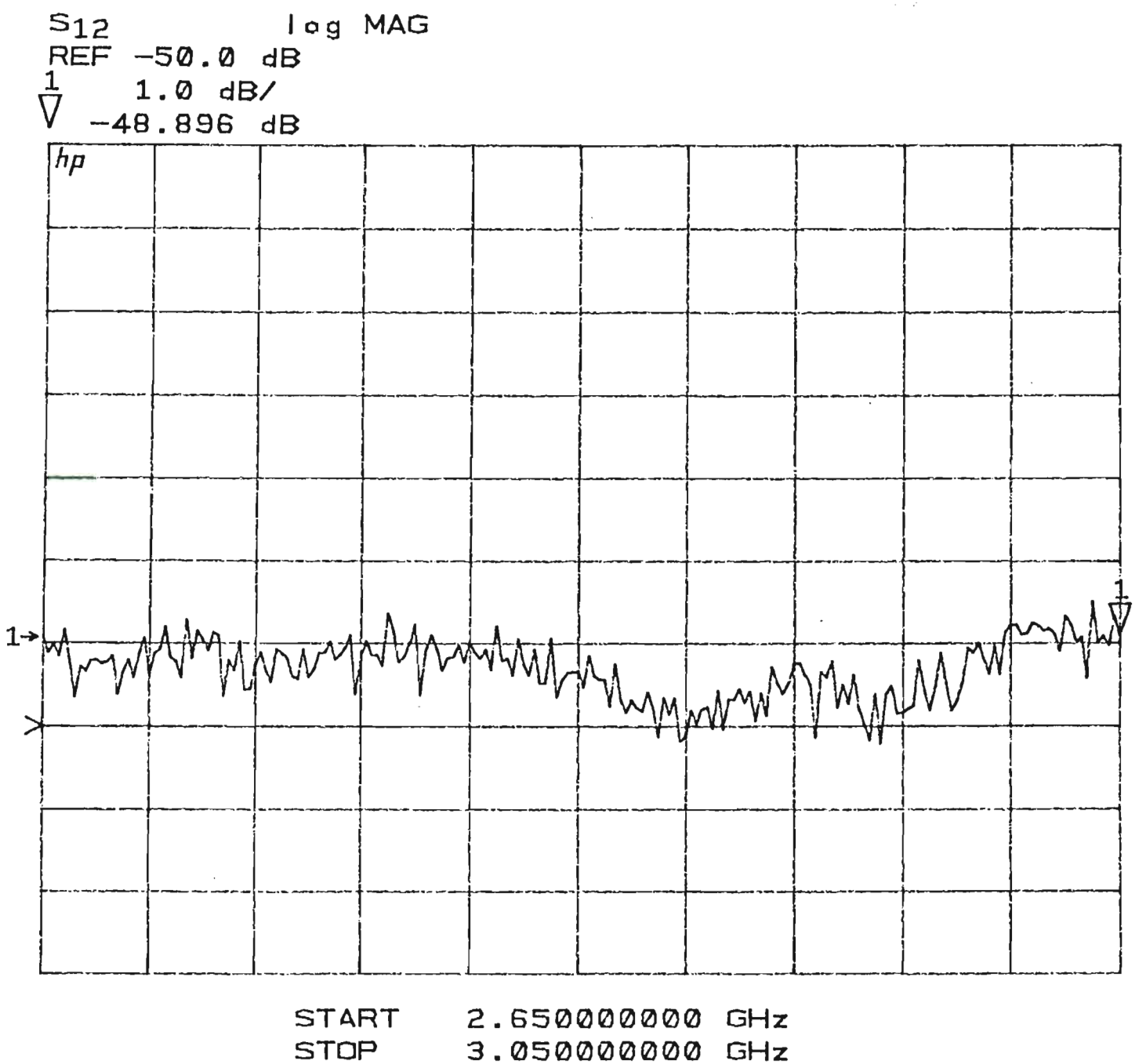

R.F. PICKOFF CALIBRATION CHART (EXPANDED)